Coupled neutronics and computational fluid dynamics for the molten salt fast reactor

PNR-131-2012-005
E. van der Linden
April, 13 2012

Section Physics of Nuclear Reactors
Department Radiation, Radionuclide's and Reactors
Faculty of Applied Physics
Delft University of Technology
Mekelweg 15, 2629 JB Delft
The Netherlands

Coupled neutronics and computational fluid dynamics for the molten salt fast reactor

Featuring a physical description of the precursor transport in liquid turbulent nuclear fuels

Master Thesis

E. van der Linden

April, 14 2012

Supervisors:
Dr. ir. J.L. Kloosterman
Dr. ir. D. Lathouwers

Name:	Erik van der Linden		
Studentnumber:	1539639		
Programme:	Applied Physics specialization: Nuclear Science and Engineering		
Supervising Tutor:	Dr.ir. J.L. Kloosterman	**Research Group:**	Physics of Nuclear Reactors
2nd reviewer:	Dr.ir.D. Lathouwers	**3rd reviewer:**	Prof.dr.ir. C. Kleijn
Start date:	4-4-2011	**End date:**	
Subject to confidentiality agreements?		No	

Acknowledgments

To everyone in the reactor physics group I would like to say: thank you for your patient responses to many of my questions. Thanks goes out to my supervisors Danny Lathouwers and Jan-Leen Kloosterman, without you this project would not have been possible. Special thanks goes out to József Kópházi, for your patience during many of our friendly discussions, which mend a great deal to me, and had a large impact on my thesis project.

Abstract

The foremost fears in society concerning nuclear energy are reactor safety and long lived nuclear waste. A much safer reactor is needed to regain trust, boost the field of nuclear physics and to supply the world's ever increasing demand for clean electric energy. The molten-salt reactor (MSR) has this promise. It is even likely that they can consume more nuclear waste than they produce.

The nuclear fuel of MSRs is dissolved in a liquid salt, which has several advantages. When temperatures exceed predetermined values, a passive safety system allows for the liquid fuel salt to be drained in to several passively cooled sub-critical storage tanks, so that the MSRs can be brought to a passive shutdown during which there is no need for the decay heat to be removed by active means. The molten salt also allows the gaseous neutron absorber xenon to be quickly removed from the reactor core, which makes the breeding of uranium from thorium feasible, so that only thorium, and no uranium, has to be added when refuelling MSRs. The thorium fuel cycle has the advantage that the production of long living transuranic waste is reduced by 5 orders of magnitude as compared to when natural or enriched uranium would have been used.

One promising MSR is the molten salt fast reactor (MSFR). The MSFR does not have a complex graphite core, and only the salt slightly moderates the neutrons, which results in an epithermal neutron spectrum. Due to the absence of any structural material in the core the flow reaches very high Reynolds numbers there.

For a correct physical description of the neutron flux in the MSFR, the transport of the precursors, within the flowing fuel, must be accounted for. Turbulent mixing affects the transport of the precursors, given that the fuel flow through the MSFR's core is turbulent.

In this work a model is presented that physically describes the mutually dependent neutron flux, turbulent flow, and turbulent transport of heat and the precursors. For the flow the Reynolds averaged Navier-Stokes (RANS) equation, with Boussinesq's closure hypothesis and the standard $k - \epsilon$ model are adopted. The multi-group diffusion equation is used for the neutron flux. The convection diffusion equation for scalar transport in turbulent flows has been selected for describing the transport of precursors.

The resulting system of partial differential equations is solved by making use of three different programs. The in-house CFD program HEAT was used to solve the RANS equation and the $k - \epsilon$ model. The in-house program DALTON-MSR solved for the neutron flux and the precursor concentration. A third program was used for generating the temperature-dependent neutron group cross-sections. The three mutually linked programs form the software package named IMP.

Results obtained with IMP show that, when the heat extraction and flow rate remain constant, the MSFR passively reaches a steady state operation. During steady state operation a large recirculation zone is found within the reactor core. As a consequence, unnecessarily high temperatures are reached there, which will corrode the structural material at an unnecessarily high rate. From results obtained with IMP it is concluded that different precursor concentrations would have been found, had turbulent transport of the precursors been unaccounted for. Transient calculations performed with IMP show that there is a strong negative temperature feedback on the reactivity. For a reactivity introduction of $\Delta\rho = 533\,\text{pcm}$, the MSFR becomes super prompt critical. At first, the neutron flux quickly increases by 3 orders of magnitude, but within 50 milliseconds, the flux decreases to levels lower than it was before the transient.

Contents

Nomenclature

A	Atomic weight	[g/mol] or [u]
$C_{\epsilon 1}$	Constant $C_{\epsilon 1}$ = 1.44 for the $k-\epsilon$ model	[-]
$C_{\epsilon 2}$	Constant $C_{\epsilon 2}$ = 1.92 for the $k-\epsilon$ model	[-]
$C_{\epsilon 3}$	Constant $C_{\epsilon 3}$ = 1.0 for the $k-\epsilon$ model	[-]
C_{μ}	Constant C_{μ} = 0.09 for the $k-\epsilon$ model	[-]
C_i	Precursor concentration in precursor group i	[m^{-3}] or [$barn^{-1}cm^{-1}$]
D	Neutronic diffusion constant $D = [3(\Sigma_t - \overline{\mu_0}\Sigma_s)]^{-1}$	[cm^{-2} s^{-1}]
E	Constant for the law of the wall $E = 9.8$ for smooth walls	[-]
K	Number of identical atoms in a molecule	[-]
N_A	Avogadro constant	[6.022 10^{23} mol^{-1}]
N_i	Isotopic or atomic number density	[$barn^{-1}$ cm^{-1}]
N_m	Molecular number density	[$barn^{-1}$ cm^{-1}]
P	Heat source or sink	[W m^{-3}]
P_b	Production of k due to buoyancy effects	[kg m^{-1} s^{-3}]
P_f	Fission power i.e. fission heat	[W cm^{-3}] or [W m^{-3}]
T	Temperature	[K]
β_ρ	Thermal expansion coefficient	[K^{-1}]
$\mathbf{f}_b$	Body force vector	[N m^{-3}]
$\mathbf{u}$	Mean flow velocity vector	[m s^{-1}]
$\mathcal{L}$	Average large eddy length scale	[m]
$\mathcal{V}$	Average large eddy velocity scale	[m s^{-1}]
Pr_t	Turbulent Prandtl number	[-]
c_p	Specific heat capacity	[J kg^{-1} K^{-1}]
g_z	The acceleration of gravity	[m s^{-2}]
k	Turbulent kinetic energy per unit mass	[m^2 s^2] or [J kg^{-1}]
k_{eff}	Neutronic multiplication factor	
p	Pressure	[Pa m^{-3}]
t	Time	
u	Flow velocity vector	[m s^{-1}]
u^+	Dimensionless velocity	[-]
u_τ	Friction velocity	[m s^{-1}]

v_g	Neutron group velocity	[cm s^{-1}]
x_i	Isotope fraction	[-]
x_m	Molecular or atomic fraction	[-]
y^+	Dimensionless distance to the wall	[-]
y_d	Distance to the wall	[m]
Γ	Molecular diffusion constant	[m^2 s^{-1}]
Φ	Neutron flux	[cm^{-2} s^{-1}]
Σ	Group constant macroscopic cross-section	[cm^{-1}]
α	Reactivity coefficient	[pcm]
β	Fraction of the neutrons which is delayed	
χ_g	Fraction of neutrons produced in energy group g	
ϵ	Dissipation of turbulent kinetic energy	[m^2 s^{-3}]
ϵ_f	Energy released per fission	[J]
λ	Decay constant	[s^{-1}]
λ_{T}	Thermal conductivity	[W m^{-1} K^{-1}]
μ	Dynamic viscosity	[Pa s]
μ_t	Eddy viscosity	[Pa s]
ν	Average number of neutrons produced per fission	[-]
ρ	Reactivity	[pcm]
ρ_F	Density of the fuel salt	[kg m^{-3}]
σ_ϵ	Constant σ_ϵ = 1.30 for the $k-\epsilon$ model	[-]
σ_k	Constant σ_k = 1.00 for the $k-\epsilon$ model	[-]
g	Neutron energy group index	

1 Introduction

The foremost fears in society concerning nuclear energy are reactor safety and long lived nuclear waste. A much safer reactor is needed to regain trust, boost the field of nuclear physics and to supply the world's ever increasing demand for clean electric energy. The molten-salt reactor (MSR) has this promise. It is even likely that they can be designed to consume more nuclear waste than they produce.

1.1 The molten-salt reactor and the thorium fuel cycle

Research in Molten-Salt Reactors (MSRs) started in 1947 and was initially financed by the United States military for purposes of making a nuclear fuelled airplane. A *liquid* fuel promised to be the best choice and fluoride salts *"appeared particularly appropriate because they have high solubility for uranium, are among the most stable of chemical compounds, have very low vapour pressure even at red heat, have reasonably good heat transfer properties, are not damaged by radiation and do not react violently with air or water"* [29].

The Oak Ridge National Laboratory (ORNL) did most of the research on the Aircraft Reactor Experiment. They were the first to construct a small (2.5 MW_{th}) molten-salt reactor which reached criticality as early as in 1954. It was fuelled with uranium which was dissolved in a salt. The salt had a chemical composition of NaF, ZrF_4, and UF_4. During its total operation time of 9 days no mechanical nor chemical problems were encountered while the reactor was found to be stable and self-regulating [18].

The purpose of the nuclear fuelled airplane was to make very long flights, enabling the US to drop a nuclear bomb whenever this action of last resort was deemed necessary. But development of the intercontinental ballistic missile made a nuclear fuelled airplane obsolete and consequently halted further research to that end.

(a) Li_2BeF_4 has a melting point of 460 °C and high solubility for uranium and thorium.

(b) The MSRE graphite core.

Figure 1.1 – The fuel salt with U-233 was pumped through the graphite core tubes.

A molten-salt reactor has the attractive option of breeding its own fuel from thorium. Not only is thorium three times more abundant than uranium, it also promises to significantly reduce the amount of nuclear waste produced - the waste reduction is discussed in more detail later on. Natural thorium (100% Th-232) is not fissile, but when it captures a neutron Th-233 is formed. This subsequently undergoes beta decay to protactinium-233 followed by beta decay to U-233. The just described breeding of U-233 from Th-232 is also visualized by Figure 1.2. U-233 thus formed is fissile and can be used as a nuclear fuel.

Producing more U-233 than is consumed is not easy in a neutron economic sense. On average about 2.5 neutrons are produced when U-233 fissions. One neutron needs to be captured by Th-232. More than one is required to induce a new fission: when U-233 absorbs a neutron its chance for fissioning is high, but in about 10% of the cases, a neutron is captured, i.e. not inducing fission [7]. In short: at least 1 neutron needs to be absorbed by Th-232 in order to breed enough U-233, and 1.1 neutron needs to be absorbed by U-233 to induce one fission, which is needed to keep the chain reaction going. This leaves only 0.4 neutrons to be wasted on leakage and parasitic capture by: fission products, protactinium-233, structural materials, molten-salt and moderator if present.

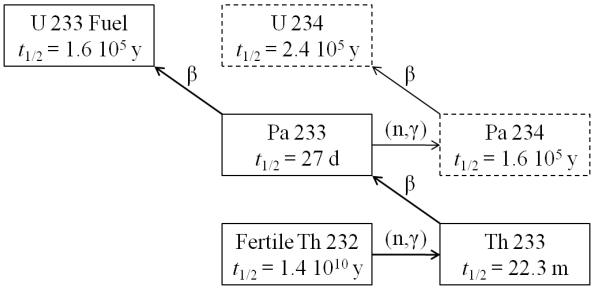

Figure 1.2 – Breeding U-233 fuel from fertile thorium.

There are two reasons that make molten-salt reactors especially attractive for the thorium fuel cycle [29].

- Neutron absorbing gaseous fission products like xenon can be quickly removed from the salt. This saves up neutrons for breeding U-233 from Th-232.
- Removing protactinium-233 ($t_{1/2}$ = 27 d) would prevent it from subsequently capturing a second neutron. This would save neutrons, and would prevent Pa-234 to be formed, which decays to U-234 - a non fissile isotope with a high neutron capture cross-section that only contaminates the reactor fuel.

These advantages are unique for molten-salt reactors - on-line removing xenon or protactinium is harder to realise, if not impossible, for a solid fuelled reactor - making the MSR better suited for breeding in this respect.

Some yet to be discussed safety features and the prospect of less waste production when the more abundant thorium is used, may have been all the motivation that was needed for the experienced scientists associated with the aircraft reactor experiment to start further research of molten-salt reactors. *"That molten-salt reactors might be attractive for civilian power applications was recognized from the beginning ... and in 1956 H.G. MacPherson formed a group to study the technical characteristics, nuclear performance, and economics of molten-salt converters and breeders [29]."*

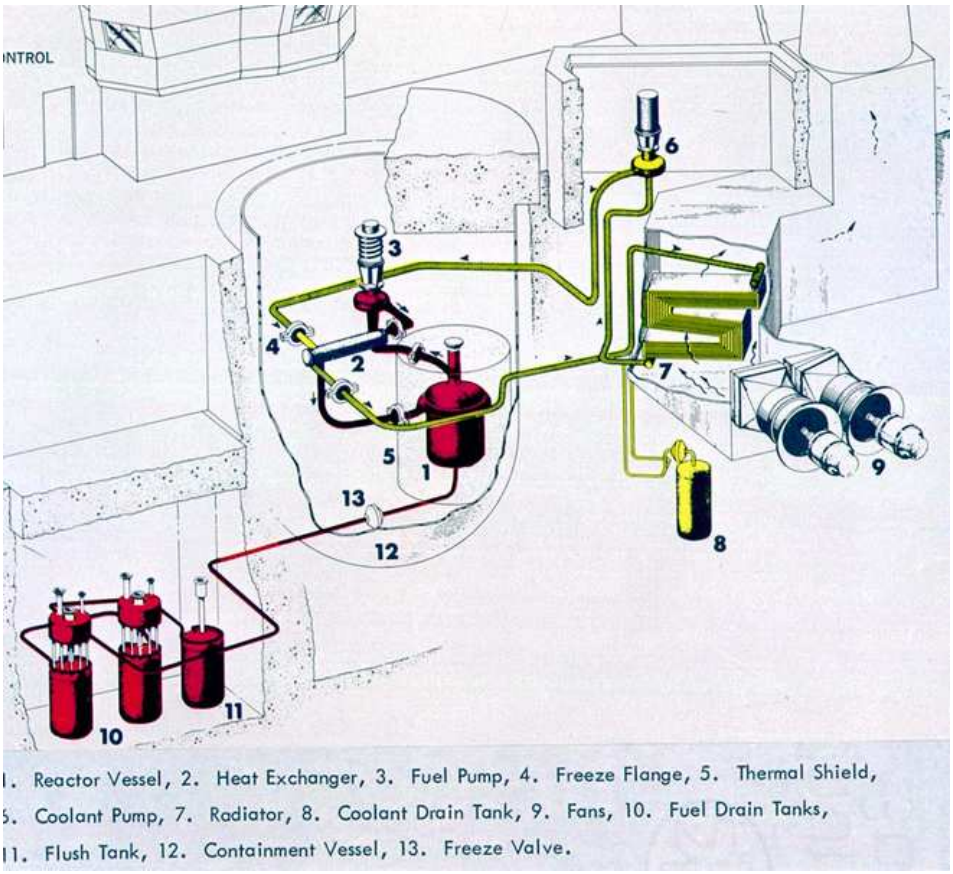

Figure 1.3 – A schematic overview of the MSRE reactor building [16]. The primary circuit is sketched in red, the secondary circuit in yellow. Note that a freeze-plug is depicted near nr 13.

To make optimal use of fuel resources it was decided to build a small graphite moderated MSR appropriately named the Molten-Salt Reactor Experiment (MSRE). Design began in 1960, construction started in 1962 and it first reached criticality in 1965. The fuel salt was composed of uranium, lithium-7, beryllium, and zirconium fluorides which was pumped through the tubes in the graphite reactor core. Both salt and core are shown in Figure 1.1, a diagram of the reactor building is depicted in Figure 1.3 and a top view of reactor inside the building is given in Figure 1.4. After six months of successful operation the (enriched) uranium was removed by treating the fuel with fluorine gas after which it was replaced by U-233. On October 1966 the MSRE was the first reactor that reached criticality on U-233.

In the 1960s, at the time of the MSR-Experiment, uranium reserves were thought to be scarce which promoted interest in breeding reactors. MSRs are however not the only breeding reactors: it had to compete with

liquid metal cooled fast (U-238/Pu-239) breeding reactors (LMFBR). In a fast reactor Plutonium produces more neutrons per fission and suffers from less parasitic neutron capture compared to U-233. This suggested that the LMFBR would be a better breeder. This was part of the reason why the molten-salt reactor lost the competition in an early stage [21]. Funding stopped and the MSRE ended in 1969. Since then no MSR research has been funded at levels comparable to the MSRE.

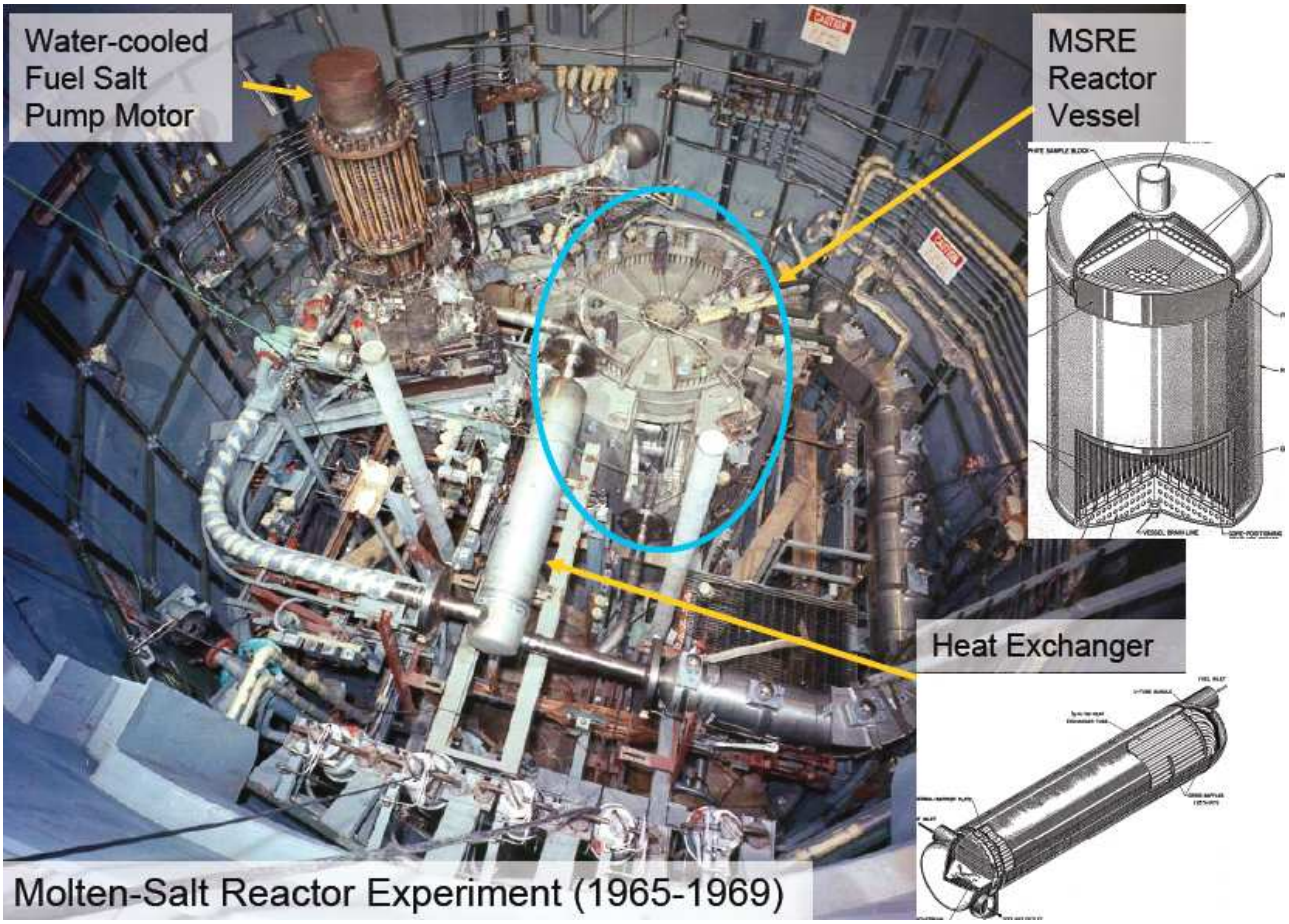

Figure 1.4 – This picture was taken inside the containment of the MSRE building. Here the reactor, heat exchanger, salt pump and many other components can be seen.

Scepticism against thorium breeding has long since been refuted. From 1977 to 1982 a pressurised water reactor fuelled with thorium and uranium-233 proved that thermal breeding is possible. It produced 1.3% more fissile material than it consumed during its 5 years of operation [8]. If a solid fuel boiling water reactor can breed, a MSR certainly can, as the molten-salt allows the xenon and protactinium to be quickly removed from the core.

The MSR's safety aspects, the low waste perspective, and other attractive features give more than enough reason for more (serious) research and development of the MSR. Its potential is starting to get recognised. The European Union is now funding the 1.86 million Euro Evaluation and Viability of Liquid Fuel Fast Reactor Systems (EVOL) project - the research described in this report is part of the EVOL project. This however does not even come close to the level of funding for other nuclear projects.

China appears to have taken the MSR potential more seriously. Under supervision of Ph.D. Jiang Mianheng, son of the former Chinese president Jiang Zemin, China plans to build a molten-salt reactor in 20 years and aims to keep all the intellectual property rights [27].

1.2 MSR safety aspects

Current reactors operating and those under construction need active cooling after shut down in order to extract the decay heat generated by the fission products. Failure of the active cooling system may eventually lead to a scenario where radioactive materials are released to the environment, requiring those who live nearby to be evacuated - as was the case during the recent Fukushima nuclear accident. There are a number of reasons why molten-salt reactors can be made safer than other reactor types, the most relevant of which are listed below.

- The specific heat capacity (1.0 kJ kg^{-1} K^{-1}) and the density ($4.1 \cdot 10^3$ kg m^{-3}) of the salt are high. Combined with a boiling point that is 1000 K higher than the operating temperature, this gives a very high margin to boiling i.e. it takes a long time before the fuel salt reaches dangerous temperatures.

- Reactivity feedback is high: around -6 pcm/K [20]. This makes sure the nuclear reaction rate decreases fast when the fuel temperature increases. As such, abnormal increases in reactor power are quickly suppressed [9].

- The reactor pressure is kept at atmospheric pressure (about 1 bar) reducing risks of leakage. Today's pressurised water reactors operate at 155 bars for comparison.

- Fission products can be removed during operation - and some of the isotopes can be sold [12] such as molybdenum-99 which is of high value to hospitals. By reducing the number of decay products in the fuel salt, the fraction of decay heat generated in the reactor core can be drastically reduced. It means that it will be easier to (passively) cool the fuel after shutdown.

- The neutron absorbing fission product xenon plays an important role in reactor safety - the xenon concentration had a role in initiating the Chernobyl nuclear accident [8]. As a noble gas xenon boils out of the molten-salt almost completely by itself, an effect that can be accelerated by Helium bubbling. During the MSRE it was demonstrated that low xenon concentrations could be realised [29].

- On-line refuelling makes it possible to operate without any excess reactivity. Reaching unintended re-criticality after shutdown is therefore less likely.

- A nuclear reactor needs to be shutdown automatically if something goes wrong. In a Molten-Salt reactor this can be realised by mere passive means, i.e. without the need of moving mechanical parts, input of "intelligence" (instruments) and without an external source of power.
  In a MSR plugs of solidified salt can be installed at the bottom of the reactor. When, for some reason, temperatures become too high these plugs will melt. Gravity then makes sure that the liquid fuel drains into several tanks. The tanks can be designed with physical properties unfavourable for neutron chain reactions thus guaranteeing subcriticality. [17] This freeze-plug drainage-system for molten-salt reactors is significantly more reliable compared to the shutdown system of Pressurised Water Reactors (PWRs) where moving mechanical parts (control rods) as well as instruments and measurements are needed for initiating shutdown.
  Passively cooling the fuel salt storage tanks with natural-convecting air can ensure removal of the decay heat produced by the fission products. This again is very passive, reducing the risk of overheating. It consequently makes scenarios where radioactive materials are released to the environment considerably less likely as compared to PWRs where active pumping of the cooling water is required for removing the decay heat.
  The proof of concept for the freeze-plug has already been delivered during the Molten-Salt Reactor Experiment (MSRE) at Oak Ridge National Laboratory (ORNL) through the 1960s [28]. Although there the plug was molten by active and not by passive means.

These safety gains have to be weighed against some disadvantages unique for molten-salt or thorium fuelled reactors.

- The number of delayed neutrons produced per fission is $\nu_d = 0.0074$ for U-233, which is less than 0.0167 for U-235, but more than 0.0065 for Pu-239. This means that prompt criticality should be prevented by changing reactivity slower as compared to conventional uranium fuelled reactors.

- The effective delayed neutron fraction is (often) further reduced by the salt that moves through and - more importantly - out of the core. The transport of precursors is in fact an important part of this thesis. When more precursors decay outside the core, a higher fraction of prompt neutrons is needed inside the core to keep the chain reaction going i.e. to maintain criticality. This further increases the time needed for changing the reactivity in a controlled fashion thus preventing prompt criticality.
- The potential of leaking chemicals may be of little threat for citizens living nearby since the reactor pressure is low and the fluorides are found to be stable. However, *if* something starts leaking the fuel salt's high specific activity does increase the risk of seriously contaminating the work floor inside the containment where maintenance personnel may have to work.

Some of today's reactors are operating for a significant part on plutonium. This is partly unavoidable since Pu-239 is formed by neutron capture when using uranium fuel which contains more than 95% U-238. More importantly, some reactors are currently fuelled by Mixed Oxide Fuel (MOX) which contains about 7% plutonium and 93% depleted uranium. This means that in MOX fuel elements almost all the precursors originate from plutonium fissions. The point is that current regulatory and safety commissions do accept fuels which produce a relatively small fraction of delayed neutrons and since this fraction is higher for U-233 than for Pu-239 it should not stand in the way of further development of Molten-Salt Reactors.

The potential leakage of nuclear fuel and the consequent risk it brings for maintenance personnel should be taken serious but are not to be overstated. Radiation can not *directly* be seen, heard, smelled or other wise observed. It can however be very accurately measured. Staff of nuclear reactors know this. They are - and should be - well-trained. They know what radiation is and are aware of the potential health risks involved. They closely monitor the dose rates in their working environment: dosimeters carried by each worker will trigger an acoustic alarm when a dose rate approaches a safe limit. If a pipe starts to leak the maintenance personnel will know how to respond accordingly. Weighed against the safer environment for residents living nearby the Molten-Salt Reactor can be a better choice.

1.3 The Low Waste Perspective

Reactors fuelled by (enriched) uranium contain a significant part (96%) of uranium-238. As illustrated by Figure 1.5 most of the long living waste is generated by neutron absorption of U-238 and repeated neutron absorption of newly formed actinides.

Using thorium and U-233 as a fuel ensures that many long living actinides will simply not be created and drastically reduces the long living radio toxic waste. For an equal amount of burnup the production of the actinides americium and curium is 0.3 g with U-233 fuel, contrasted to 25 kg for U-238 fuel - a difference of five orders of magnitude [13].

The few actinides that are produced can be kept in the molten-salt. There they will reach an equilibrium concentration at the point where the actinide's production rate is equal to the destruction rate by fission and decay. Due to the low production rate the equilibrium concentration will also be low, which means that only a tiny fraction of neutrons is needed for burning the actinides. When a molten-salt reactor is started with an actinide concentration above the equilibrium concentration more (actinide) waste will be burned than produced.

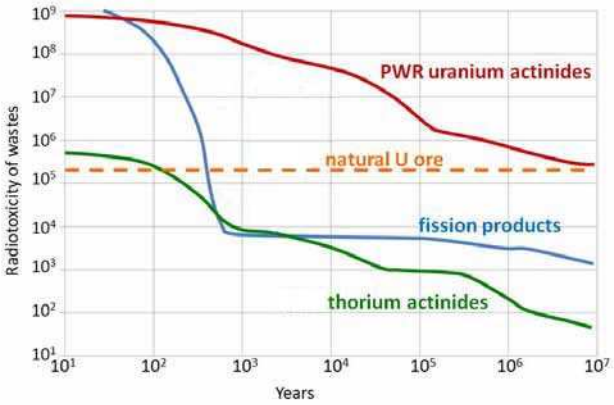

Figure 1.5 – Comparing the radio toxicity [Sv/(GW_{th} year)] of a PWR to a thorium fuelled MSR [6]. Note that similar amounts of fission products are produced while there is a great difference in long living actinides.

It is also optional to leave some of the long living fission products in the molten-salt. Iodine-129 with a half life of (T1/2 = $1.6 \cdot 10^7$ year) is an example of a fission product which can be transmuted by both fast and thermal reactors [5]. Although the fission yield of I-129 is low (0.0076) Iodine is of special interest due to its high volatility. Technetium-99 can also be transmuted, but mainly by fast neutrons only [5]. Produced with a

high yield of 0.063 per fission it reduces the breeding gain by 0.2 which is the price that has to be paid by the neutrons needed for the transmutation.

Whether the transmutation of long living fission products is practical or not remains to be seen. Although the transmutation is worth mentioning, it should actually not be given too high a priority since actinides are much more radio toxic than fission products as was shown by Figure 1.5.

The most important advantage is the prospect of a significant reduction in long living actinide waste. The potential of the thorium fuelled Molten-Salt Reactor, burning more actinides than it produces and its inherently low waste production, cannot be overemphasised.

1.4 The molten-salt fast reactor (MSFR)

The first MSRs, and many other designs that have since been proposed, contain a high volume fraction of graphite [9] which is used for purposes of moderating the neutrons. However, due to the high radiation dose, which is unavoidable inside a nuclear reactor core, the graphite lifetime is limited. Even when the specific power and the neutron flux is kept at relatively low levels, a MSR's core has to be replaced every 20 years or so [22]. Replacing an entire core is not something to think of lightly, and the financial costs may prove to be unacceptably high.

Another disadvantage of graphite moderated MSRs is that the moderator coefficient is occasionally found to be positive - which is a safety concern [9].

Merle-Lucotte et. al. [20] studied many different MSR designs. *"Amongst all TMSR* (Thorium MSR) *configurations, these studies have singled out the configurations with no moderator* (graphite) *in the core as particularly simple and promising. Such a reactor presents indeed many intrinsic advantages, avoiding the deterioration of the moderator while ensuring excellent safety characteristics."*

During this project the relevant physics - the neutronics, liquid fuel and precursor flow - is modelled for the non-moderated Molten-Salt Fast Reactor (MSFR), as defined by Merle-Lucotte in the EVOL project benchmark reference design of May 2011, which is included in the appendix.

For modelling the physics, the computational fluid dynamic program Heat, the neutronic code DALTON-MSR and the group constant generation process has been improved. The new programs were mutually linked. In other words: the MSR-CC originally written by Hoogmoed [11] was improved. The new computational program is named the Improved MSR-CC software Package or IMP in short. The aforementioned benchmark design is used to define the geometry and material properties as assumed by and hard-coded in IMP.

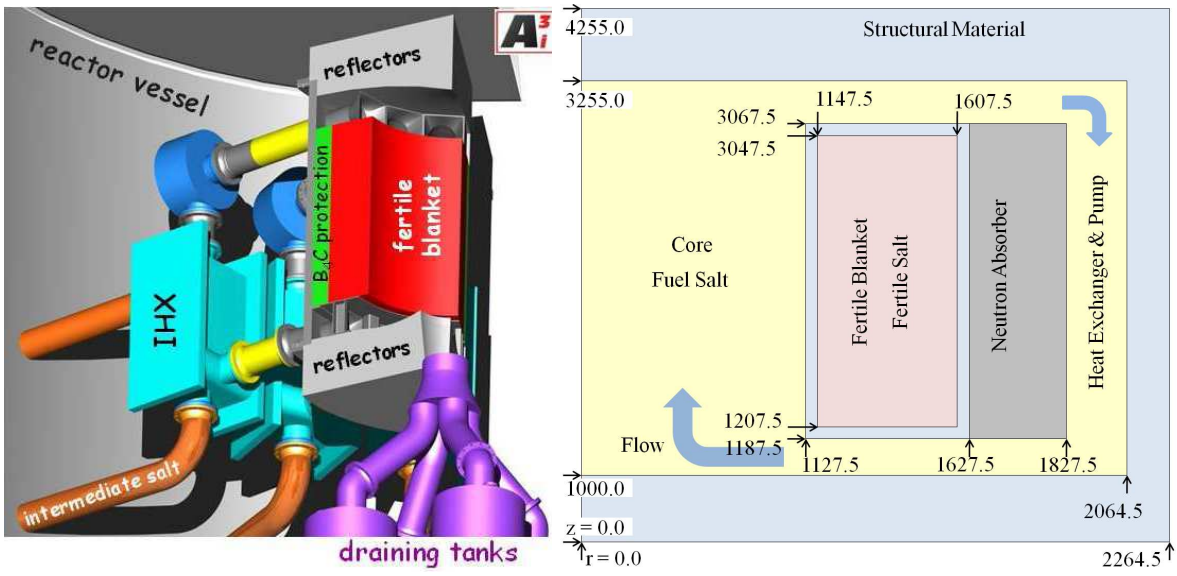

(a) The MSFR's current design. **(b)** Axial symmatric reactor as programed.

Figure 1.6 – The MSFR as defined by the EVOL project reference design. The figures are not scaled. Coordinates of the interfaces are given as implemented in the computational model IMP. Dimensions are given in mm.

Figure 1.6a illustrates the current design of the MSFR. As it is axially symmetric the external circuit is composed of 16 identical components. Each contains a pump as well as a heat exchanger and it is connected to

the reactor core via an inlet and outlet.

Making a computational program for the design as illustrated by Figure 1.6a is challenging and time consuming. Especially when both the neutronics and fluid dynamics are interdependent and have to be correctly linked. For this reason the EVOL project benchmark reference design of 2011 only defines a further simplified MSFR version in great detail. Depicted in Figure 1.6b, it exactly resembles the geometry programmed for the thesis project.

Note that in Figure 1.6b *everything* is cylindrically symmetric, including the part where the salt is pumped - that part is not just a pipe - contrary to what a quick reader may have understood.

1.5 Thesis' focus and layout

This thesis work focuses mainly on the physical modelling of the Molten-Salt Fast Reactor (MSFR) as defined by the EVOL project benchmark reference design of May 2011. The idea behind the EVOL project benchmark is to define a geometry so that different computational programs from different research groups can be compared. This means that each program should accurately describe the physics before similar results can be expected.

To that end this thesis project aims to accurately describe the space and time dependent: neutron flux, group constants, turbulent flow, power production, and temperature. Special emphasis rests on the simultaneous calculation of the mutually dependent heat transport (CFD) and neutron flux - both of which strongly affect each other via multiple feedback mechanisms. The transport of migrating precursors is thoroughly included to an extent that has not yet been published in literature.

In chapter 2 the physical models used are presented. It includes the physical model that describes the precursor concentration for several precursor groups as a function of space and time, which is applicable for liquid (turbulent) nuclear-fuels in general.

Three programs are used for describing the physics for the MSFR: HEAT for the CFD, MIXER for determining the group constant cross-sections and DALTON-MSR for the neutronics and precursors. HEAT and DALTON-MSR have been upgraded for the MSFR. MIXER was completely re-written. As the physics is interrelated, the three programs were mutually linked accordingly. The complete software package thus created will be referred to as the Improved MSFR Package - alias IMP. The programs' details can be found in chapter 3. Results of steady state and transient calculations obtained with IMP are presented in chapter 4. Conclusions and further suggestions are given in chapters 5 and 6.

2 Physics used for modelling the MSFR

2.1 Neutron diffusion equation, transport of precursors and fission heat

2.1.1 Neutron diffusion equation

The MSR version of the neutronics code DALTON-MSR, which is used by IMP, solves for the neutron flux Φ by solving the multi group diffusion equation. Derivation of the diffusion equation is thoroughly discussed in other works such as by Duderstadt & Hamilton [7]. Only the final result will be given here, by equation 2.1.

$$\frac{1}{v_g}\frac{\partial \Phi_g}{\partial t} - \nabla \cdot D_g \nabla \Phi_g + \Sigma_g^r \Phi_g = \sum_{g \neq g'}^{G} \Sigma_{g' \to g}^s \Phi_{g'} + \chi_g \sum_{g'}^{G} (1-\beta)\nu_{g'} \Sigma_{g'}^f \Phi_{g'} + \sum_{i}^{I} \lambda_i \chi_{d,g,i} C_i \tag{2.1}$$

The first term on the left is the rate of change in the neutron group flux $\Phi_g(\mathbf{x}, t)$ - in other words the time dependent rate of change in the neutron density. The second term is the diffusion term which describes the streaming of the neutrons. D_g is the group diffusion constant. The third term accounts for neutrons leaving energy group g either by absorption or out of group scattering, which is represented by the Σ_g^r macroscopic cross-section.

The first term on the right describes the neutrons that scatter from all other energy groups to group g. The second term designates the prompt neutrons produced by fissioning with a kinetic energy that falls in energy group g. It depends on all group fluxes $\Phi_{g'}$, the fraction of prompt neutrons produced $(1-\beta)$, the average number of neutrons produced per fission $\nu_{g'}$, and the group cross-section for fissioning $\Sigma_{g'}^f$. The last term accounts for the delayed neutrons that originate from a precursors decay. Here λ_i is the decay constant and C_i the concentration of precursor group i. In the prompt and delayed neutron production terms χ donates the fraction of neutrons with an energy that fall in energy group g. Note that $\sum \chi_g = 1$. Table 2.1 is provided as a summary for the terms and quantities in the diffusion equation.

Table 2.1 – The Neutronic diffusion equation. An overview of quantities involved and terms in the equation.

D_g	Neutronic Diffusion Constant [cm] $D = [3(\Sigma_t - \overline{\mu_0}\Sigma_s)]^{-1}$.
v_g	Neutron group velocity [cm s^{-1}].
β	Fraction of delayed neutrons.
χ_g	Fraction of prompt neutrons produced in energy group g.
$\chi_{d,g,i}$	Fraction of neutrons produced by radioactive decay of precursor group i, emitted with a kinetic energy falling in energy group g.
λ_i	Decay constant [s^{-1}] of precursor group i.
$\nu_{g'}$	Average neutrons produced per fission induced by a neutron from energy group g'.
Φ_g	Neutron Flux [cm^{-2} s^{-1}] in neutron kinetic energy group g.
Σ	Macroscopic cross-section [cm^{-1}].
$\frac{1}{v_g}\frac{\partial \Phi_g}{\partial t}$	Rate of change of the neutron flux in group g.
$\nabla \cdot D_g \nabla \Phi_g$	Diffusion of the neutrons in neutron flux group g.
$\Sigma_g^r \Phi_g$	Neutrons leaving group g either by absorption or out of group scattering.
$\sum_{g \neq g'}^{G} \Sigma_{g' \to g}^s \Phi_{g'}$	Neutrons scattering in to group g coming from all other groups g'.
$\chi_g \sum_{g'}^{G} (1-\beta)\nu \Sigma_{g'}^f \Phi_{g'}$	Prompt neutrons from fissions appearing in group g.
$\sum_{i}^{I} \lambda_i \chi_{d,g,i} C_i$	Delayed neutrons, with group energy g, that originate from decaying precursors.

One should be aware that several assumptions are made for deriving the diffusion equation. The better the conditions for the assumptions are satisfied, the more accurate and reliable the final solution of the diffusion equation will be. The following is assumed [7].

- The angular flux depends only weakly on angle. More specifically, the angular flux is only linearly anisotropic.
- The neutron source term is isotropic.
- The rate of time variation of the neutron current density is much slower than the collision frequency $v\Sigma_t$.

In practise this means that the diffusion approximation is violated in the following cases [7] p.138.

1) Near boundaries or where material properties change dramatically within distances comparable to a mean free path.
2) Near localized sources.
3) In strongly absorbing media.

The diffusion approximation is usually valid several mean free paths away from sources or boundaries, in weak absorbing media, where the flux only varies slowly in space.

For the MSFR, as defined by the EVOL project Benchmark reference design, there are no localized sources. The only strongly absorbing medium is located behind the fertile blanket, which acts as a neutron reflector for the flux in the reactor core. This ensures that only an insignificant part of the neutrons reach the absorber. As a consequence, the strongly absorbing medium has an insignificant effect on the neutron flux in the reactor core, where fissile uranium is located.

From the points listed above, number 1 was the only one of concern. The neutronic properties of the salt with uranium and the fertile salt without uranium are different. The salt that contains fissile uranium has, due to its high probability of fissioning, a relatively high absorption cross-section - as compared to the uranium free fertile salt, where the absorption cross-section is significantly lower.

Later it will be demonstrated in section 3.2.4.1 that the solution obtained with the diffusion equation is almost identical to the solution obtained with a transport calculation. This demonstrates that the diffusion equation is an accurate description for the MSFR's neutronics.

2.1.2 Convection diffusion equation for precursors in a turbulent nuclear fuel flow

In turbulent flows, transport of scalar quantities (like temperature or chemical concentrations) is generally described by the convection diffusion equation with source and sink terms when appropriate [31]. For the precursor concentration C_i [cm^{-3}] we have

$$\frac{\partial C_i}{\partial t} + \nabla \cdot (C_i \mathbf{u}) = \nabla \cdot \left[\left(\Gamma_i + \frac{\mu_t}{\rho_F \, \mathrm{Pr}_t} \right) \nabla C_i \right] + \beta_i \sum_{g=1}^{G} \nu_g \Sigma_{f,g} \Phi_g - \lambda_i C_i \tag{2.2}$$

The first term on the left is the rate of change in the precursor concentration $C_i(\mathbf{x}, t)$ in precursor group i. The second term designates convection, which depends on the mean flow velocity vector $\mathbf{u}(\mathbf{x}, t)$.

The first term on the right can be divided in two. $\nabla \cdot \Gamma_i \nabla C_i$ describes the molecular diffusion. Turbulent transport is encapsulated by $\nabla \cdot \frac{\mu_t}{\rho_F \, \mathrm{Pr}_t} \nabla C_i$, where ρ_F is the salt's density, and μ_t the turbulent or eddy viscosity, which will be defined later in section 2.2.3.

The second term on the right is a production term which accounts for the precursors produced by fission. Here ν_g is the average number of neutrons produced in energy group g, β_i is the fraction of delayed neutrons that originate from decay by precursor group i. Note that $\sum \beta_i = \beta$ represents the total fraction of neutrons which are delayed.

The last term is a sink term which represents the decay of each precursor group i, each with its typical decay constant λ_i. A description for each term and quantity can also be found in table 2.2.

It is worth mentioning that an almost identical form of equation 2.2 has already been reported in literature, for example by Cammi et. al. [4], except that they (and others) implicitly decided to exclude diffusion and turbulent transport.

Table 2.2 – The Convection Diffusion Equation for Precursors. Each term explained.

$\mathbf{u}$	Mean flow velocity vector as a function of space and time.	[m s^{-1}]
Γ_i	Diffusion constant for precursor group i in the solution.	[m^2 s^{-1}]
μ_t	Dynamic eddy viscosity as a function of space and time.	[Pa s]
ρ_F	Fuel salt density.	[kg m^{-3}]
Pr_t	The turbulent Prandtl number, the default value of Pr_t is 0.85 [30] [3].	
$\frac{\partial C_i}{\partial t}$	Rate of change in the concentration of precursor group i.	.
$\nabla \cdot (C_i \mathbf{u})$	Convection of precursor group i.	
$\nabla \cdot \Gamma_i \nabla C_i$	Diffusion of precursor group i.	
$\nabla \cdot \frac{\mu_t}{\rho_F \sigma_t} \nabla C_i$	Turbulent mixing of precursor group i.	
$\beta_i \sum_{g=1}^{G} \nu_g \Sigma_{f,g} \Phi_g$	Precursors produced by fissions in precursor group i.	
$\lambda_i C_i$	Precursor decay rate, with precursor group decay constant λ_i.	

The convection diffusion equation for precursors can only be solved if the velocity field and eddy viscosity of the fuel flow is known. And its solution - i.e. the precursor concentration as a function of space and time - is needed for solving the neutronics diffusion equation 2.1. In short: the flow most be solved before the neutronic diffusion equation can be solved. This is one of the ways by which neutronics and computation fluid dynamics are linked.

2.1.3 Fission heat

When U-233 fissions some 200 MeV of energy is released. Table 2.3 gives an overview of how the fission energy is distributed.

Table 2.3 – Energy release due to fission [7] p65. The range of the fission product's decay heat deposition is short in a solid fuel. However, the fission products in the molten salt decay wherever the fuel salt is allowed to flow.

Reaction product	Energy [%]	Range	Time Delay
Fission fragment kinetic energy	80	$<$ 0.01 cm	instant
Fast neutrons	3	10-100 cm	instant
Fission gamma energy	4	100 cm	instant
Fission product β^- decay	4	whole primary circuit (MSR)	delayed
Neutrinos	5	irrecoverable	delayed
Non fission reactions due to neutron capture	4	100 cm	delayed

In conventional solid fuelled reactors, the fission products are practically unable to migrate, and they decay at almost exactly the same position as where they were produced, releasing their decay heat there.

In a molten salt reactor the fission products move with the flow. This means that the delayed decay heat will not be released at the location where the uranium fissioned. The convection diffusion equation 2.2 from 2.1.2 can be applied to describe the flow - and the location of decay - of all the fission products (including the precursors). However, during this project, the following equation 2.3 is used for calculating the fission power P_f in [W cm^{-3}]

$$P_f = \sum_{g}^{G} \epsilon_{f_g} \Sigma_{f_g} \Phi_g \tag{2.3}$$

Here, ϵ_{f_g} is the energy released per fission for each energy group g in [J/fission].

It assumes that all of the recoverable fission energy is released, at the exact location of fissioning. In the model the heat will be exactly scaled to the neutron flux. Whereas in reality a small part of the heat production P_f will be distributed over all of the reactor fuel salt, which also flows to locations where the neutron flux is very low.

Equation 2.3 also assumes that all decay heat is produced instantaneously. In reality however, the decay heat is about 6% of nominal power, immediately after a shutdown, after which it gradually decreases as a function of time, as figure 2.1 illustrates.

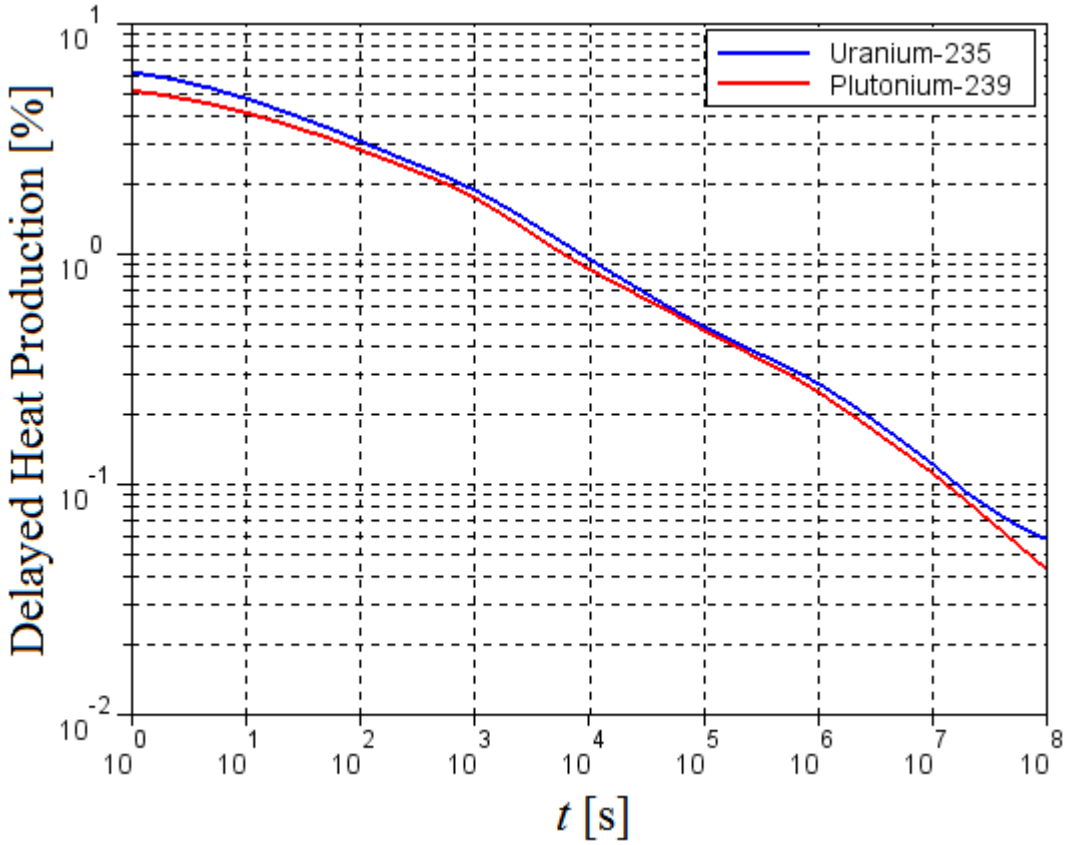

Figure 2.1 – Decay heat as a function of time, as percentage of nominal power, after a reactor shutdown [14]. Immediately after shutdown, the delayed fission heat is about 6% of nominal power. After $t = 10$ s it is about 5% and after $t = 100$ s it is about 3%.

Computation fluid dynamics is needed for calculating the temperature field in which P_f will be treated as a source. The temperature field influences the cross-sections, which affects the flux and thus the power produced. This is another way by which neutronics and CFD are interrelated.

Equation 2.4 expresses what happens to the reactivity ρ due to a change in the temperature of the fuel salt.

$$\frac{\partial \rho(T)}{\partial T} = \alpha \qquad \text{where} \qquad \rho \equiv \frac{k_{\text{eff}} - 1}{k_{\text{eff}}} \tag{2.4}$$

The Doppler effect and thermal expansion of the salt make sure that (with the current salt composition) the reactivity coefficient α remains negative. This means that when the fuel salt's temperature increases, the neutron flux decreases (eq.2.4), which brings down the reaction rate and reduces the power produced (eq.2.3). It is what makes a MSR self regulating. When for example the heat exchangers are malfunctioning, an increase in temperature will decrease the power produced.

2.2 Computational fluid dynamics (CFD) and turbulence modelling

Flows in molten salt reactors are often turbulent. This is especially so for the MSFR where Reynolds numbers may easily reach Re = $\rho_{_F}\, v\, D/\mu \approx 2.5\,10^6$ in the core region and Re $\approx 5.3\,10^5$ in the out-of-core region.

Different models can be used for describing turbulent flows. The most accurate of which is direct numerical simulation (DNS), for which the complete Navier-Stokes equation is solved. For the complex geometry of the MSFR, this method simply needs too much calculation time, even when the best computers available would be used. Large eddy simulation is the next best turbulnce modal that is available. However, the realisation of this model, and the computation time needed to solve the system of equations, were suspected to exceed the 9 months time limit for a master thesis project. Hence, the Reynolds averaged Navier-Stokes (RANS) equations with Boussinesq's closure hypothesis and the standard $k-\epsilon$ model were chosen instead.

At flow velocities lower than the speed of sound for that medium, its density is not affected by pressure, which makes it an incompressible flow [30]. For the MSFR, where $v_{\text{max}} < 10$ m/s, this condition is clearly satisfied. Hence, incompressibility is assumed for modelling the fuel salt flow in the MSFR.

For incompressible flows, the mass conservation equation, also known as the continuity equation reads [30],

$$\nabla \cdot \mathbf{u} = 0 \tag{2.5}$$

2.2.1 Reynolds averaged Navier-Stokes equation

The Navier-Stokes equations are a set of non-linear partial deferential equations that give a complete description of a flow. When DNS is used, every detail of the flow is solved for, from the largest to the smallest eddy. As mentioned above, this is computationally very intensive, to such an extend that it currently can only be used for a limited set of geometries, and certainly not for the MSFR.

The RANS equations give a statistical description of turbulent flows, so that the flow is described in a macroscopic way. By doing this, it is no longer required to resolve the smallest eddies, and it allows for several negligible terms to be dropped from the Navier-Stokes equations, so that its complexity is reduced. Each variable is split in two parts: an average and a fluctuating part. For the flow velocity this means that $\mathbf{U} = \mathbf{u} + \mathbf{u}'$, where $\mathbf{U}$ is the actual velocity, $\mathbf{u}$ the mean velocity and $\mathbf{u}'$ the fluctuating velocity. For incompressible flows the Reynolds averaged Navier-Stokes equation reads

$$\rho_{_F} \frac{\partial \overline{\mathbf{u}}}{\partial t} + \rho_{_F} \left(\overline{\mathbf{u}} \cdot \nabla\right) \overline{\mathbf{u}} = -\nabla \overline{p} + \nabla \cdot \left[\mu \left(\nabla \overline{\mathbf{u}} + (\nabla \overline{\mathbf{u}})^{\mathrm{T}}\right) - \rho_{_F} \overline{u_i' u_j'}\right] + \mathbf{f_b} \tag{2.6}$$

wherein the time averaged quantities are indicated by an overline. From left to right the first term describes the rate of change in the mean flow velocity $\overline{\mathbf{u}}$. The second term denotes convection.

The first term to the right is a pressure term. Flow generally accelerates in the direction anti parallel to a pressure gradient, hence the "$-$" sign. The second term is a diffusion term. The third term on the right denotes the turbulent Reynolds stress tensor τ, which is a 3×3 matrix, wherein $\tau_{ij} = -\rho \overline{u_i' u_j'}$. The last term is a body-force, such as gravity. Note that $\nabla \mathbf{u}$ is a matrix, and that $^{\mathrm{T}}$ denotes its transposed. For Cartesian coordinates we have

$$\nabla \mathbf{u} = \begin{bmatrix} \dfrac{\partial u_x}{\partial x} & \dfrac{\partial u_x}{\partial y} & \dfrac{\partial u_x}{\partial z} \\ \dfrac{\partial u_y}{\partial x} & \dfrac{\partial u_y}{\partial y} & \dfrac{\partial u_y}{\partial z} \\ \dfrac{\partial u_z}{\partial x} & \dfrac{\partial u_z}{\partial y} & \dfrac{\partial u_z}{\partial z} \end{bmatrix} \tag{2.7}$$

The RANS equation needs a closure hypothesis, i.e. an expression for the Reynolds stresses. The Boussinesq's closure hypothesis is assumed, which reads that Raynolds stresses are assumed to be proportional to mean rates of deformation [30] p67. For the Reynolds stresses we have, assuming incompressibility,

$$\tau_{ij} = \mu_t \left(\frac{\partial \overline{u_i}}{\partial x_j} + \frac{\partial \overline{u_j}}{\partial x_i}\right) + \frac{2}{3} \rho_{_F} k \delta_{ij} \tag{2.8}$$

using a different notation

$$\tau = \mu_t \left(\nabla \overline{\mathbf{u}} + (\nabla \overline{\mathbf{u}})^{\mathrm{T}}\right) + \frac{2}{3} \rho_{_F} k \mathrm{I} \tag{2.9}$$

here, k is the turbulent kinetic energy per unit mass, μ_t the turbulent or eddy viscosity, I the identity matrix, and δ_{ij} the chronicle delta which is 1 for $i = j$ and 0 otherwise.

Boussinesq's closure hypothesis is generally valid as long as $Re^{1/4} \gg \frac{u}{a}$, where u is the velocity and a the speed of sound in the fluid. [23] p61. For the MSFR $a_{\text{LiF}} > 1500\,\text{m s}^{-1}$, as the speed in LiF is faster than the speed of sound in water, which is $a_{\text{H}_2\text{O}} \approx 1500\,\text{m s}^{-1}$. The maximum fuel salt velocity in the MSFR is $u < 10\,\text{m s}^{-1}$. So, for the MSFR, the condition is clearly satisfied.

According to Versteeg and Malalasekera, all models that are based on the Boussinesq's closure hypothesis will have problems in swirling flows and flows with large rapid extra strains (e.g. highly curved boundary layers and diverging passages) that effect the structure of the turbulence in a subtle manner [30]. For the MSFR the outflow of the fuel salt is diverging. This can be expected to have little effect on the fuel flowing in to the reactor core, and may therefore be of little consequence for the parameters of interest, such as the time average temperature.

With Boussinesq's closure hypothesis the Reynolds averaged Navier-Stokes (RANS) equation for incompressible flow becomes [4].

$$\rho_{_F} \frac{\partial \overline{\mathbf{u}}}{\partial t} + \rho_{_F} \left(\overline{\mathbf{u}} \cdot \nabla\right) \overline{\mathbf{u}} = -\nabla \cdot \left(\overline{p}\mathrm{I} + \frac{2}{3}\rho_{_F} k\mathrm{I}\right) + \nabla \cdot \left[\left(\mu + \mu_{_t}\right)\left(\nabla \overline{\mathbf{u}} + \left(\nabla \overline{\mathbf{u}}\right)^{\mathrm{T}}\right)\right] + \mathbf{f}_b \tag{2.10}$$

The third term on the right can be divided in two. A term that contains the viscosity μ, and a term that contains eddy viscosity $\mu_{_t}$. The first term accounts for molecular diffusion, the second for transport by turbulence, i.e. turbulent diffusion. For equation 2.10 a summary for each term is given in table 2.5.

Table 2.4 – The Reynolds averaged Navier-Stokes equation. Each term explained.

$\overline{\mathbf{u}}(\mathbf{x}, t)$	The mean velocity vector.	[m s^{-1}]
$\overline{p}(\mathbf{x}, t)$	The Reynolds averaged pressure.	[Pa m^{-3}]
$k(\mathbf{x}, t)$	Turbulent kinetic energy per unit mass.	[J kg^{-1}] = [m^2 s^{-2}]
μ	Dynamic viscosity of the fluid.	[Pa s]
$\mu_{_t}(\mathbf{x}, t)$	Turbulent viscosity, also known as eddy viscosity.	[Pa s]
$\mathbf{f_b}(\mathbf{x}, t)$	Body force vector e.g. gravity.	[N m^{-3}]
$\rho_{_F} \frac{\partial \overline{\mathbf{u}}}{\partial t}$	Time dependent rate of change.	
$\rho_{_F} \left(\overline{\mathbf{u}} \cdot \nabla\right) \overline{\mathbf{u}}$	Convection of the mean flow.	
$-\nabla \overline{p} - \nabla \cdot \left(\frac{2}{3}\rho_{_F} k\mathrm{I}\right)$	Pressure term.	
$\nabla \cdot \left[\left(\mu + \mu_{_t}\right)\left(\nabla \mathbf{u} + \left(\nabla \mathbf{u}\right)^{\mathrm{T}}\right)\right]$	Diffusion and turbulent mixing.	

2.2.2 Buoyancy in an incompressible flow

The gravity force on the fluid f_z in [N m^{-3}] depends on the density, and as the density is a function of temperature the same holds for f_z. The first order Taylor expansion for f_z is given by equation 2.11. It remains valid as long as $|\beta_\rho(T_t)(T - T_t)| \ll 1$.

$$f_z = \rho_{_F}(T)\, g_z \approx \rho_{_F}(T_t)\, g_z \left[1 - \beta_\rho(T_t)\left(T - T_t\right)\right] \tag{2.11}$$

Here, $\beta_\rho(T_t)$ is the thermal expansion coefficient in [K^{-1}] at a given reference temperature T_t in [K] and $g_z = -9.81$ m s^{-2}. The thermal expansion coefficient β_ρ is defined by equation 2.12. Note that $\beta_\rho > 0$ for almost all fluids.

$$\beta_\rho \equiv -\frac{1}{\rho_{_F}} \left.\frac{\partial \rho_{_F}}{\partial T}\right|_{T=T_t} \tag{2.12}$$

From equation 2.11 a first order approximation for the buoyancy force can be derived. The result of which is

$$f_{b_z} \approx -\rho_{_F}(T_t)\, g_z\, \beta_\rho(T_t)\, (T - T_t) \tag{2.13}$$

f_{b_z} is the upward buoyancy force in [N m^{-3}]. The density $\rho_{_F}(T_t)$ is assigned a constant value for a given reference temperature T_t (even though the actual temperature T varies in space and time). The thermal expansion coefficient $\beta_\rho(T_t)$ has to be evaluated at the same temperature T_t. The buoyancy f_{b_z} can be substituted in equation 2.6 as a body force.

2.2.3 Standard $k - \epsilon$ model

Boussinesq's closure hypothesis introduces new quantities, i.e. turbulent kinetic energy and eddy viscosity, for which an additional model is needed. For this, different models are available. According to Versteeg and Malalasekera, the $k - \epsilon$ model is most widely used and validated [30].

The large-scale turbulence can be represented by the large-eddy velocity scale $\mathcal{V}$ and the large-eddy length scale $\mathcal{L}$. They can be defined by the turbulent kinetic energy per unit mass k in [J kg^{-1}] or [m^{2}s^{-2}] and ϵ, which is the dissipation of the turbulent kinetic energy in [m^2 s^{-3}].

$$\mathcal{V} \equiv k^{1/2} \qquad \mathcal{L} \equiv \frac{k^{3/2}}{\epsilon} \tag{2.14}$$

The eddy viscosity $\mu_{_t}$ is the product of the large-eddy scales and is defined by

$$\mu_{_t} = C_\mu \rho_{_F} \mathcal{V}\mathcal{L} = C_\mu \rho_{_F} \frac{k^2}{\epsilon} \tag{2.15}$$

C_μ is a dimensionless constant. Equations 2.16 and 2.17 are used to describe the transport of k and ϵ [4] [19].

$$\rho_{_F} \frac{\partial k}{\partial t} + \rho_{_F} \nabla \cdot (k\, \mathbf{u}) = \nabla \cdot \left[\left(\mu + \frac{\mu_{_t}}{\sigma_k} \right) \nabla k \right] + P_k + P_b - \rho_{_F} \epsilon \tag{2.16}$$

$$\rho_{_F} \frac{\partial \epsilon}{\partial t} + \rho_{_F} \nabla \cdot (\epsilon\, \mathbf{u}) = \nabla \cdot \left[\left(\mu + \frac{\mu_{_t}}{\sigma_\epsilon} \right) \nabla \epsilon \right] + C_{\epsilon 1} \frac{\epsilon}{k} \left[P_k + C_{\epsilon 3} \max(P_b, 0) \right] - C_{\epsilon 2} \rho_{_F} \frac{\epsilon^2}{k} \tag{2.17}$$

In words:

Rate of change of ϵ or k	+	Transport by convection	=	Transport by diffusion	+	Rate of production	−	Rate of destruction

Regarding the transport equations 2.16 and 2.17 for k and ϵ, we are already familiar with the first three terms that, from left to right, denote the rate of change, convection, and (turbulent) diffusion. The other terms are production terms for k or ϵ. The last term of each equation is the destruction of k or ϵ.

P_k is the production of turbulent kinetic energy

$$P_k = \mu_{_t} \mathbb{T}^2 \tag{2.18}$$

where $\mathbb{T}$ is the tensor

$$\mathbb{T} = \left(\nabla \mathbf{u} + (\nabla \mathbf{u})^{\mathrm{T}} \right) \tag{2.19}$$

The scalar product of $\mathbb{T}$ with itself is

$$\mathbb{T}^2 = \mathrm{t}_{11}^2 + \mathrm{t}_{12}^2 + \mathrm{t}_{13}^2 + \mathrm{t}_{21}^2 + \mathrm{t}_{22}^2 + \mathrm{t}_{23}^2 + \mathrm{t}_{31}^2 + \mathrm{t}_{32}^2 + \mathrm{t}_{33}^2 \tag{2.20}$$

The constants are experimentally determined [30].

$$C_\mu = 0.09 \quad \sigma_k = 1.00 \quad \sigma_\epsilon = 1.30 \quad C_{\epsilon 1} = 1.44 \quad C_{\epsilon 2} = 1.92 \quad C_{\epsilon 3} = 1.0 \text{ [19]}$$

In the equations above, P_b is the production of k or ϵ by buoyancy effects [10]

$$P_b = -\beta_\rho g_z \frac{\mu_t}{\mathrm{Pr}_t} \frac{\partial T}{\partial z} \tag{2.21}$$

Here, $g_z = -9.81$ [m s^{-2}], and Pr_t is the dimensionless turbulent Prandtl number which is taken to be $\mathrm{Pr}_t = 0.85$ during this project. The coefficient of thermal expansion β_ρ in [K^{-1}] was earlier defined by equation 2.12. Van Maele and Merci [19] noted that with this approach, the magnitude of the buoyancy production term is known to be underestimated, and they reposed alternative, more complex, estimates of P_b [19].

For deriving the $k - \epsilon$ model several approximations are made, due to which it may perform poorly in the following cases [30].

1 For some unconfined flows. *"The model is reported not to perform well in weak shear layers (far wakes and mixing layers), and the spreading rate of axially symmetric jets in stagnant surroundings is severely over predicted. In large parts of these flows the rate of production of turbulent kinetic energy is much less than the rate of dissipation, and the difficulties can only be overcome by making ad hoc adjustment to model constants C."*

2 In flows with large extra strains (e.g. strongly curved boundary layers or swirling flows).

3 Flows driven by anisotropy of normal Reynolds stresses (e.g. fully developed flows in non-circular ducts).

4 The model is oblivious to body forces due to rotation of the frame of reference.

For the MSFR, point 2 and 3 may be of concern. A large recirculation zone is found in the reactor core, and there are sharp corners near the inlet and outlet, where large strains and anisotropy of the Reynolds stresses can be expected. It should be emphasised that using the Reynolds averaged Navier-Stokes equation, with Boussinesq's closure hypothesis, and the $k - \epsilon$ model only describes a turbulent flow by approximation. The extent of its validity has to be experimentally verified for the MSFR's geometry.

2.2.4 Near wall flow behaviour and the law of the wall

Near a wall boundary the behaviour of turbulent flow is considerably different as compared to free turbulent flow. Close to the wall the flow is influenced by viscous effects and does not depend on free stream parameters. Here the law of the wall can be used as given by equation 2.22 [30].

$$u^+ \equiv \frac{u}{u_\tau} = \begin{cases} y^+ & y^+ \leq 11.3 \\ \frac{1}{\kappa} \ln(E\, y^+) & 11.3 < \; y^+ < 500 \end{cases} \tag{2.22}$$

Here, $\kappa = 0.41$ is the Von Karman's constant and E the dimensionless wall roughness parameter. For smooth walls $E = 9.8$ while for rougher walls it is lower. In equation 2.22 above u^+ is the dimensionless velocity and u_τ the so called friction velocity in [m s^{-1}]. The dimensionless distance to the wall y^+ is defined by equation 2.23 below. In which y_d is the distance to the wall and μ the dynamic viscosity.

$$y^+ \equiv \frac{\rho_F u_\tau y_d}{\mu} \tag{2.23}$$

Near the wall the Reynolds averaged Navier-Stokes equation and the standard $k - \epsilon$ model can be related - through u_τ - by equation 2.22 and 2.24 [30].

$$k = \frac{u_\tau^2}{\sqrt{C_\mu}} \qquad \epsilon = \frac{u_\tau^3}{\kappa\, y_d} \tag{2.24}$$

Near the wall the mean velocity gradient is large, which ensures a high production of turbulent kinetic energy k. This means that the wall effects are important for the accuracy of the final result. During this work it was aimed to keep $y^+ < 30$ for each volume element adjacent to a wall.

2.2.5 Temperature transport in a turbulent flow

Transport of scalar quantities in a turbulent flow can be described by the convection diffusion equation as was earlier discussed in section 2.1.2. For the Reynolds averaged temperature T in a molten salt reactor we have equation 2.25 [4].

$$\rho_{_F} c_p \frac{\partial T}{\partial t} + \rho_{_F} c_p \nabla \cdot (T\overline{\mathbf{u}}) = \nabla \cdot \left[\left(\lambda_{\mathrm{T}} + c_p \frac{\mu_{_t}}{\mathrm{Pr}_t} \right) \nabla T \right] + P \tag{2.25}$$

Again from left to right the rate of change, convection and (turbulent) diffusion terms can be recognised. The specific heat capacity is denoted by c_p and the heat conduction by λ_{T}. Table 2.5 gives a description for each quantity and term involved.

Table 2.5 – The Convection Diffusion Equation for the temperature. Each term explained.

$\overline{\mathbf{u}}(\mathbf{x}, t)$	Mean flow velocity vector.	[m s^{-1}]
λ_{T}	Thermal conductivity.	[J K^{-1} m^{-1} s^{-1}]
$\mu_{_t}(\mathbf{x}, t)$	Dynamic eddy viscosity as a function of space and time.	[Pa s] or [kg m^{-1} s^{-1}]
$P(\mathbf{x}, t)$	Heat-source or sink.	[J m^{-3} s^{-1}]
$\rho_{_F}$	Fuel salt density.	[kg m^{-3}]
Pr_t	The turbulent Prandtl number. Pr_t = 0.85 by default [30] [3].	[-]
c_p	Specific heat capacity.	[J Kg^{-1} K^{-1}]
$\rho_{_F} c_p \frac{\partial T}{\partial t}$	Rate of change.	.
$\rho_{_F} c_p \nabla \cdot (T\mathbf{u})$	Temperature transport by convection.	
$\nabla \cdot \left[\left(\lambda_{\mathrm{T}} + c_p \frac{\mu_{_t}}{\mathrm{Pr}_t} \right) \nabla T \right]$	Temperature transport by diffusion and turbulent transport.	

Assuming that all fission heat is created instantaneously at the moment and location of fissioning we set $P = P_f$. As was earlier defined by equation 2.3.

3 The computation programs that model the MSFR

During this thesis project a computational software package, named IMP, was created for calculating the physical behaviour of the MSFR in particular. IMP uses DALTON-MSR, MIXER and HEAT. DALTON-MSR is a multi group diffusion code which solves equation 2.1 and the precursor transport equation 2.2. DALTON-MSR needs group constants i.e. cross sections. They are provided by MIXER. HEAT is a CFD code that solves the RANS and $k-\epsilon$ equations 2.10 - 2.25. In other words, HEAT solves for the turbulent flow and temperature profile. Both HEAT and DALTON-MSR use the finite volume method to numerically solve the partial differential equations.

3.1 Detailed description of the MSFR benchmark reference design

As discussed earlier in the introduction, IMP models a simplified geometry of the MSFR. Its design, material composition and the physiochemical properties are defined by the EVOL project benchmark reference design of May 2011 which is included in the Appendix.

3.1.1 Reactor design

Figure 3.1 below depicts the reactor as modelled. This simplified design of the reactor is axially symmetric. The vast majority of the fissions will be located in the reactor core. The structural material and the fertile blanket act as a neutron reflector. The pipes, fuel pumps and heat exchangers, i.e. the system outside the core, is axially symmetrically modelled by IMP. The neutron absorber shields the heat exchanger and fuel salt pump from unnecessary high neutron radiation.

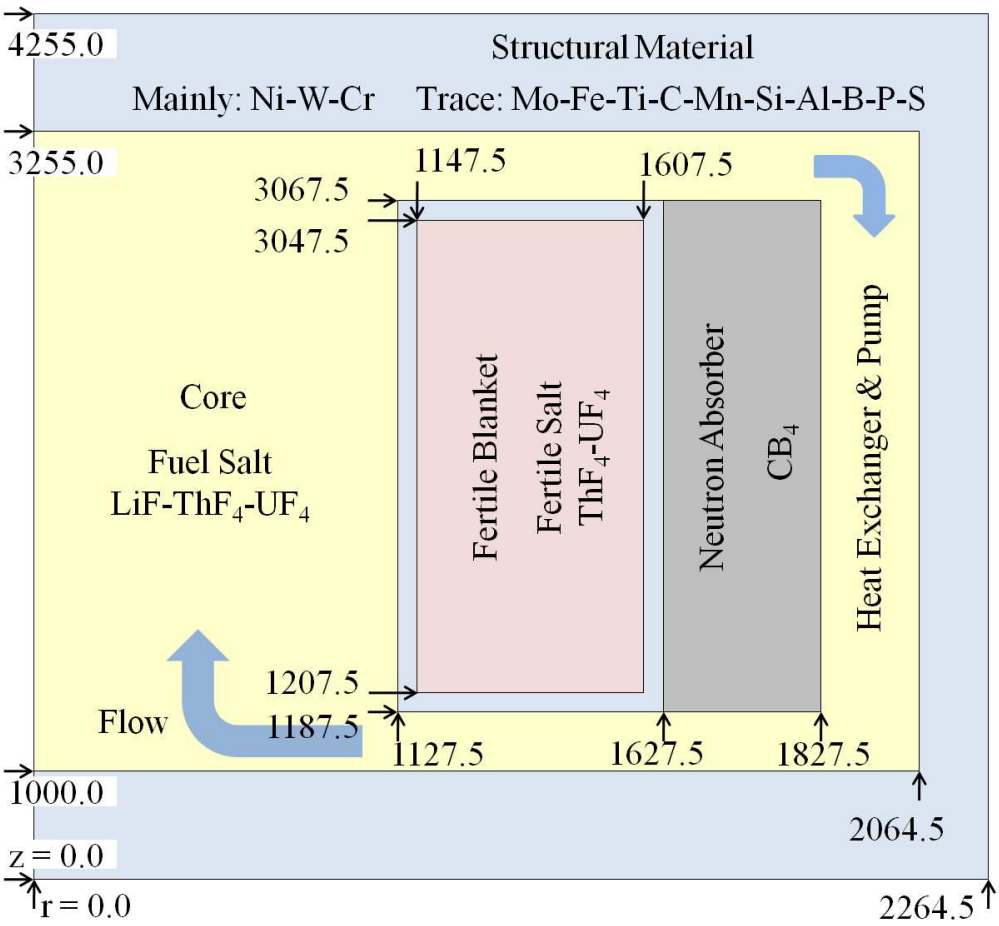

Figure 3.1 – The MSFR as modelled by IMP. Measurements and coordinates are given in mm. The total fuel salt volume is 18 m^3. Half of the fuel salt, 9 m^3, is located inside the reactor core. The other half flows through the pipes, pumps and heat exchanger, through the outer system. This outer system is simplified: no *individual* pipes or pumps are modelled in IMP. Axial symmetry is assumed instead.

3.1.2 Molten salt and structural material

Two fuel salt compositions are proposed in the Benchmark but only the U-233 containing salt was used during the thesis project. The salt composition is LiF-ThF_4-UF_4 (77.5-20-5% mol) the lithium is 99.999% Li-7. The LiF makes it a weakly moderated reactor, which results in an epi-thermal neutron spectrum, somewhere in between a fast and thermal spectrum. The fertile salt LiF-ThF (77.5-22.5% mol) is very similar to the fuel salt, the only difference is that it does not contain uranium.

One should be aware that the program IMP does not account for burn-up. Fission products are also quite literally left out of the equation - except for the precursors. It means that the salt composition does not change during calculations. This however is a good approximation for the reactor's behaviour if time intervals are kept relatively short, as is the case for the transient calculations reported below.

Table 3.1 – Fuel and fertile salt composition.

		LiF	ThF_4	UF_4
Fuel Salt x_m	[% mol]	77.500	19.985	2.515
Fertile Salt x_m	[% mol]	77.500	22.500	

The fuel and fertile salt composition is given in Table 3.1. Equation 3.1 below gives the molecular number density N_m [barn^{-1} cm^{-1}] as a function of the density ρ [g barn^{-1} cm^{-1}].

$$N_m = N_A \frac{\rho}{M} \tag{3.1}$$

M is the "molecular" weight in [g/mol] of the salt or the structural material and N_A is the Avogadro constant [6.022 10^{23} mol^{-1}]. The molecular weight M is defined by equation 3.2 below.

$$M \equiv \sum_j x_{m_j} \sum_k K_{j,k} A_{j,k} \tag{3.2}$$

The index k indicates a sum over all the constituent *atoms* of a particular molecule j in a salt (or other material). The index j indicates a sum over the *molecules* in the salt. K is the number of identical atoms in one molecule. In ThF_4 K = 4 for F and K = 1 for Th. A is the atomic weight in [g/mol] and x_m is the fraction of the molecules in the salt. For the structural material equation 3.2 may also be used, but now x_m is the fraction of atoms in the metal and K = 1.

Table 3.2 – Molar densities M for different materials used.

		Fuel Salt	Fertile Salt	Structural Material
M	[g mol^{-1}]	89.494	89.468	70.602

Equation 3.3 gives the isotopic number density N_i in [barn^{-1} cm^{-1}] - later it will be needed for calculating the cross-sections. x_i is the fraction for each isotope of a particular atom. As before, x_m is the fraction of the molecules in the salt. For the structural material x_m is the fraction of atoms in the metal and K = 1.

$$N_i = N_m \, x_m \, x_i \, K \tag{3.3}$$

Note that fluoride is found in different molecules (LiF, ThF_4 and UF_4). For F the different N_i have to be summed for each molecule: $N_i = N_{i_{LiF}} + N_{i_{ThF_4}} + N_{i_{UF_4}}$.

The atomic concentrations were calculated using equations 3.1 - 3.3, the data provided in Table 3.1 and the density ρ. Some results are shown in Table 3.3 for verification, as this is part of a benchmark process. Due to thermal expansion of the salt $\rho(T)$, the isotopic number density will change as a function of temperature.

Table 3.3 – Fuel and fertile salt isotopic number density at T = 1000 K.

		Li-6	Li-7	F	Th	U-233
Isotopic Weight A_r	[g/mol]	6.01512	7.01600	18.99840	232.03805	233.03963
Isotopic Fraction x_i	[% mol]	0.001	99.999	100	100	100
Fuel Salt N_i	[10^{-3} barn^{-1} cm^{-1}]	0.00021	21.30306	46.04256	5.47018	0.71464
Fertile Salt N_i	[10^{-3} barn^{-1} cm^{-1}]	0.00021	21.30926	46.05596	6.18662	0

The molecular number density of the fuel salt is $N_m = 27.624\ 10^{-3}$ barn^{-1} cm^{-1} at T = 1000 K.
For the fertile salt $N_m = 27.632\ 10^{-3}$ barn^{-1} cm^{-1} at T = 1000 K.

Table 3.4 – Atomic composition of the structural material.

	Ni	W	Cr	Mo	Fe	Ti	C	Mn	Si	Al	B	P	S
A_r [u]	58.693	18.38	52.00	95.96	55.85	47.87	12.01	54.94	28.09	26.98	10.81	30.97	32.06
x_m [%]	79.432	9.976	8.014	0.736	0.632	0.295	0.294	0.257	0.252	0.052	0.033	0.023	0.004
*	677.53	85.09	68.36	6.278	5.391	2.516	2.508	1.192	2.149	0.444	0.281	0.196	0.034

* Atomic number density N_i in 10^{-4} barn^{-1} cm^{-1}.

Table 3.4 shows the atomic number densities N_i for the Ni-based alloy. As the alloy's density $\rho = 10$ g cm^{-3} is assumed to be unaffected by temperature, its molecular number density N_i will also remain constant during calculations with the program IMP.

The neutron absorber is B_4C. For both the carbon and boron a natural isotopic concentration is assumed. The density is $\rho = 2.52016$ g cm^{-3}. During this project, the neutron absorber's density is assumed to be unaffected by temperature. The molecular number density N_m = 2.746676 10^{-2} barn^{-1} cm^{-1}. The atomic number densities are $N_i = N_m$ for C and $N_i = 4\,N_m$ for B.

3.1.3 Physicochemical properties

The physicochemical properties of the salt are a function of temperature and are presented in table 3.5 below. No temperature dependence was provided for the fertile salt. However, the fertile and fuel salt are very similar. Following the advice of the EVOL project Benchmark participants, the same data is used for the fertile salt during calculations.

The melting point of the fuel salt is T = 838 K. The boiling point of LiF is T = 1949 K.

For practical programming reasons the dimensions of the reactor are assumed to be constant and unaffected by temperature. This is why IMP assumes the structural materials' density to be temperature independent.

Table 3.5 – Physiochemical Properties for the fuel salt. IMP assumes exactly the same properties for the fertile salt.

		Behaviour	value at T = 700 ^{o}C
Density ρ_F	[g cm^{-3}]	4.632 - 7.526·10^{-4} $T_{(^oC)}$	4.1052
Dynamic Viscosity μ	[Pa s]	3.9943·10^{-4} exp(2812.9/$T_{(K)}$)	7.191·10^{-3}
Thermal Conductivity λ_T	[W m^{-1} K^{-1}]	0.16016 + 5·10^{-4} T$_{(^oC)}$	0.510
Specific Heat Capacity c_p	[J kg^{-1} K^{-1}]		1045

The physiochemical properties given in table 3.5 are modelled in HEAT. With this data the salt's thermal expansion coefficient β_ρ can be calculated. At $T_t = 973$ K, the salt density is $\rho_F = 4.1052$ g cm^{-3}. Using equation 2.12 we get $\beta_\rho = 1.833 \cdot 10^{-4}$ K^{-1}.

3.2 Coupling the computation programs

The software package IMP contains three constituent computational programs:

- HEAT. A CFD program which uses the finite volume method to solve the RANS equations (eq. 2.10), $k-\epsilon$ model (eq. 2.16 & 2.17) and the scalar transport equation for temperature (eq. 2.25).
- MIXER. A program that calculates the group constants i.e. the macroscopic cross-sections for each temperature and each location in the reactor.
- DALTON-MSR. It uses the finite volume method to solve the multi group diffusion equation (eq. 2.1) and the scalar transport equation (eq. 2.2) for the precursor concentration.

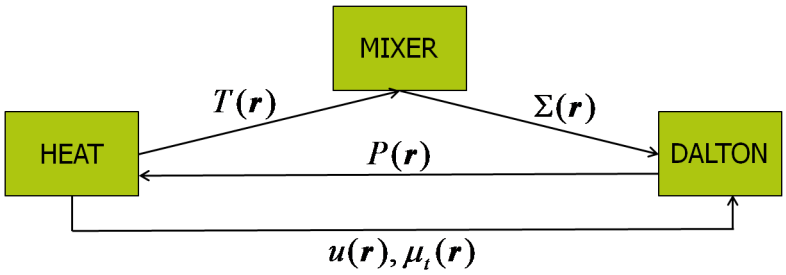

Figure 3.2 – An overview of the program IMP. It uses three other programs: HEAT, MIXER and DALTON-MSR.

Figure 3.2 gives an overview of the constituent programs that form IMP. The figure also shows how the programs are interrelated. Each program needs data from another program. HEAT needs the fission power distribution $P_f(\mathbf{r})$ as input, which is calculated by DALTON-MSR. MIXER needs the temperature distribution $T(\mathbf{r})$, which is calculated by HEAT. DALTON-MSR needs the cross-sections from MIXER and it needs the flow $\mathbf{u}(\mathbf{r})$ and eddy-viscosity $\mu_t(\mathbf{r})$ from HEAT so that it can calculate the precursor concentration and neutron flux.

Only one program can be run at one moment. A loop over the three programs is used for time dependent calculations. The script that contains this loop is a Perl script named MSFR_CC.pl. It calls a program, waits until it is finished, after which it calls the next, and so on.

It is the user's responsibility to use appropriately short time intervals. The time interval length is set in both DALTON-MSR and HEAT. It goes without saying that both should calculate an equally long time interval when they are individually called in order for the final result to be physically meaningful. Note that no time interval is set for MIXER as it only has to update the cross-sections for the current $T(\mathbf{r})$ it receives.

How fast the fission power P_f or temperature changes, determines how short a time interval should be. Due to the Doppler effect and the temperature dependent density, the cross-sections change when the temperature changes. MIXER should be called when the cross-sections have to be updated, so that DALTON-MSR calculates the correct neutron flux. Heat should be called when P_f changes. Etc. In transient calculations where fluxes quickly change, time intervals as small as $\Delta t = 10^{-5}$ s may have to be used. A time interval of $\Delta t = 0.1$ s can be used when fluxes are changing slowly.

In this thesis report a distinct difference is made between a "time interval" and a "time step". The time interval is the period of calculated time of one complete HEAT (or DALTON-MSR) run. This means that the time interval is the period between two MIXER runs. The time interval can be divided in smaller time steps. Time steps are used for the time dependent discretisation of the differential equations. Often several time steps are made during one complete HEAT (or DALTON-MSR) run. It follows that DALTON-MSR and HEAT can have different time step sizes, as long as their total calculated time interval is equal.

3.2.1 Mesh used by the numerical solvers

Both DALTON-MSR and HEAT use the finite volume method in order to numerically solve their respective equations. The axial symmetry assumed by the Benchmark makes a cylindrical coordinate system ideal for describing the MSFR in physical way. Symmetry in θ allows the three dimensional reactor (r, z, θ) to be

described by only two dimensions: the radius r and the height z. For creating the mesh of finite volumes the following was regarded.

- Enough elements should be used to obtain good accuracy. However, not too many should be used in order to avoid unnecessary long calculation times. This means an optimum should be found where the accuracy is acceptably high while the calculation time remains acceptably short. A test for the individual programs was performed to find this optimum.
- In order to obtain meaningful results with HEAT, very small volume elements had to be used near the walls, so that $y^+ < 30$ for all volume elements adjacent to the wall. DALTON-MSR did not need volume elements that small. That is mainly why it was decided to use a twice as fine mesh for HEAT as was used for DALTON-MSR, thus saving valuable calculation time.
- Data transfer between the different meshes of the different programs was realised in a practical way by making sure that the boundaries of the rougher mesh always overlap with (some of) the boundaries of the finer mesh. Figure 3.3 is implemented as an illustration. After for example DALTON-MSR has finished its calculations the power distribution P_f is passed on to HEAT. This means that P_f has to be transferred from a relatively rough mesh to a fine mesh. Without introducing additional errors, the power P_f of each larger volume element can be assigned to the smaller ones it is composed of.
- As discussed earlier in section 2.2.4, the aim was to have $y^+ < 30$ for all volume elements directly adjacent to a wall. For the MSFR this means that the size of these elements has to be small: 0.5 mm in some cases. As a uniform grid of 0.5 mm elements would lead to impractically long calculation times, hence a non-uniform grid was adopted. Sine functions are used to define the meshes in such a way that the volume elements near walls become small enough while the elements farther away are created proportionately larger. This can also be seen in figure 3.3 and 3.4. It simultaneously ensures that the condition $y^+ < 30$ is satisfied while only a limited number of volume elements is needed for making a complete mesh that models the whole MSFR. This again should lead to accurate results within a reasonable calculation time.

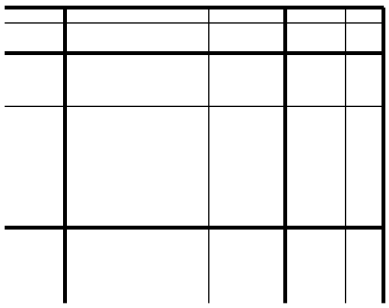

Figure 3.3 – A close-up sketch of the mesh used. The boundaries of the larger mesh always overlap with boundaries of the finer mesh. The volume elements near the wall are the smallest and those further away become proportionately larger.

Evaluations of the meshes chosen for DALTON and HEAT are reported below. The mesh, i.e. grid, of finite volumes used by DALTON-MSR and HEAT is depicted in figure 3.4.

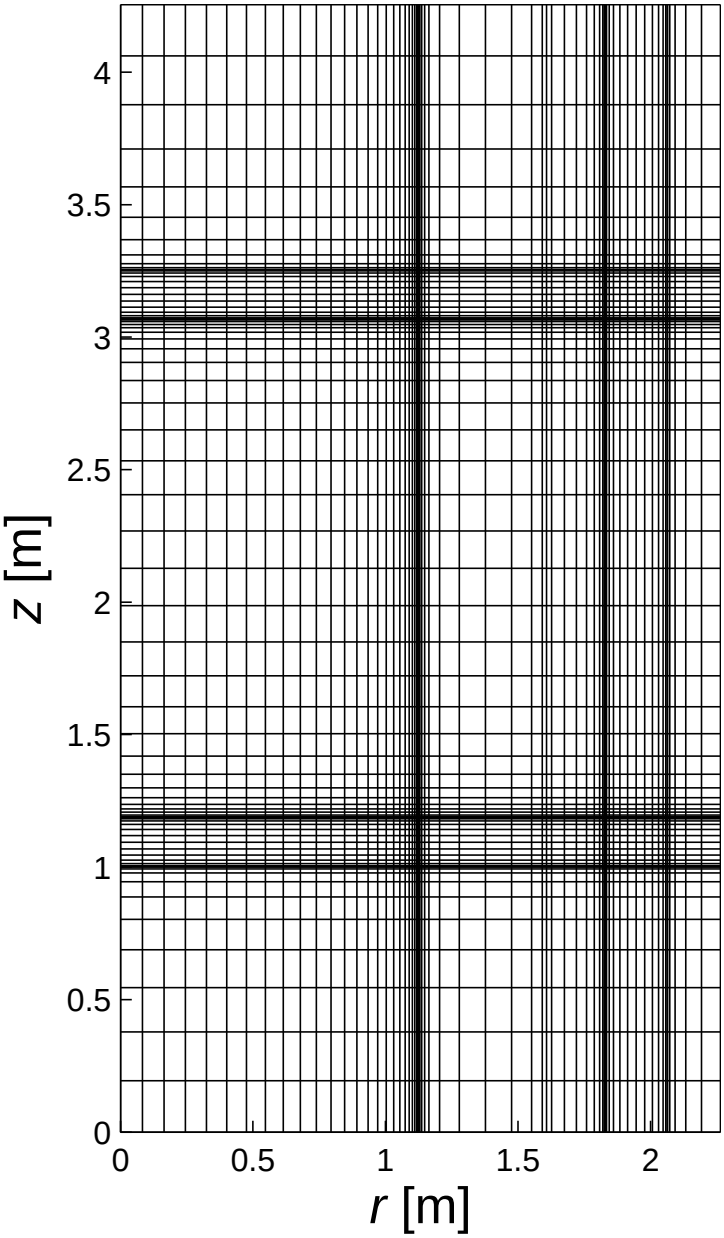

Figure 3.4 – The actual mesh used by DALTON-MSR and MIXER. The mesh is 66 radial by 78 vertical volume elements. A twice as fine mesh is used by HEAT which has (132 x 156) volume elements. The volume elements near the walls are too small for the current resolution to be resolved, i.e. lines near the walls overlap.

One additional program was written to make the (different) meshes for the three programs HEAT, MIXER and DALTON-MSR. This program is named MakeMesh. If it is desired to change the geometry, or only just the mesh, MakeMesh has to be modified, after which it has to be run just once, before new simulations are started.

3.2.2 The CFD program HEAT

HEAT is the Computational Fluid Dynamics code used by IMP. HEAT uses the finite volume method for solving the RANS equations (eq. 2.10), $k-\epsilon$ model (eq. 2.16 & 2.17) and the scalar transport equation for temperature (eq. 2.25). The finite volume method for computational fluid dynamics is thoroughly discussed by Versteeg and Malalasekera [30] and Patankar [25].

A staggered grid is used. This means that the velocity vector components are located at the boundaries of the volume elements, whereas the scalar quantities like pressure or temperature are given at the centre of the volume elements. See figure 3.5 for an illustration.

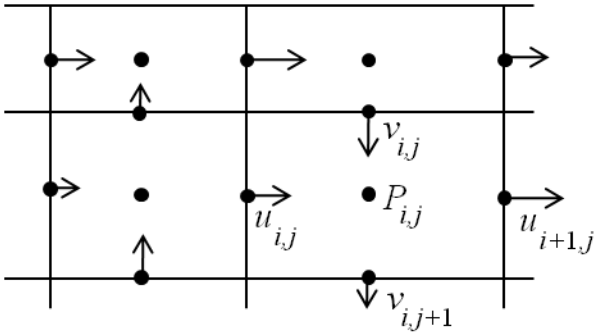

Figure 3.5 – A staggered grid. Scalar quantities are located in the centre of the volume elements. The velocity components are located at the cell boundaries. In HEAT two arrays are used: u for the radial volume velocities in the r-direction and v for the vertical velocities in the z-direction.

The law of the wall (eq. 2.22 and 2.24) is used to link the RANS and $k-\epsilon$ model for volume elements directly adjacent to a wall. Using equation 2.24 the friction velocity u_τ is isolated from the turbulent kinetic energy k. In HEAT the result, the right hand side of equation 3.4 below, is substituted in the other law equations. In this way the relation of the law functions through u_τ is realised.

$$k = \frac{u_\tau^2}{\sqrt{C_\mu}} \qquad \Longrightarrow \qquad u_\tau = \sqrt{k}\, C_\mu^{(1/4)} \tag{3.4}$$

During this project the dimensionless wall roughness parameter E in equation 2.22 is chosen to be $E = 8.432$.

The law of the wall is only valid for high Reynolds numbers [30]. As Re $\equiv 2.5\,10^6$ m s^{-1} during steady state operation this particular condition is expected to be satisfied, even if the bulk velocity decreases by one or two orders of magnitude.

Within each time step the pressure correction method, with the SIMPLE routine, [25] [30] is used to solve for u, P, k and ϵ. The convergence criteria of the SIMPLE routine is set so that the pressure correction should be < 1.0 Pa for *all* the volume elements, within each time step. As local pressures are found to be of the order of 10^5 Pa this 1.0 Pa convergence criteria is quite strict.

After the SIMPLE routine has reached convergence, yet still within the same time step, HEAT solves equation 2.25 for the temperature. The heat source term P_f should be known from a previous DALTON-MSR run.

It should be noted that the thorium atoms occasionally fission. This results in a fission power of $P_f = 0.90\,\text{MW}$ to be created within the fertile blanket, where no uranium is located. As this is only a fraction (0.03%) of the total fission power of $P_f = 3.0\,\text{GW}$, this heat is assumed to be extracted by the same system that extracts the freshly bread U-233. In HEAT the fission power produced within the fertile blanket is simply assumed to be $P_f = 0\,\text{W}$, and the heat transport in the fertile blanket is not modelled.

The heat exchanger is modelled outside the core. Figure 3.6a illustrates the location. It is modelled by equation 3.5 as fallows.

$$S_{\text{sink}} = h_{HX}\,(T - T_{\text{res}}) \tag{3.5}$$

Herein S_{sink} is the heat sink term in [W m^{-3}] and h_{HX} is a heat transfer coefficient in [W m^{-3} K^{-1}]. T_{res} = 773 K is the salt temperature in the secondary loop. In this simplified model T_{res} is assumed to remain constant under all conditions.

In the current version of HEAT no heat exchange is modelled between the structural material and the fuel salt. Instead, the average temperature of the fuel salt is assigned to the structural material. Suggestions for modelling heat-exchange between flows and walls are proposed by Versteeg & Malalasekera [30] and Guan Heng Yeoh & Kwok Kit Yuen [33]. So, in HEAT, the fission heat produced is modelled to be removed only by the heat exchanger.

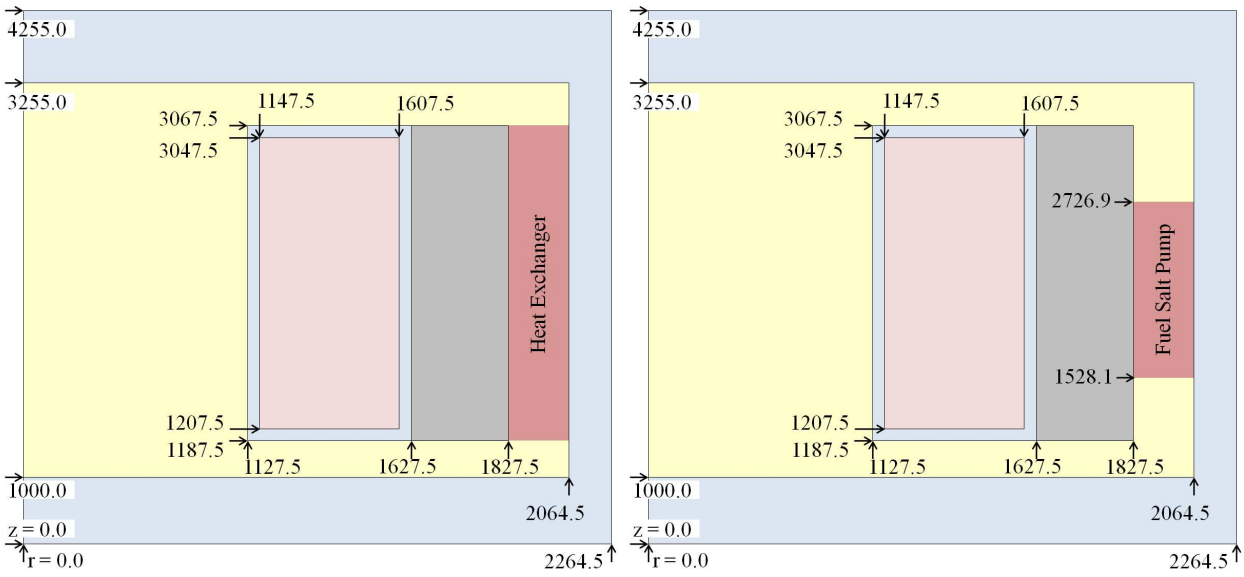

(a) The location where the heat exchanger is modelled. **(b)** The modelled location of the fuel salt pump.

Figure 3.6 – Both the heat exchanger and the fuel salt pump are located behind the neutron absorber. In the current model the pump overlaps with the heat exchanger.

Regarding the RANS equation 2.10 the pump is modelled by a body force F_{b_z}. It has the mathematical form of a pressure gradient $\frac{\Delta P}{\Delta z}$ as given by equation 3.6 below[1]. The pump has been modelled in the outer core region at the location illustrated by figure 3.6b.

$$F_{b_z} = \frac{\Delta P}{\Delta z} = \left(\frac{P(z_2) - P(z_1)}{z_2 - z_1} \right) \tag{3.6}$$

As HEAT always uses the RANS equation and the $k - \epsilon$ model, the flow must remain turbulent for results to remain physically meaningful. Again the high Reynolds numbers of Re $\approx 2.5\,10^6$ ensures that this condition is satisfied. However, some approximations are made for the MSFR modelled in HEAT. And as the model's validity is geometry dependent, experiments are still needed for validation.

3.2.2.1 Refinement of HEAT's Mesh

For HEAT an optimal mesh had to be found which leads to an accurate solution within a reasonable computation time. Many meshes were created and evaluated before a satisfactory compromise was found.

Based on these tests it was decided to use a mesh of 132 radial by 156 axial elements. This (132 x 156) mesh includes volume elements for the solid structural material. Counting the volume elements for the flow only, the final mesh contains (122 x 116) volume elements.

As an illustration, one of the evaluations is presented in figure 3.7 below. A twice as fine mesh, (244 x 232) volume elements for the flow, shows the changes that occur if a finer mesh would have been used. Given that turbulence modelling is known not to give extremely accurate results, the difference in details between the two was judged to be small enough when making a compromise between accuracy and computation time. Hence the (122 x 116) mesh could be adopted for the MSFR reactor model - with respect to the eddy viscosity.

After similar satisfactory evaluations were performed for the mean flow, pressure and turbulent kinetic energy, the (132 x 156) mesh (which includes the volume elements in the non-flowing structural material) was finally adopted for HEAT.

[1]Note that physically F_{b_z} is a body force and not a pressure, as the body force F_{b_z} generated by the pump will push the flow in the same direction of the pressure gradient, i.e. from a lower to a higher pressure.

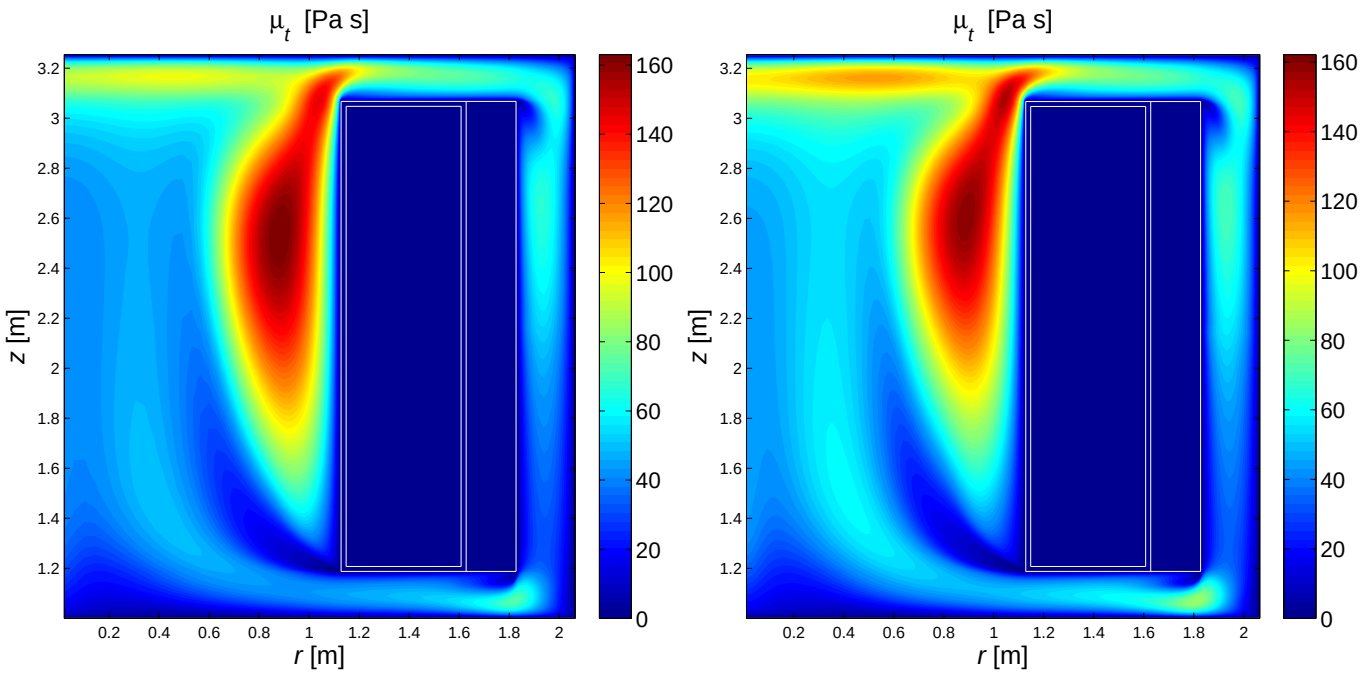

(a) The eddy viscosity calculated with a 122 x 116 (r x z) mesh.

(b) The eddy viscosity calculated with a 244 x 232 (r x z) mesh.

Figure 3.7 – The difference in details between the two solutions is judged to be small enough. Hence the (122 x 116) mesh could be adopted for the MSFR reactor model in HEAT.

3.2.3 Calculating the group cross-sections for DALTON-MSR

Temperature dependent group constant cross-sections Σ have to be provided for DALTON-MSR. The accuracy of the group constants determines how accurate DALTON-MSR's produced results can ultimately be: DALTON-MSR can only produce reliable results if its input is correct.
The process can roughly be divided in two main parts.

- In the first part different libraries of cross-sections are created for given homogeneous temperatures, at temperature intervals of 100K. These libraries have to be created prior to a simulation with IMP, and only once. During this process the geometry is approximate.
- The second part has earlier been referred to as MIXER. MIXER interpolates the group constant cross-sections $\Sigma(\mathbf{r}, T)$ for a given temperature $T(\mathbf{r})$. During a MIXER run the geometry is also exactly defined so that the MSFR rector has the geometry as described above in section 3.1.2 Reactor Design. MIXER has to be called each time the temperature, and therefore the cross-sections change.

3.2.3.1 Creating the cross-section libraries

Isotopic cross-sections σ_i strongly depend on the neutron's incident energy, as can be seen in Figure 3.8, where both the fission and capture cross-sections of U-233 are plotted as a function of the neutron's kinetic energy.
For calculating the few group constant cross-sections two steps are needed.

- **Step one**. The cross-sections are calculated for the mixture of different isotopes. The fuel salt, for example, contains U-233, Th-232, F-19 and Li-7 (section 3.1.2). The individual isotopes have very different cross-sections, and as the different isotopes shield each other, the total macroscopic cross-section is not simply the proportionately weighted sum of the individual isotopic cross-sections.

  During this thesis project the fine group cross-sections of the isotopic mixtures are computed with CENTRM's INFHOMMED, which is part of the CSASI routine of ORNL's SCALE 6. INFHOMMED references the library scale.rev05.xn238v7 which contains the individual isotopic cross-sections in 238 neutron energy groups. INFHOMMED assumes an infinitely large medium and according to the manual *"this treatment is best suited for large masses of materials where the size of each material is large compared with the average mean free path of the material."* [1] p.19. For the highest neutron energy group the mean free path is $1/\Sigma_{tot} = (7.7 \pm 0.5)$ cm in the fuel salt. As the inner core diameter and height of

225.5 cm can be considered large compared to this mean free path, INFHOMMED can be expected to produce reliable fine group cross-sections.

Using INFHOMMED, the fine group constants are determined for each of the four different materials: fuel salt, fertile salt, structural material and neutron absorber.

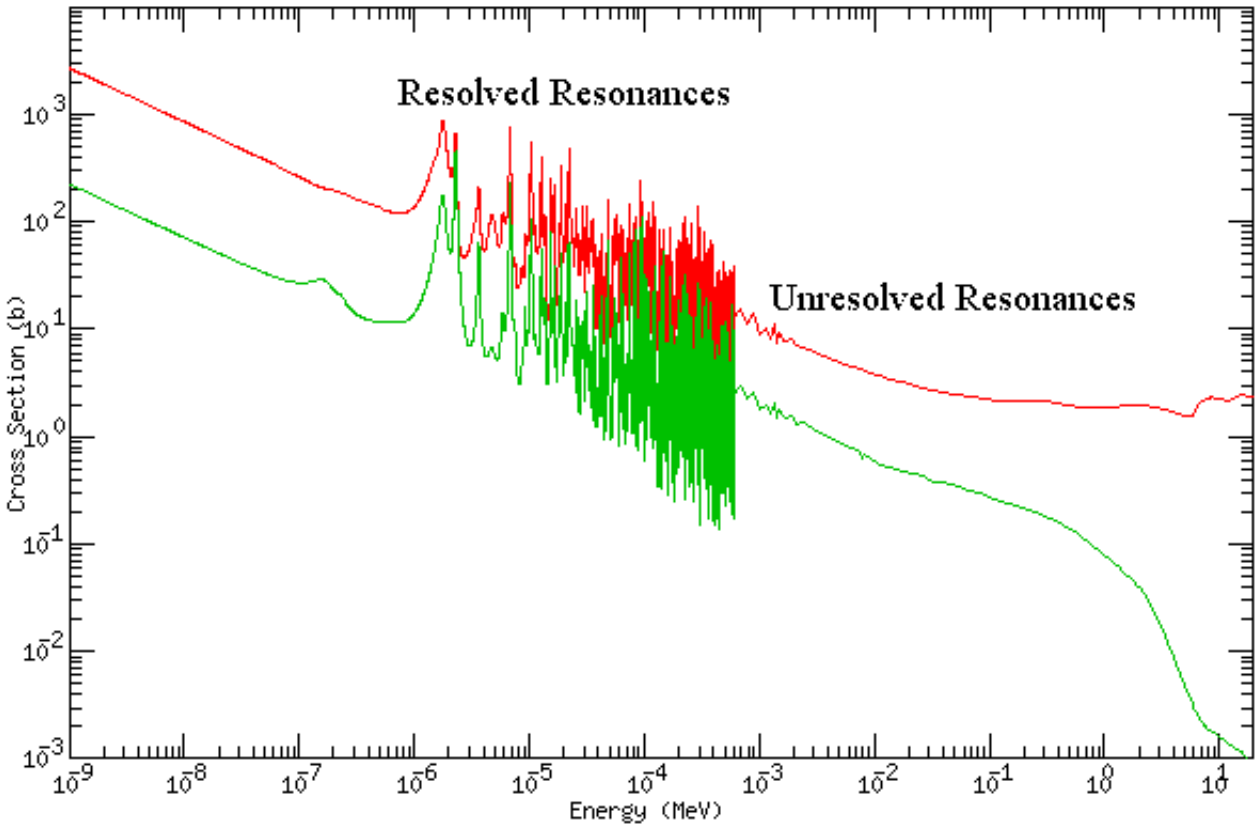

Figure 3.8 – U-233 cross-sections [2]. The **red** line represents the microscopic **fission** cross-section σ_f. The **green** line is the microscopic **capture** cross-section σ_c.

- **Step two**. The geometry will be taken in to account and the cross-sections for 238 groups are collapsed to a few energy groups. The geometry of the materials affects the local neutron spectrum and, as such, the few group cross-sections may differ as a function of space, even within the same material. The fine group cross sections produced by INFHOMMED are further collapsed with XSDRN which is also part of SCALE 6. XSDRN can account for the geometry effects, but only in one dimension, in the other two dimensions symmetry has to be assumed. In order to best represent the MSFR's geometry the few group cross-sections are calculated for two cases: for a radial dependent, axially symmetric, infinitely long representation of the MSFR, and for the axial-slab, z-dependent, infinitely wide representation of the MSFR.

  During this collapsing process performed by XSDRN, the exact same mesh will be assumed as used by DALTON-MSR. This means that the radial calculation is divided in 66 radial volume elements - and for each element one of the four materials is assigned in accordance with the MSFR's geometry, as illustrated by figure 3.9. For the axial collapsing only half of the elements have to be used as symmetry in the z-direction can be assumed. Only a temperature difference in the z-direction eliminates this symmetry in z, which is not yet of concern as the collapsing is performed for a homogeneous temperature - how temperature effects are accounted for will be reported in a moment. So, assuming symmetry in the z-direction, the axial XSDRN calculation needs only 39 axial elements for collapsing the fine group to few group constants. Figure 3.10 illustrates what the 1D mesh in XSDRN looks like for the z-direction.

  XSDRN collapses the fine group constants from 238 neutron energy groups to 9 energy groups, the boundaries of the 9 energy groups are given in table 3.6 below.

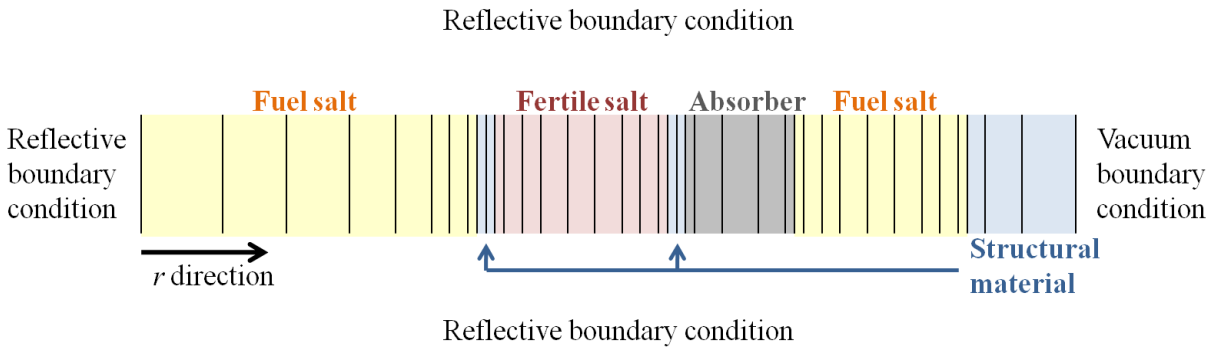

Figure 3.9 – A sketch of the 1D volume elements for the radial XSDRN calculation. The boundaries exactly overlap with the radial boundaries of the DALTON-MSR mesh, so it has 66 elements (note that in the sketch fewer elements are drawn). For each element the right material cross-sections are assigned which resulted from the INFHOMMED calculation: fuel salt, fertile salt, neutron absorber or structural material.

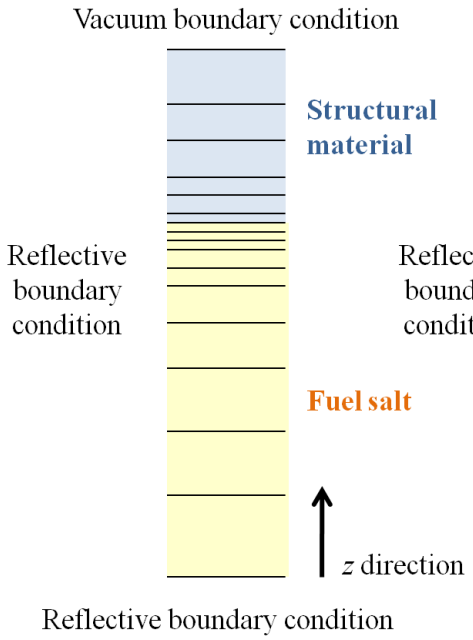

Figure 3.10 – A sketch of the 1D volume elements for the axial XSDRN calculation. Due to the homogeneous temperature, symmetry can be assumed in the z-direction. Again, the boundaries exactly overlap with the DALTON-MSR mesh. But as symmetry is assumed only half the number of elements, which is 39, have to be used. In each cell-element a material cross-section is assigned which resulted from the INFHOMMED calculation. For the z-direction this is either the fuel salt or the structural material.

Table 3.6 – The boundaries of 9 energy groups XSDRN collapses to. DALTON-MSR will use the same number of energy groups with exactly the same boundaries.

Boundary	Neutron kinetic energy [eV]
1	2.000E+07
2	1.400E+06
3	5.730E+05
4	7.300E+04
5	2.290E+03
6	1.860E+02
7	5.200E+01
8	3.325E+01
9	1.290E+01
10	1.000E-05

One run of INFHOMMED followed by the collapsing process with XSDRN takes several minutes for one temperature. During operation the temperature strongly depends on space and time $T(r, z, t)$. This affects the macroscopic cross-sections due to the Doppler effect and thermal expansion of the material. Obtaining the correct cross-sections by repeating the INFHOMMED and XSDRN calculation, for each different temperature in each diferent volume element, would simply consume too much time.

During time dependent calculations it is most practical to have several libraries readily available at certain temperature intervals $\Delta T_{libraries}$. During this project $\Delta T_{libraries}$ = 100 K. The INFHOMMED and XSDRN calculations were carried out for temperatures from T = 200 K to T = 2300 K in 100 K steps. This was performed for both the radial and axial 1D representation of the MSFR. In this way, 21 radial and axial libraries were created.

From the libraries made available, MIXER selects, for each volume element of the DALTON-MSR mesh, the correct 1D element, and makes a correct temperature interpolation. This, within a reasonable amount of time ($\Delta t \approx 60$s), so that time dependent calculations become practically feasible.

3.2.3.2 MIXER

Contrary to the libraries generated, MIXER is called during time dependent calculations. MIXER is responsible for two main tasks, so that the cross-sections can be readily used by DALTON-MSFR.

- MIXER has to provide the cross-sections for the exact geometry as defined by the Benchmark. For each 2D volume element of the DALTON-MSR mesh, MIXER has to select the correct 1D library: radial or axial. And from the library chosen it has to select the right 1D volume element.
- MIXER has to make a correct temperature interpolation for each volume element. MIXER will need two libraries for making the interpolation. For each volume element with a temperature T a library with $T_1 \leq T$ and a library with $T_2 > T$ has to be selected.

Figure 3.11 shows when for a given volume element the radial or axial library is used. The axial library will be used when a volume element in the DALTON-MSR mesh is located on the left hand side of the bold red line. The radial library will be used otherwise. As figure 3.10 illustrates, no axial cross-sections are available for the fertile blanket, hence the radial library will be used there. This formed the bases as to how the red line was drawn. The vertical red line in the core is drawn between the 15$^{\text{th}}$ and 16$^{\text{th}}$ radial volume element, where $r = 97.1$ cm. In the centre of the reactor core, at the red line, the cross-sections of the radial and axial libraries are the same for up to 3 digits.

When the radial library is used, the radial coordinate of the volume element determines which 1D element should be selected from the library. When an axial library is used it is determined by the axial coordinate, but the 2D (r,z) coordinate has to be translated to the symmetric z 1D coordinate.

This process may be best explained by the following example. Volume element (47,19) is clearly located on the right hand side of the red line. So the radial 1D library will be used. As $i = 47$ this element will be selected from two 1D libraries (one at a higher and one at a lower temperature). For the volume elements (3,19) and (3,50) the axial 1D libraries will be used.

Volume element (47,50) is a special case as it belongs to the top (or bottom) of the fertile salt tank. From figures 3.9 and 3.10 it can be seen that no 1D element exists for these - and only these - cases. The structural material that contains the fertile salt is only 2 cm thick, which means that the volume of the top and bottom of the fertile salt tank is small. Furthermore, it lays outside the core region. For these special cases it was therefore decided to use the structural cross-section from the 1D radial library. To be precise: that structural material volume element is selected, which is part of the tank, and lays between the fuel salt and the fertile salt. This is the first volume element that contains a structural material in the radial library, as seen from left to right in figure 3.9. It can be expected that these cross-sections would otherwise have been very similar. The error thus introduced can be expected to be very small if not negligible.

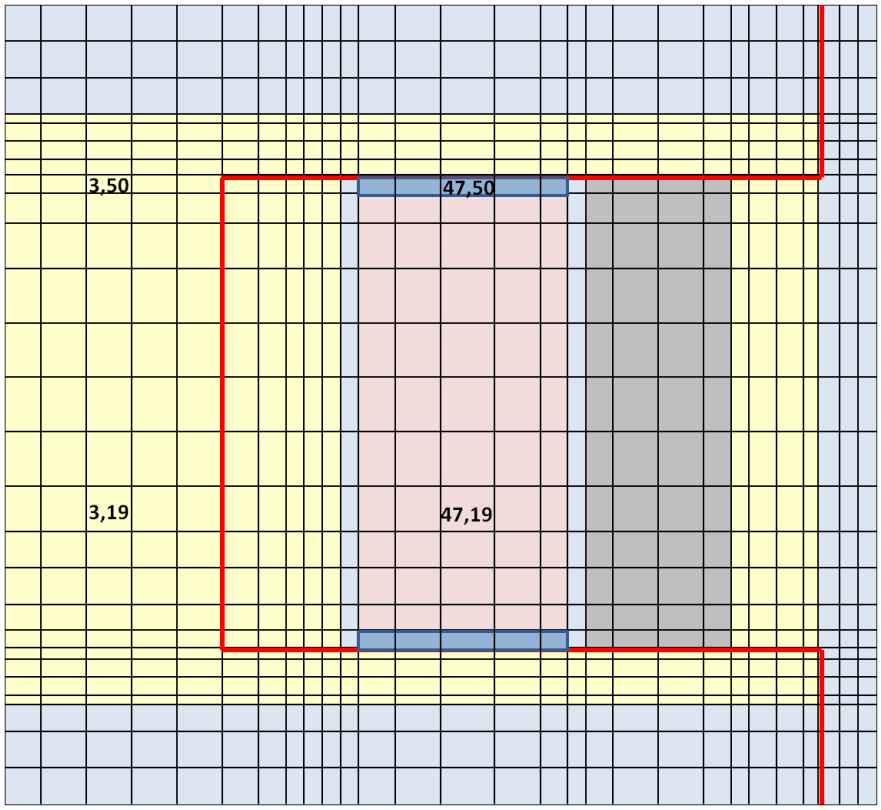

Figure 3.11 – A sketch of the DALTON-MSR mesh. MIXER uses the 1D radial and axial libraries, as illustrated by figures 3.9 and 3.10, to form the 2D DALTON-MSR mesh. After MIXER is finished the resulting newly formed 2D cross-section library can be readily used by DALTON-MSR.

For the temperature interpolation the pseudo-materials approach is used [15]. The pseudo-materials approach is given by equations 3.7 below.

$$\Sigma(T) = w_1\Sigma(T_1) + w_2\Sigma(T_2) \qquad w_2 \equiv \frac{\sqrt{T} - \sqrt{T_1}}{\sqrt{T_2} - \sqrt{T_1}} \qquad w_1 \equiv 1 - w_2 \tag{3.7}$$

T is the actual temperature of a given 2D volume element. T_1 is the temperature of the colder 1D volume element in a radial or axial library. T_1 is T rounded down in 100 K steps. T_2 is the temperature of the hotter 1D volume element in a radial or axial library and $T_2 = T_1 + 100$ K. This means that $T_1 \leq T < T_2$ where T_i is the temperature of the respective libraries.

With the calculated weights w_1 and w_2, and for each volume element, MIXER interpolates two cross-sections $\Sigma(T_1)$ and $\Sigma(T_2)$ in to one $\Sigma(T)$.

3.2.4 Solving for the neutron flux and precursor concentrations with DALTON-MSR

DALTON-MSR uses the finite volume method to solve equations 2.1 and 2.2. In DALTON-MSR the Fully Implicit Time Integration Scheme of Pautz and Birkhofer [26] is applied to the multi-group diffusion equation (eq. 2.1). The scheme enables DALTON-MSR to make time dependent calculations during which it solves for $\Phi_g(r, z, t)$ and $C_i(r, z, t)$. DALTON-MSR can also make an eigenvalue calculation, it then solves for k_{eff} in addition to $\Phi_g(r, z)$ and $C_i(r, z)$.

For solving the transport equation for precursors (eq. 2.2), DALTON-MSR uses the hybrid differencing scheme as given by Versteeg and Malalasekera [30] p155. A scheme which exploits the favourable properties of both the upwind and central differencing schemes[2].

The large matrix equation is solved with the Generalized Minimal Residual Method (GMRES). The number of iterations needed by GMRES to solve the system was significantly reduced by preconditioning the large

[2]The central scheme is more accurate but may become unbounded i.e. the matrix may fail to become diagonally dominant. This may lead to un-physical solutions. The hybrid scheme switches to the (slightly less accurate) forward scheme before this happens and thus exploits the favourable properties of both schemes.

matrix. By using the ILU preconditioner a factor of 34 fewer iterations were needed for GMRES to solve the system, which thus saved valuable calculation time.

Before DALTON-MSR can solve the transport equation for precursors (eq. 2.2), the eddy diffusion $\frac{\mu_t}{\rho_F \, \mathrm{Pr}_t}$ and the mean flow velocity $\overline{\mathbf{v}}(\mathbf{r})$ needs to be known. For each volume element HEAT writes these quantities to the file TurbDiffAndFlow.bin in binary form. They are given at each cell boundary, as illustrated in figure 3.5, so that DALTON-MSR can readily solve the transport equation with the finite volume method. During one DALTON-MSR run, the eddy diffusion and flow are assumed not to vary as a function of time, which is of no concern since HEAT, MIXER and DALTON-MSR are called subsequently, after relatively short calculated time intervals, as was earlier explained in section 3.2.

In liquids, the molecular diffusion coefficient Γ can be expected to be of the order of $10^{-9}\,\mathrm{m}^2\,\mathrm{s}^{-1}$ [32]. As HEAT can only be used for turbulent flows, the eddy viscosity will be of the order of $\gtrapprox 1\,\mathrm{Pa\,s}$, which means that the eddy diffusion will be of the order of $\frac{\mu_t}{\rho_F \, \mathrm{Pr}_t} \approx 3\,10^{-4}\mathrm{m}^2\,\mathrm{s}^{-1}$. Given that $3 \cdot 10^{-4} \gg 10^{-9}$ the molecular diffusion of the precursors Γ_i is neglected during this thesis project.

At the beginning of a time dependent calculation, DALTON-MSR either uses the flux and precursor concentration from a previous calculation or it uses Φ and C from an eigenvalue calculation. Hence, at least one eigenvalue calculation is needed, before time dependent calculations can be started. For time dependent calculations the GCR Krylov acceleration method has been found to significantly reduce computation times without compromising the result's accuracy.

During this project 9 energy groups and 6 precursor groups are used. The boundaries of the energy groups are given in table 3.6 above. The decay-constants λ_i of each precursor group as well as the delayed neutron yields for U-233 can be found in table 3.7 below [24].

Table 3.7 – Delayed neutron yields and decay constants as assumed by the MSFR version of DALTON-MSR [24].

i	λ_i $[\mathrm{s}^{-1}]$	$\nu_{d_i} = \frac{\text{delayed neutrons}}{\text{fission}} \times 100$
1	0.0129 ± 0.0002	0.053 ± 0.003
2	0.0311 ± 0.0005	0.197 ± 0.012
3	0.134 ± 0.003	0.175 ± 0.025
4	0.331 ± 0.012	0.212 ± 0.013
5	1.26 ± 0.12	0.047 ± 0.014
6	3.21 ± 0.26	0.016 ± 0.006

3.2.4.1 Diffusion vs transport

Between the salt in the core and the tank that contains the fertile salt, a strong gradient in the neutron flux was observed. This raised doubts about the validity of the diffusion approximation for the MSFR. In order to test the diffusion approximation SCALE's XSDRN was used. XSDRN is capable of using the diffusion equation as well as the more accurate transport equation. Both methods were used while everything else was kept the same so that the validity of the diffusion approximation could be tested. Results for group flux 8 are shown in figure 3.12.

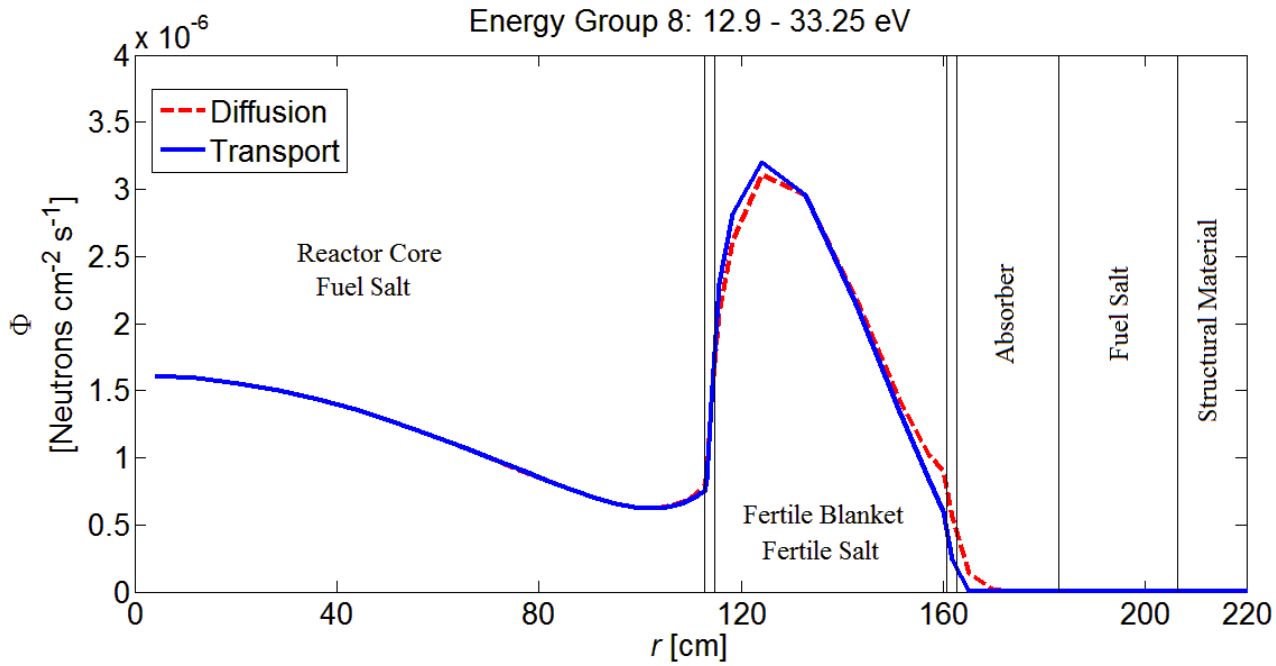

Figure 3.12 – The group flux obtained with the diffusion and transport equation. The two methods yield very similar results, especially where it matters, which is in the core region.

From what figure 3.12 illustrates it can be concluded that the discrepancy between the two results is very small. Compared to the other 8 neutron energy groups, this group flux has the strongest gradient of all. Since the diffusion equation yields accurate results for this group flux, it follows that an accuracy at least as good can be expected for the other groups. It can be concluded that the diffusion equation correctly describes the neutron flux for the MSFR reactor, and it follows that DALTON-MSFR can be expected to produce accurate results.

3.2.4.2 Accuracy as a function of the number of neutron energy groups

The effect of the number of energy groups used by DALTON-MSR has been investigated. Using more neutron energy groups generally leads to more accurate solutions. Results obtained with DALTON-MSR are given in table 3.8 below.

Table 3.8 – Increasing the total number of energy groups used by DALTON-MSR leads to a more accurate solution for the flux and k_{eff}.

Number of Energy Groups G	k_{eff}
15	1.00742
30	1.00620
60	1.00507
119	1.00141

If the collapsing process would have been perfect, no change in k_{eff} would have been observed as a function of the total number of energy groups used by DALTON-MSR. The maximum difference of approximately 600 pcm is most probably the result of a neutron spectrum that slightly varies in space, in both the r and z direction. The group constants generated with XSDRN allow for space dependence, but only either in the r or the z direction. However, the neutron spectrum, and thus the few group constants, most likely vary in both directions simultaneously. This effect is currently unaccounted for, which explains the differences in k_{eff}. The SCALE's program NEWT is, contrary to XSDRN, capable of accounting for 2D effects when generating group constants, which means that Newt may be a better choice for future work. Based on the results reported in table 3.8 the inaccuracy in k_{eff} is expected to be around $\Delta k_{\text{eff}} = 0.01$.

As the fine groups were collapsed to fewer energy groups (119, 60, 30, 15) the fine groups were combined evenly throughout the spectrum. So, the first two groups of the 238 groups are combined to form the first group

of the 119 groups, the third and fourth group of the 238 groups are combined to form the second group of the 119 groups, etc.

In a later stadium of the project it was decided not to use 15, but 9 energy groups. When the number of neutron energy groups was reduced from 15 to 9, only the groups with $E < 12.9$eV were combined: the lowest 7 energy groups of the 15 were all combined to form the 9th group, the energy boundaries of the first 8 groups were kept the same. For the 15 groups an eigenvalue calculation, different from the one reported above, found that $k_{\text{eff}} = 0.9998315$ for the 9 groups, with every thing else kept the same, $k_{\text{eff}} = 0.9998301$, a difference of only 0.14 pcm. From this it can be concluded that all neutron groups with $E < 12.9$eV can be combined into a single energy group. No up-scatter groups are needed to accurately describe the neutron flux of the MSFR.

3.2.4.3 Mesh dependency of DALTON-MSFR's solutions.

Dependency on the mesh chosen for DALTON-MSFR has been investigated in an early stage of the project, while coupling between the programs was not yet realised. The MSFR geometry, and the same version of MIXER was used as in the final version of IMP. No fuel salt flow was simulated, and a homogeneous temperature of $T = 700\,^{o}$C was assumed. The mesh was also not yet determined for HEAT and was chosen to be 84x90 volume elements for DALTON-MSFR. The boundaries of the volume elements were later chosen to be different. Nine energy groups were used, with different energy boundaries as reported above.

Two eigenvalue calculations were performed. One with a 84x90 mesh, and another one with a mesh twice as fine in both directions i.e. 168x180 volume elements. Everything else was kept the same. The following eigenvalues were found: $k_{\text{eff}_{84\text{x}90}} = 1.014928$ and $k_{\text{eff}_{168\text{x}180}} = 1.014844$, a difference of $\Delta\rho = 8.4$ pcm. The individual group fluxes were also compared, and no differences were observed, other than that group fluxes of the finer mesh had a better resolution.

From these results it can be concluded that the error introduced by the mesh used is negligible compared to the error that is introduced by the limited number of energy groups used, even when it is noted that the final version of DALTON-MSR was different in the sense as reported above e.g. the final mesh was 66x78 and not 84x90 volume elements.

3.2.4.4 Testing the routine that solves for the precursor concentration

The subroutines added to DALTON-MSR for solving the precursor transport equation were checked in two different ways. The following two tests were performed separately.

- **Test case one.** After steady state precursor concentrations $C_i(\mathbf{r}, t_0)$ were found, the production of precursors was artificially turned off. For each precursor group the $C_i(\mathbf{r}, t)$ was integrated over space, so that the total amount of precursors $N_i(t)$ was found for each group. From $N_i(t_0)$ and the well known decay equation 3.8 the total number of precursors as a function of time can now be predicted by analytical means, and DALTON-MSR should obtain the same results as predicted.

$$N_i(t) = N_i(t_0)\exp(-\lambda_i N_i(t)) \tag{3.8}$$

  The amount of precursors started with $N_i(t_0)$ and the number of precursors $N_i(t = 10s)$ calculated by DALTON-MSR and equation 3.8 are presented in table 3.9 below. At $t = 10$s, after 1000 time steps of $\Delta t = 0.01$s, there is good agreement between the numerical result and the analytical result. The numbers are in complete agreement up to 3 digits for the fast decaying groups; for the two slowest decaying groups the thirst 4 digits are in agreement. Note that the agreement between the numerical and analytical result is much better than the accuracy that can be expected resulting from the inaccuracy in the decay constants as presented in table 3.7 above. If for example the decay constant of the 6th precursor group is actually $\lambda_6 = 3.21 + 0.26 = 3.47$ s^{-1}, and not $\lambda_6 = 3.21$, then after 10 seconds $N_6(t = 10s) \approx 5$ atoms.

Table 3.9 – The total number of precursors in each group as a function of time when the production of precursors is artificially turned off.

i	λ_i $[s^{-1}]$	$N_i(t_0)$	DALTON-MSR result $N_i(t = 10\,texts)$ $\Delta t = 0.01$ s 1000 time steps	Calculated with eq. 3.8 $N_i(t = 10\,texts)$
1	0.0129	4.38809E+18	3.85709E+18	3.85702E+18
2	0.0311	6.7654E+18	4.9573E+18	4.9571E+18
3	0.134	1.395E+18	3.653E+17	3.653E+17
4	0.331	6.841E+17	2.499E+16	2.498E+16
5	1.26	3.984E+16	1.346E+11	1.343E+11
6	3.21	5.323E+15	61.29	61.00

- **Test case two.** The precursor production was turned on again as would normally be the case. In this case, the convection and (eddy) diffusion was artificially turned off. Thereafter a new steady state solution $C_i(\mathbf{r}, t_0)$ was calculated. With no transport of precursors, DALTON-MSR should now find the exact same precursor concentration as found when solving the well known precursor equation 3.9 for the steady state situation.

$$\frac{\partial C_i}{\partial t} = -\lambda_i C_i + P_{R_i} \tag{3.9}$$

The production rate P_{R_i} is defined by

$$P_{R_i} \equiv \sum_{g=1}^{G} \nu_{d_{i,g}} \Sigma_{f_g} \Phi_g \tag{3.10}$$

Solving equation 3.9 for C_i, while assuming steady state $\frac{\partial C_i}{\partial t} = 0$, yields

$$C_i = \frac{P_{R_i}}{\lambda_i} \tag{3.11}$$

This test case was performed for the volume element located at the centre of the reactor, where the neutron flux reaches the highest value. The production rate P_{R_i} is taken from DALTON-MSR and used for the analytic calculation. For each precursor group, the numerical and analytical calculation were found to be in complete agreement with each other for at least 11 digits.

From these two test cases it can be concluded that the precursor concentration is correctly solved for by DALTON-MSFR.

3.3 Converging to a steady state solution with IMP

Each individual program needs to have an initial condition before IMP can start to make coupled calculations. Figure 3.13 presents a program flow diagram which depicts which programs should be run in what other.

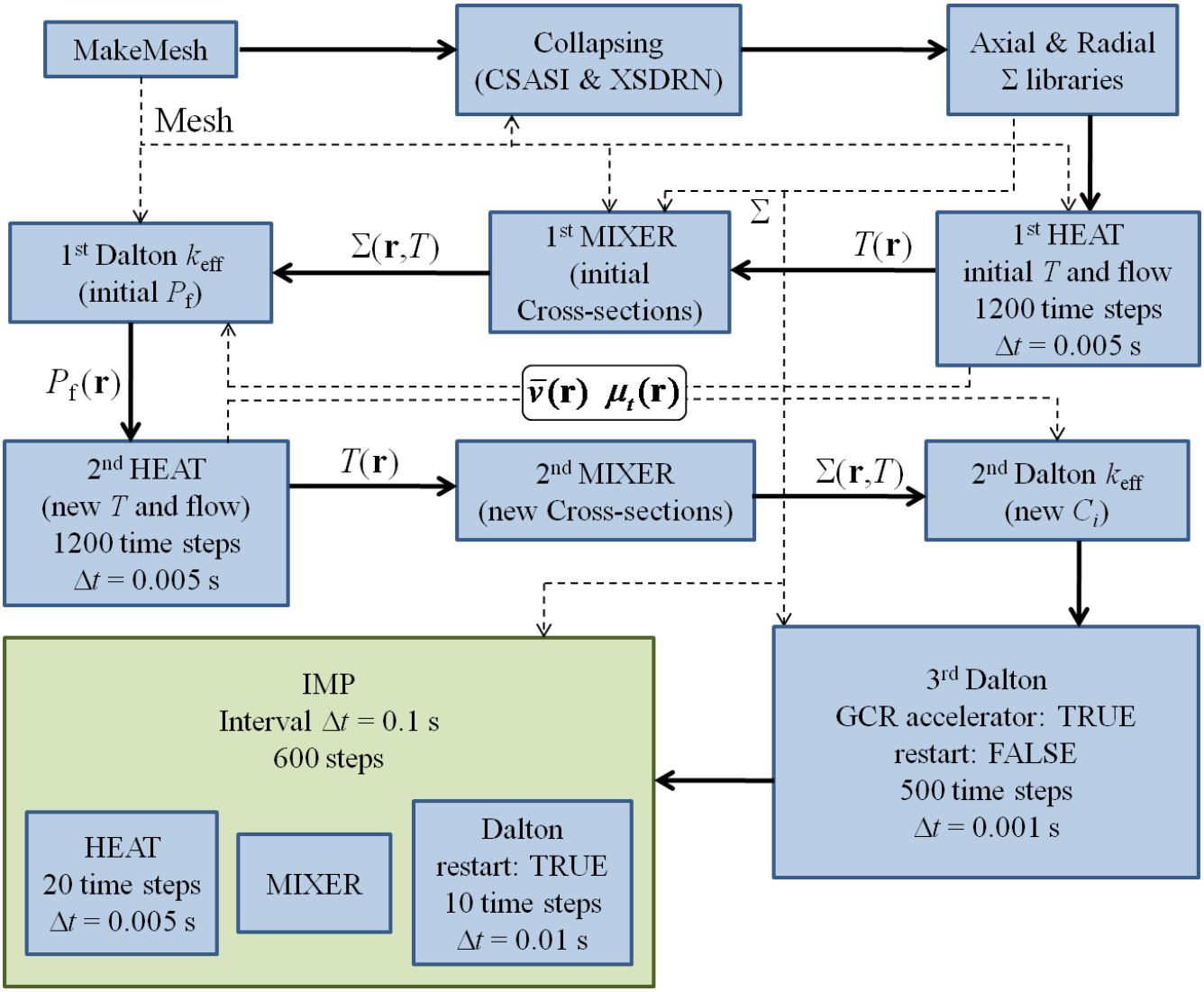

Figure 3.13 – The programs' flow diagram for setting up the initial conditions for IMP, so that IMP can solve for the steady of the MSRFR. The bold arrows indicate in which order the programs should be run. The dashed arrows indicate which parameters of importance are created as output, and needed as input by other programs.

Before the first calculations can be started, the reactor's geometry was defined and programmed in MakeMesh. MakeMesh was run first so that all the programs' mashes are known. This is also the case for the programs responsible for the Collapsing, that is CSASI and XSDRN. For the given geometry, CSASI and XSDRN produced the group constant cross-section libraries at certain temperature intervals. Libraries that are later needed by MIXER. For the first time dependent calculation with IMP, the just described sequence is executed, and it has to be repeated only after the geometry or isotopic concentrations are modified.

After the stage is set by MakeMesh, CSASI and XSDRN, an initial temperature has to be chosen. This can be realised with HEAT by defining initial temperatures in HEAT's input file HEAT_inp. Furthermore, the flag that says "use power from DALTON-MSR" has to be set to false ".F." otherwise HEAT may look for SpecificPower.bin in the DALTON-MSR directory which may not yet exist. For eigenvalue calculations the GCR accelerator should not be used. It is also advisable to turn off the heat exchanger so that no heat is extracted during the initialization precess. Only when a new mesh is created, the flag "restart" should be turned to false, so that HEAT will not try to use the flow parameters of a non-existent previous calculation.

The first time HEAT is started, it should run individually, until the flow has converged to a steady state

solution. Time steps should always be kept short: $\Delta t \leq 0.005$s was used for HEAT during this project. The calculated, i.e. simulated time needed for convergence depends on several factors but was found to be of the order of a minute for the MSFR, which corresponds to 1200 times steps.

After the first run of HEAT has finished, the flag "restart" (in HEAT's inputfile) should be turned to true, so that the found solution for the flow will be used as a starting condition the next time HEAT is started. With the flow and turbulent mixing calculated by HEAT, DALTON-MSR can now solve for the precursor transport. But, run MIXER.pl individually first[3] so that group constants are created.

Now an individual run of DALTON-MSR can be started for the first time and it has to be an eigenvalue k_{eff} calculation. See the DALTON_inp file for flags that ensure this. At the end of an eigenvalue calculation $P_f(\mathbf{r})$ will have been calculated, and is stored to disc, in the binary file SpecificPower.bin.

As SpecificPower.bin is created by DALTON-MSR a new steady state temperature field can be calculated with a second run of HEAT. Note that in HEAT_inp the heat exchanger and the "power from DALTON-MSR" flag have to be switched to true ".T." first. The calculated time needed to reach a new steady state is again about 1 minute. A second individual run of MIXER updates the cross-sections.

A second eigenvalue calculation with DALTON-MSR ensures that the precursor concentration quickly resembles the new flux distribution - which is probably quite different as was the case after the previous eigenvalue calculation (because the temperature distribution, and with it the group constants, may have changed significantly).

After the eigenvalue calculation, a time dependent calculation with DALTON-MSR must be made while the flag for restart is turned to false in DALTON_inp, so that it will not use the results of a previous time dependant calculation. With the restart flag turned to false, it will use the result of the last eigenvalue calculation. It is advisable to switch on the GCR accelerator. A small time step size of about $\Delta t = 0.001$s should be used, and 500 iterations should be made. When finished, the restart flag must be turned to true again, so that IMP will work properly. The time step size in DALTON-MSR - which is not the same as a time interval, see section 3.2 - was always $\Delta t \leq 0.01$s or smaller during transients.

It is now that IMP can be run for the first time. It has been found to be best practise to use the GCR accelerator, and use time intervals of $\Delta t = 0.1$s. IMP also has to run for a total calculated time of approximately one minute until a truly steady state solution is reached for the MSFR. The steady state solution gives the first results that will be presented in the coming sections below. The steady state solution also serves as the starting condition for each time dependent transient calculation.

[3]MIXER.pl can be found in the following directory: Scale/Interp/Version2/MIXER.pl

4 Results for the MSFR obtained with IMP

4.1 Steady state results

The following results are obtained with IMP according to the procedure in section 3.3. The flux was normalized so that $P_f = 3.0\,\text{GW}$. To pump the fuel a pressure of $\Delta p = 48.7\,10^3$ Pa is used. This results in a volume flow of $V = 6.01\,\text{m}^3\text{s}^{-1}$ and a characteristic period of $\tau = (18\,\text{m}^3)/(6.01\,\text{m}^3\text{s}^{-1}) = 3.0\,\text{s}$. Note that the characteristic period given in the benchmark is $\tau = 3.9\,\text{s}$. The fuel salt which enters the reactor core has a temperature of $T_{\text{in}} = 904\,\text{K} = 631^o\text{C}$. The fuel salt which flows out of the reactor towards the heat exchanger has a temperature of $T_{\text{out}} = 1020\,\text{K} = 747^o\text{C}$, so that $\Delta T = 116\,\text{K}$. The heat transfer coefficient of the heat exchanger was $h_{HX} = 8.31 \cdot 10^5\ \text{W m}^{-3}\ \text{K}^{-1}$

At these flow rates and temperatures, the U-233 concentration proposed by the benchmark reference design of May 2011 had to be increased by 3.37% in order to make the reactor critical. For each U-233 atom that was added, a Th-232 atom was removed. In reality, thorium absorbs neutrons, after which it decays to Pa-233, which decays to U-233. However, IMP does not account for burn-up, and the protactinium concentration is assumed to remain zero during this project. When the protactinium would have been modelled, the U-233 needed for criticality can be expected to be higher, as protactinium absorbs neutrons [8].

4.1.1 Pressure field

The steady state pressure as a function of space is given in figure 4.1. It excludes the static pressure which normally results from the gravitational force. In the "down-comer" the pump pushes the fuel salt downwards - in the direction of the pressure gradient. The pressure difference over the down-comer is the same as used for pumping the salt $\Delta p = 48.7\,10^3$ Pa, as could have been expected.

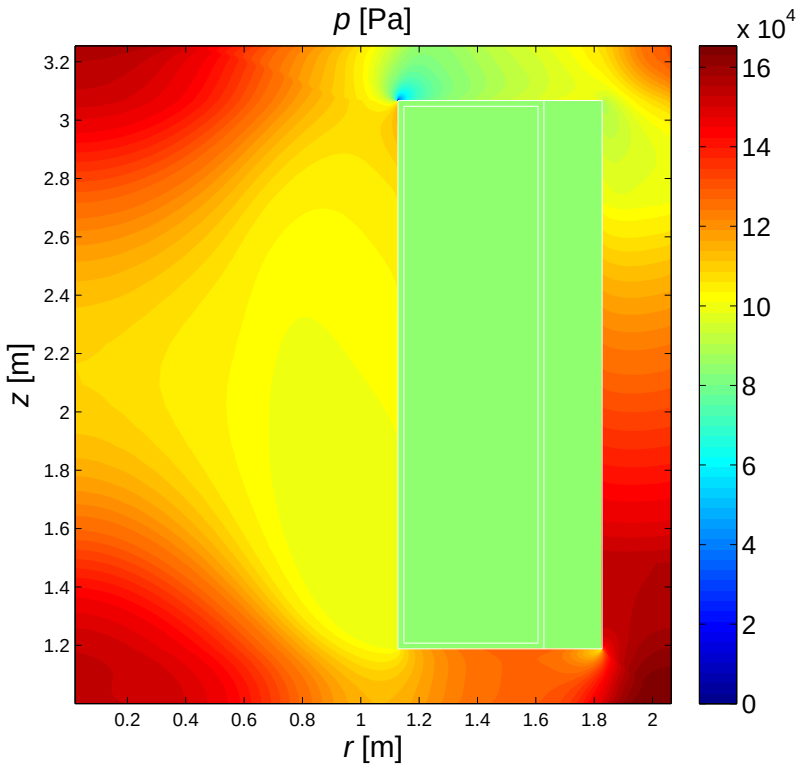

Figure 4.1 – Steady state pressure as a function of space.
The mesh for the flow has 122 x 116 volume elements.

4.1.2 Flow field

The steady state flow field is given in figure 4.2. The volume flow is $V = 6.01\,\mathrm{m^3 s^{-1}}$, which corresponds to a mass-flow of $V_m = \rho V = 24.7\,10^3\,\mathrm{kg\ s^{-1}}$ and a fuel salt full cycle period of $\tau = 3.0\mathrm{s}$. Note that time-averaged velocities are presented: local velocities will be fluctuating in both direction and magnitude, given that the flow is turbulent. Due to the cylindrical form, the velocity of the fuel salt is lower in the down-comer as compared to the core, even though the mass-flow through the core and down-comer is the same, as should be.

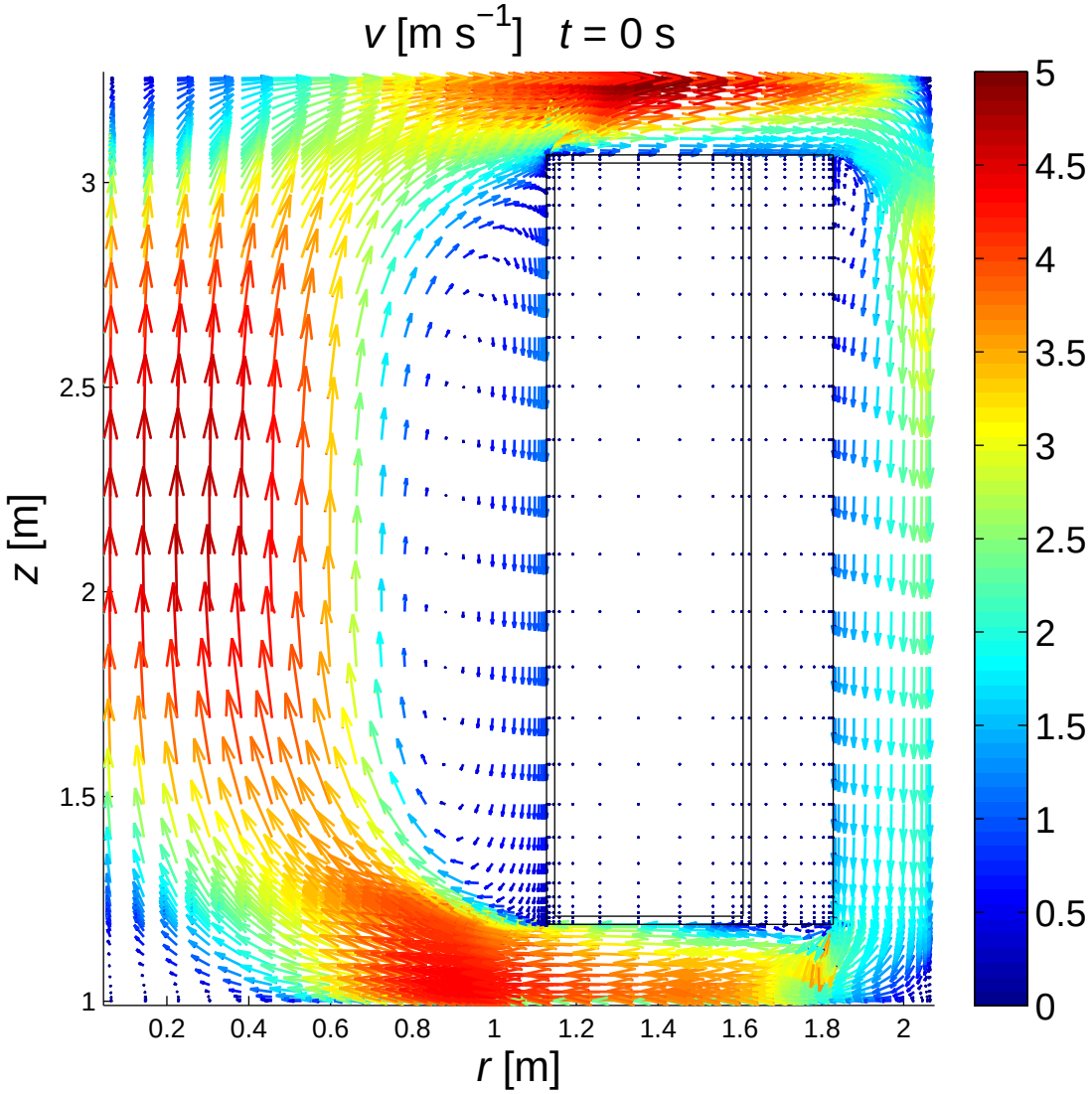

Figure 4.2 – Steady state averaged velocities as a function of space. The flow mesh has 122 x 116 volume elements and each volume element has four vectors at each of its boundaries. Only a fraction of these velocity vectors are shown. The vector's length and colour both indicate its magnitude.

Behind each corner there is a recirculation zone. In the core the recirculation is quite large. The transport of scalar quantities, like temperature or precursors, is reduced within this large recirculation zone. The solution for the temperature, given in the coming section 4.1.4, shows that the highest temperature is reached at the bottom of the large recirculation.

At higher temperatures, the rate by which the structural material corrodes, quickly increases. Finding a material that remains undamaged by the LiF salt at the high temperatures at which a MSFR operates is in fact one of the biggest challenges which have to be met before the MSFR can be realised. This is why, for a potential new design, the aim should be that no recirculation occurs. So that the maximum temperature reached can be kept to a minimum, thus increasing the life expectancy of the MSFR reactor vessel.

4.1.3 Turbulent kinetic energy, dissipation and viscosity

The eddy viscosity is plotted in figure 4.3 below. Due to the high eddy viscosity in the large recirculation zone, the scalar transport will still be significant. Just above the core inlet, where the bottom of the circulation zone is located, the velocity as well as the eddy viscosity is low.

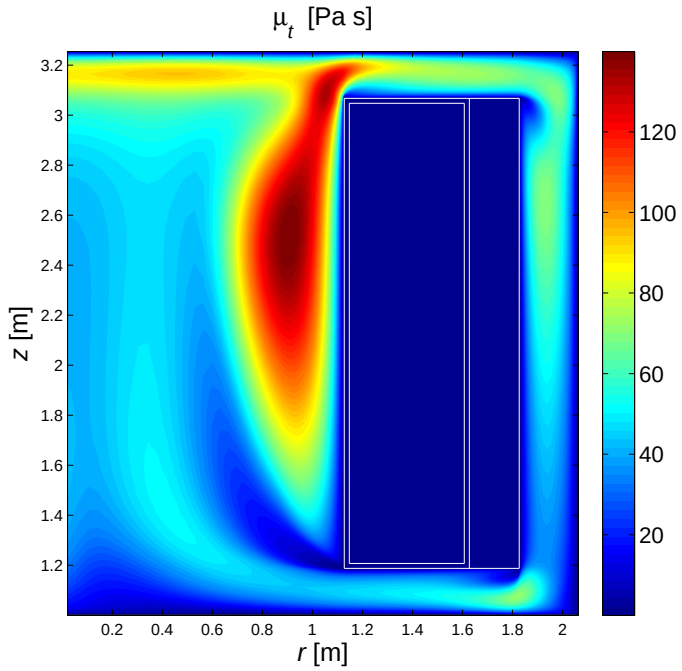

Figure 4.3 – Eddy i.e. turbulent viscosity.

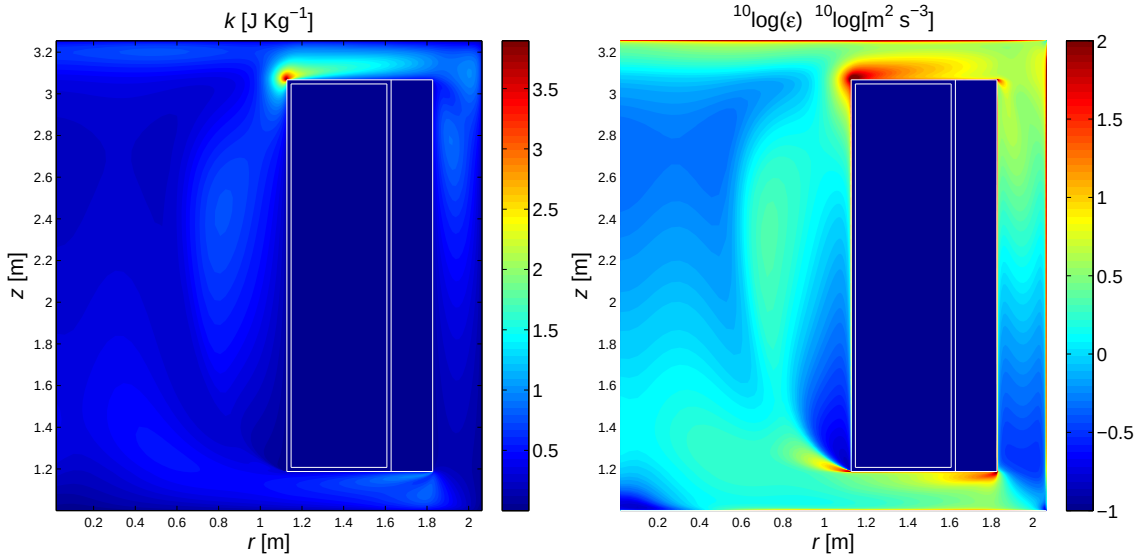

(a) Turbulent kinetic energy k.

(b) Dissipation of turbulent kinetic energy ϵ.

Figure 4.4 – k and ϵ obtained by solving the standard $k-\epsilon$ equation for the MSFR geometry.

The turbulent kinetic energy k and turbulent dissipation ϵ are presented in figure 4.4 above. Recall that the eddy viscosity μ_t is proportional to the characteristic large eddy velocity $\mathcal{V}$ and length $\mathcal{L}$ i.e. $\mu_t \propto \mathcal{V}\mathcal{L} = k^2\epsilon^{-1}$ (eq. 2.15). Also recall that $\mathcal{V} = k^{1/2}$ and $\mathcal{L} = k^{3/2}\,\epsilon^{-1}$.

There are two locations where the turbulent viscosity is high and about equal (approximately $\mu_t \approx 140$ Pa s): above the centre of the large vortex and just before the fuel salt leaves the core. Comparing the two cases, the turbulent kinetic energy k is much higher near the outlet. This means that $\mathcal{V}$ must be higher there as well. Above the centre of the recirculation zone k is smaller while the eddy viscosity is the same. It follows that here the large eddy velocities $\mathcal{V}$ are lower while the eddy length scales $\mathcal{L}$ are higher. Put differently: the eddy length scales are smaller near the outflow. That the eddy length scales are comparably smaller near the outflow and larger near the centre also makes sense given that the eddies are much more confined near the outflow than they are in the centre.

4.1.4 Temperature and specific fission power

The specific power P_f and the temperature are given in figure 4.5. The specific power is much higher in the centre of the reactor core compared to the boundaries. In the centre $P_f = 843\,\mathrm{W\ m^{-3}}$ while, at the boundaries, the fission power ranges from $P_f = 227\,\mathrm{W\ m^{-3}}$ at $r = 0\,\mathrm{m}$, to $P_f = 44$ in the corners of the reactor core.

Due to the high velocity in the centre of the core the enthalpy quickly convects to the heat exchangers. In the recirculation zone the enthalpy is mainly transported by turbulent mixing i.e. eddy diffusion. The result is that the highest temperature $T_{\mathrm{max}} = 1183\,\mathrm{K}$ is reached within the recirculation zone and especially there where eddy diffusion is low. The lowest temperature is reached after the heat exchanger and is $T_{\mathrm{min}} = 894\,\mathrm{K}$. The average fuel salt temperature is $T_{\mathrm{average}} = 996\,\mathrm{K}$.

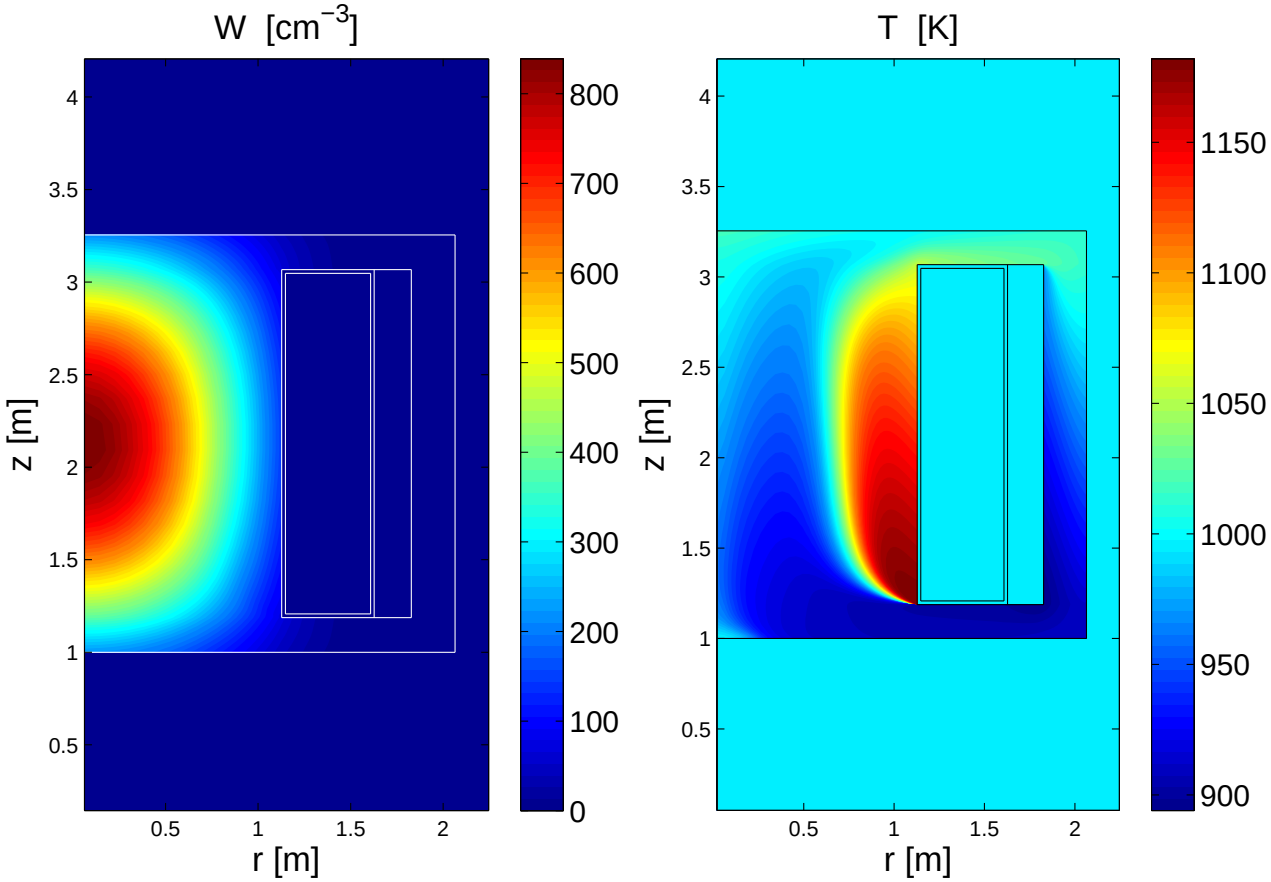

(a) Specific power produced by fission heat.

(b) Time-averaged temperature field in the MSFR.

Figure 4.5 – The heat production and transport. Heat is produced in the fuel salt. The average temperature of the fuel salt is always assigned to the structural material, fertile blanked and absorber.

4.1.5 Neutron group flux and total flux

The total flux, the sum of the group fluxes, is plotted in figure 4.6. The 9 group fluxes are plotted in figure 4.7. Note that the colour legends are different for each plot.

The highest flux is reached at the centre of the reactor core and is $\Phi = 9.66\,10^{15}\,\mathrm{s}^{-1}\,\mathrm{cm}^{-2}$. At the boundaries the flux $\Phi(r,z)$ is $\Phi(0,1) = 2.4\,10^{15}\,\mathrm{s}^{-1}\,\mathrm{cm}^{-2}$ and $\Phi(0,3.225) = 2.3\,10^{15}\,\mathrm{s}^{-1}\,\mathrm{cm}^{-2}$, while in the structural material that separates the fuel from the fertile salt, $\Phi(1.113,2.113) = 1.6\,10^{15}\,\mathrm{s}^{-1}\,\mathrm{cm}^{-2}$.

From figure 4.7 it can be concluded that the highest flux is reached in the epithermal groups. Fluxes are roughly cosine shaped. For the lower energy groups most of the neutrons are situated in the fertile blanket. In the fuel salt there is a high probability for neutrons to be absorbed by uranium, which is not the case for the fertile blanket due to the absence of uranium there. This explains why a relatively high flux is observed (only) within the fertile blanket for the low energy groups.

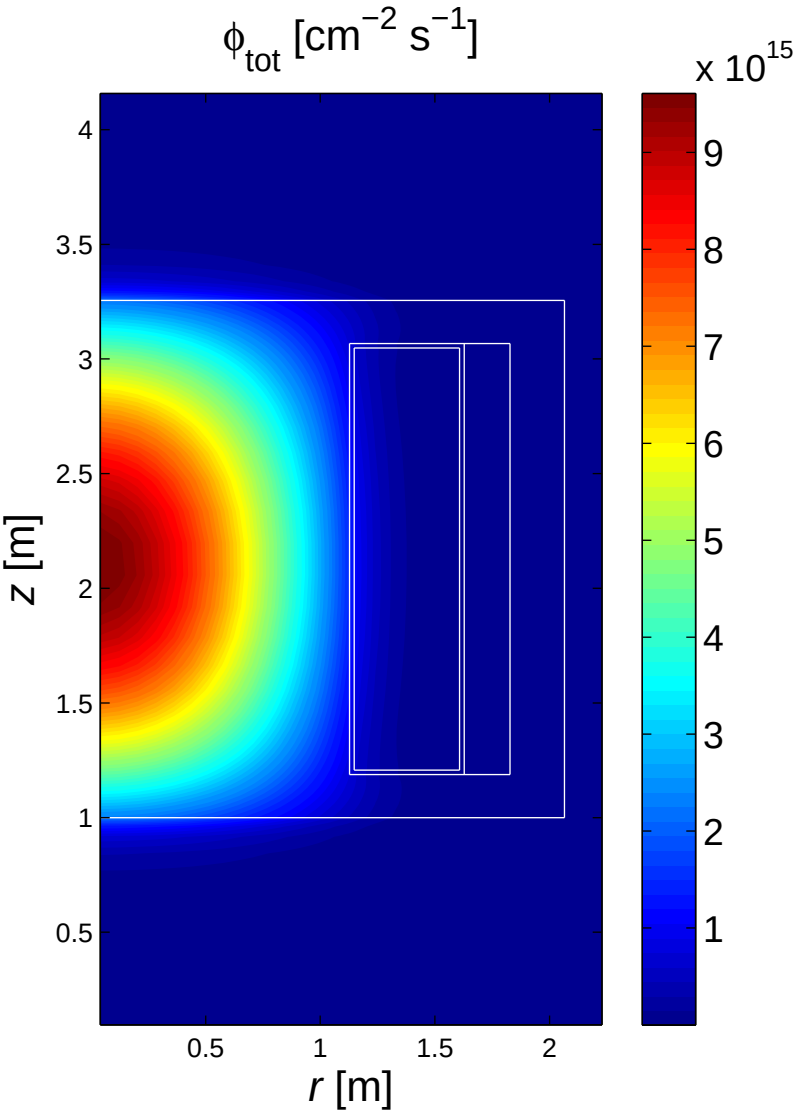

Figure 4.6 – The total flux, which is the sum of the group fluxes.

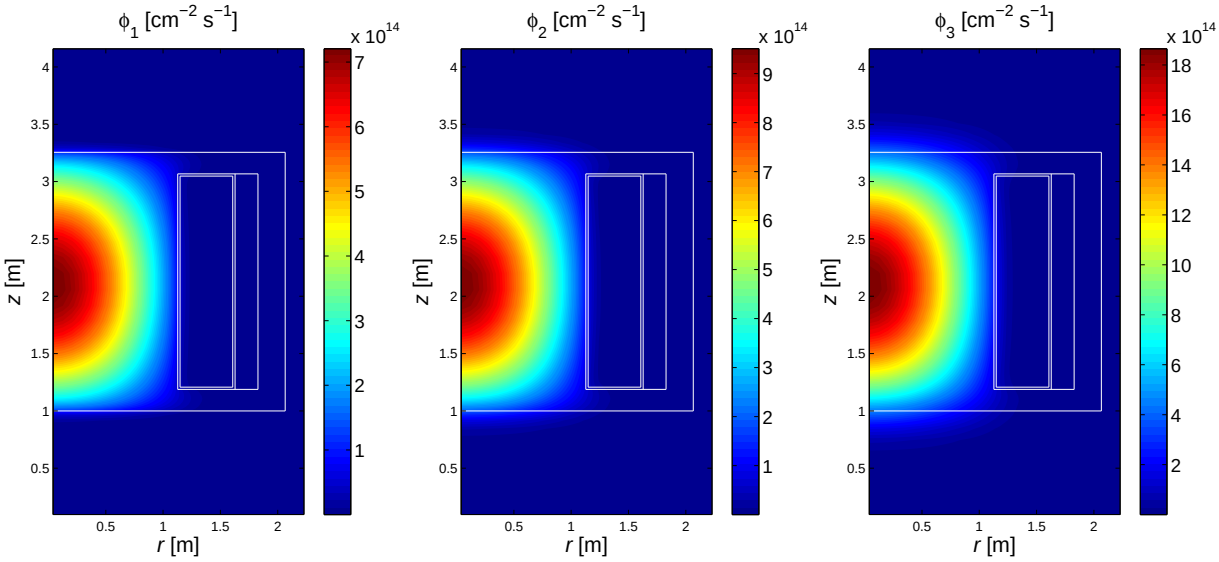

(a) 20 MeV - 1.4 MeV. **(b)** 1.4 MeV - 573 keV. **(c)** 573 keV - 73 keV.

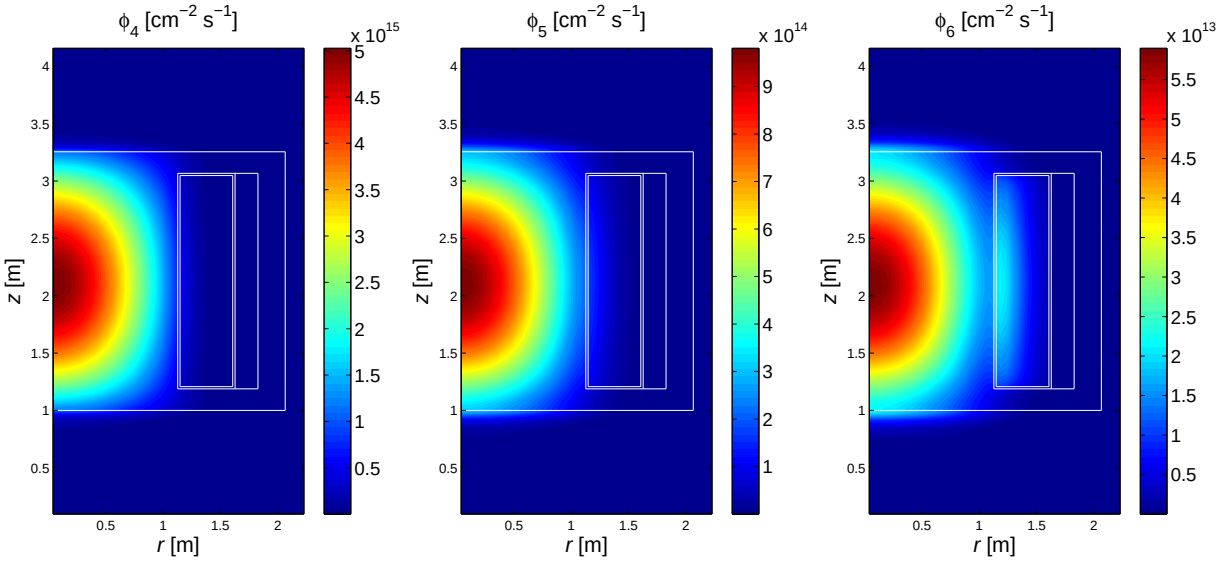

(d) 73 keV - 2.29 keV. **(e)** 2.29 keV - 186 eV. **(f)** 186 eV - 52 eV.

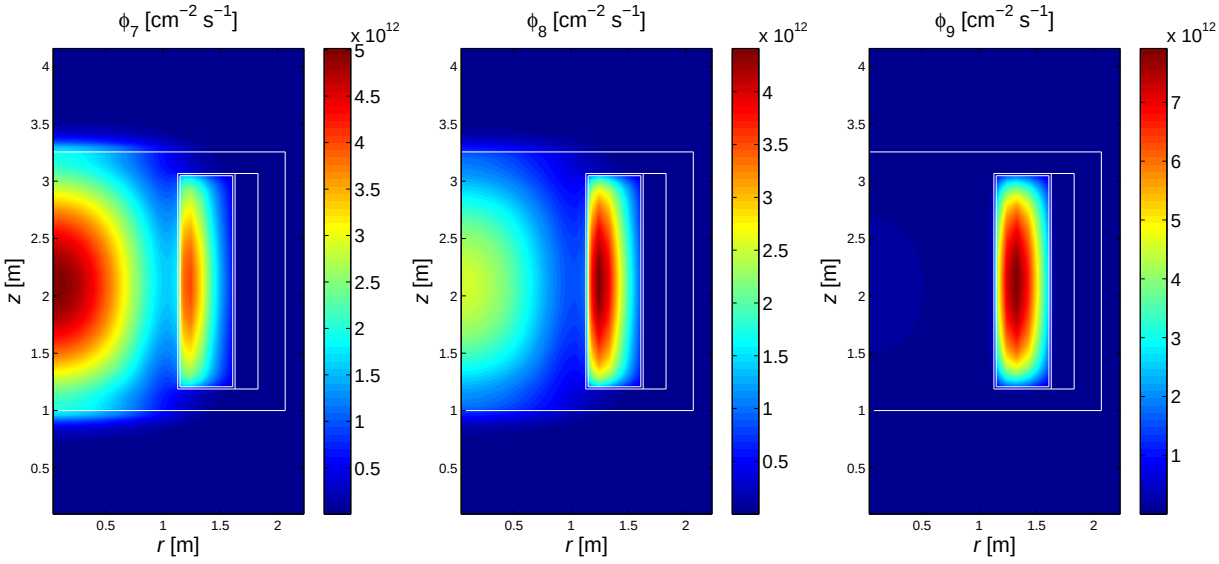

(g) 52 eV - 33.25 eV. **(h)** 33.25 eV - 12.9 eV. **(i)** 12.9 eV - 10 μeV.

Figure 4.7 – The neutron flux plotted for each energy group.

4.1.6 Neutron spectrum

The neutron spectrum located in the exact centre of the reactor is obtained with SCALE's XSDRN for 238 neutron energy groups for a temperature $T = 973\,\mathrm{K}$. Figure 4.8 shows the neutron spectrum. The flux is not scaled to $P_f = 3\,\mathrm{GW}$ so fluxes are relative.

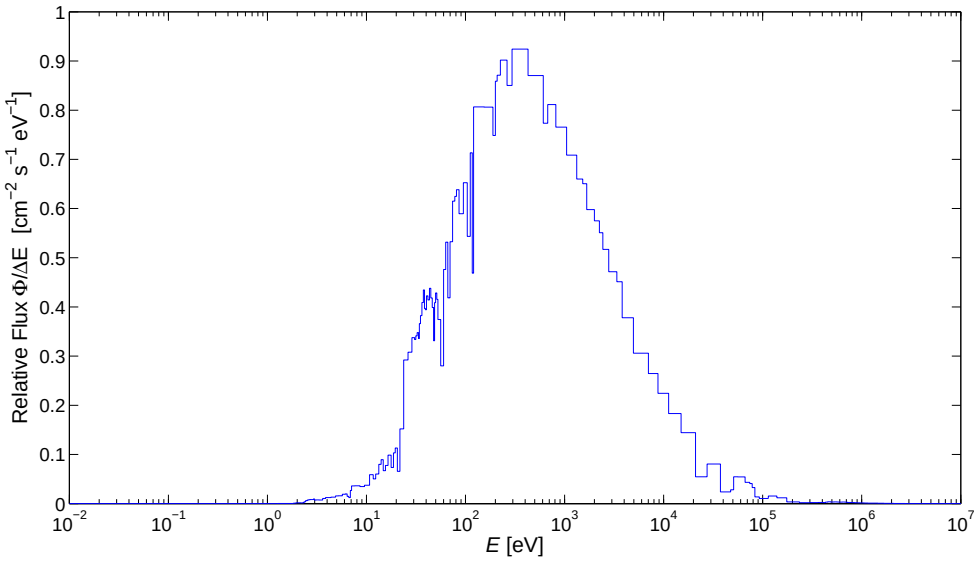

Figure 4.8 – The neutron spectrum at the centre of the MSFR reactor. 238 fine groups are used to make these plots. The neutron flux in each fine group was divided by ($E_{\text{high}} - E_{\text{low}}$) where E_{high} is the upper energy boundary and E_{low} is the lower energy boundary of the neutron energy group. This leads to [cm^{-2} s^{-1} eV^{-1}] as dimensions for the neutron spectrum.

From the plot above it can be concluded that the flux in the MSFR mainly has an epithermal spectrum. This means that the name "Molten Salt Fast Reactor" may be a bit misleading. "Molten Salt Epithermal Reactor" may be more appropriate.

4.1.7 Precursor concentration

Figure 4.9 presents the steady state precursor concentration for the MSFR. For the slow decaying first precursor group (figure 4.9a) there is plenty of time for the precursors to become almost homogeneously distributed over the fuel salt. The fast decaying precursors (figure 4.9f) decay so rapidly that only a few reach the heat exchanger. Fast decaying precursors which end up in the recirculation zone most probably decay before they can finish a full circulation. For the moderately fast decaying precursors there is enough time to make a few circulations in the recirculation zone, but there is not enough time to reach a homogeneous distribution over the fuel salt.

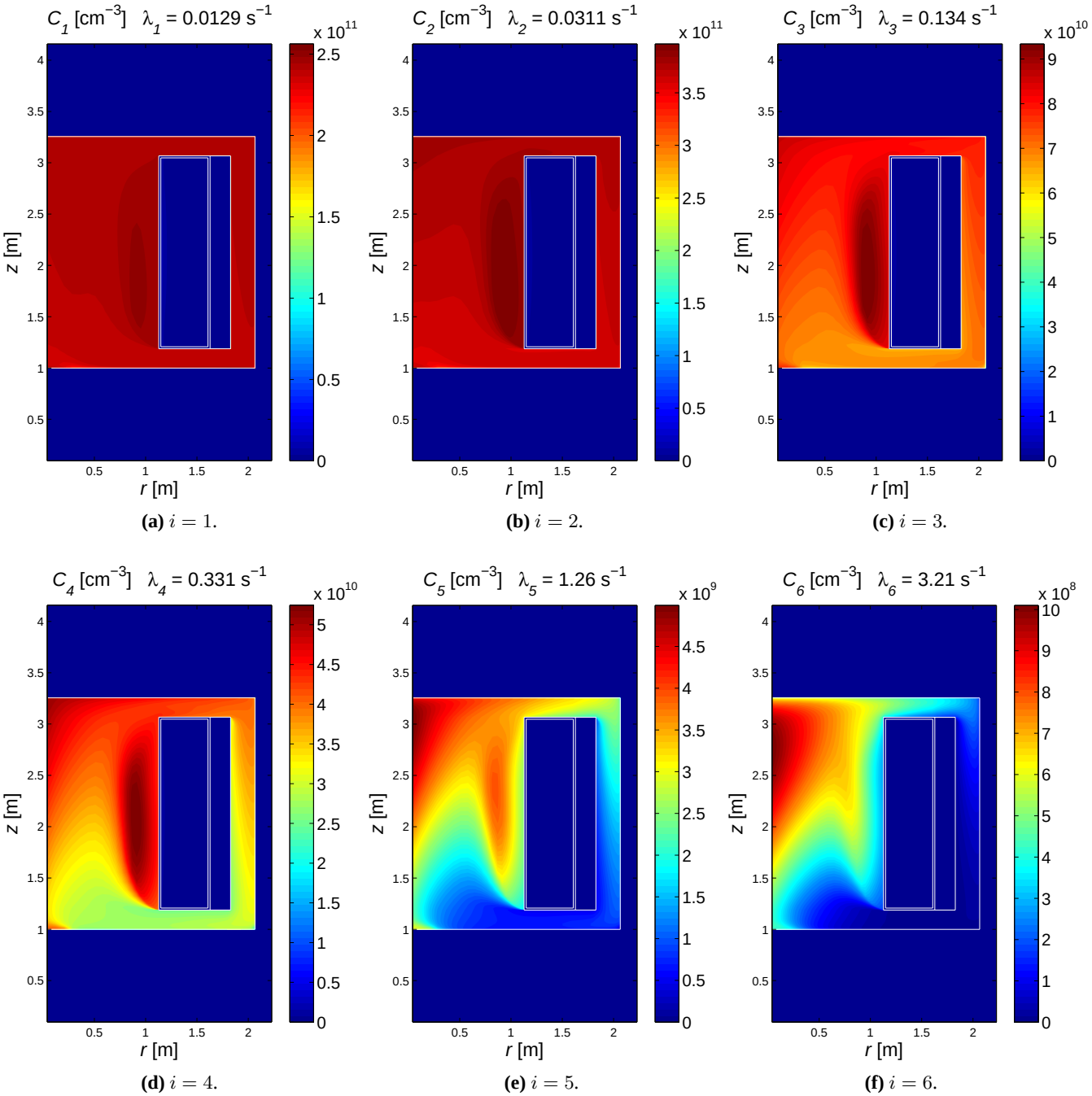

(a) $i = 1$. **(b)** $i = 2$. **(c)** $i = 3$.

(d) $i = 4$. **(e)** $i = 5$. **(f)** $i = 6$.

Figure 4.9 – Precursor concentration C_i as a function of space for the 6 precursor groups in the MSFR.

4.1.8 Precursor concentration had turbulence been unaccounted for

In order to determine the influence of the turbulence on the precursor distribution, a simulation was performed wherein only the convection was accounted for in DALTON-MSR. So, for this test, equation 2.2 becomes

$$\frac{\partial C_i}{\partial t} + \nabla \cdot (C_i \mathbf{u}) = \beta_i \sum_{g=1}^{G} \nu \Sigma_{f,g} \Phi_g - \lambda_i C_i \tag{4.1}$$

For the rest all conditions were kept the same. So in HEAT the turbulence was modelled, only $\frac{\mu_t}{\rho_F \, \mathrm{Pr}_t}$ was passed on to DALTON-MSR to artificially be equal to zero everywhere.

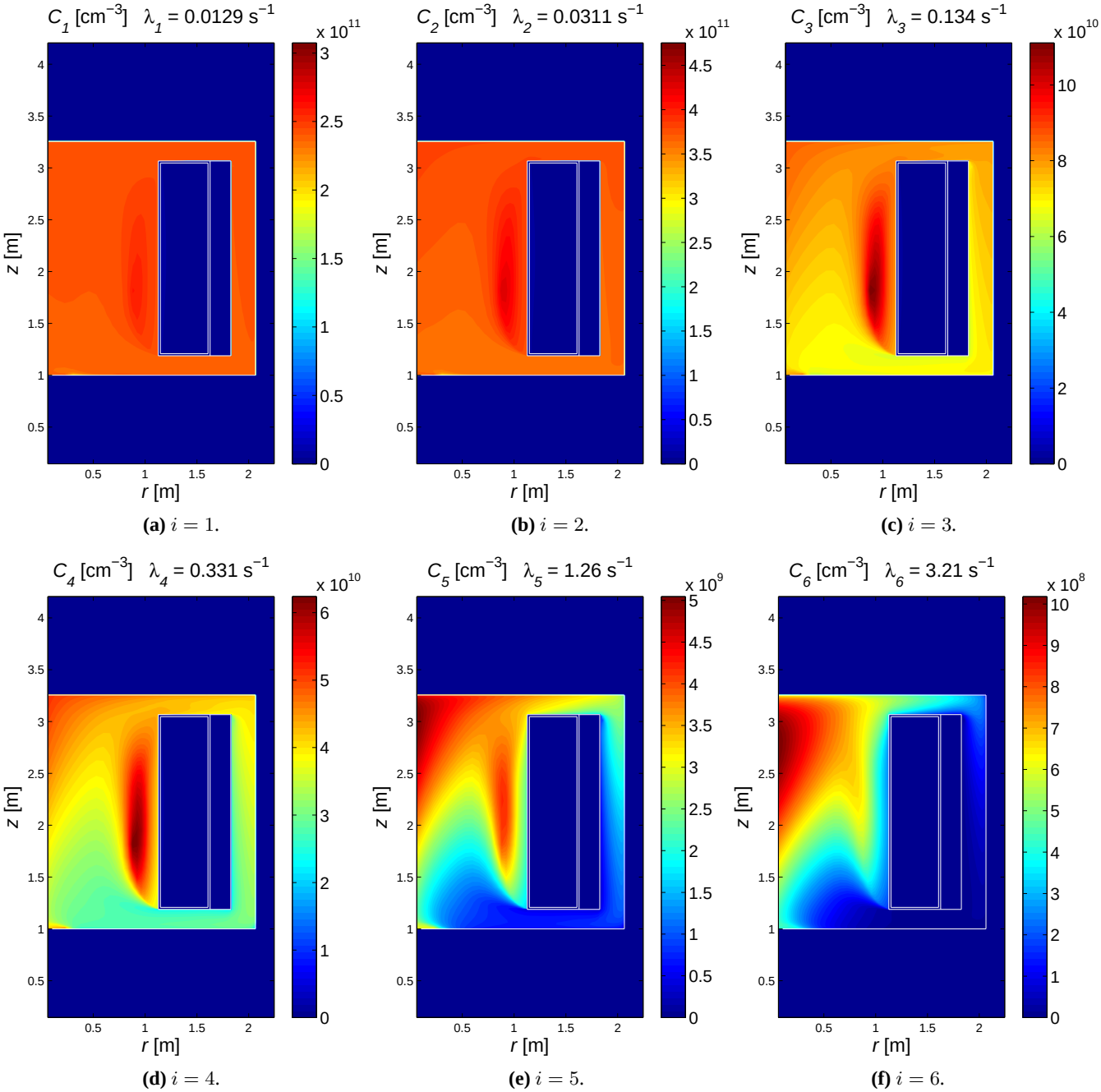

(a) $i = 1$. **(b)** $i = 2$. **(c)** $i = 3$.

(d) $i = 4$. **(e)** $i = 5$. **(f)** $i = 6$.

Figure 4.10 – Precursor concentration C_i for the 6 precursor groups when turbulent diffusion is unaccounted for. Note that the colour legends are different from figure 4.9.

Comparing the two results in figures 4.9 and 4.10 there is a clear difference in the precursor concentrations, especially where averaged velocities are low while, at the same location the turbulent diffusion is high. This is especially the case for the recirculation zone, where the difference in results is most visible.

4.2 Transient calculations

4.2.1 Heat exchanger failure

Secondary salt loops extract heat from the primary circuit via the heat exchangers. Failure of this secondary circuit might lead to safety issues. A big leak may drain all of the secondary salt or the pumps may stop working. The worst that could happen in this respect is that all heat exchangers promptly stop working, which causes the temperature in the reactor to rise. More detailed effects are investigated with IMP by simulating an immediate heat exchanger failure at $t = 0$ s. This means that no heat is extracted by any means for $t > 0$s, as no temperature transport between the walls is modelled.

In HEAT a time step size of $\Delta t = 0.005\,\mathrm{s}$ was used and 20 time steps were calculated when HEAT was called. This means that the time interval is $\Delta t = 0.1\,\mathrm{s}$. For DALTON-MSR a time step size of $\Delta t = 0.01\,\mathrm{s}$ was used and 10 time steps were calculated when DALTON-MSR was called. Shorter time step sizes and time intervals were found to produce the same results, the just mentioned ones were used in order to save valuable calculation time.

A small note should be made. During this simulation the thermal expansion coefficient was erroneously taken to be $\beta_\rho = 7.526\,10^{-4}\,\mathrm{K}^{-1}$. Instead, $\beta_\rho = 1.833\,10^{-4}\,\mathrm{K}^{-1}$ should have been used, also see section 3.1.3.

The effect of this discrepancy can however be expected to have little consequences for the final results, given that the buoyancy effect is small compared to the body force needed to pump the fuel salt. For a pump failure this does not hold. So for that scenario, reported in section 4.2.2 below, a new simulation was started with $\beta_\rho = 1.833\,10^{-4}\,\mathrm{K}^{-1}$.

For the new and correct thermal expansion coefficient a new steady state had to be reached. This steady state is used to produce the results reported in the previous section 4.1. Only for the heat exchanger failure and the instantaneous reactivity increase $\beta_\rho = 7.526\,10^{-4}\,\mathrm{K}^{-1}$ is used.

The results are given in figures 4.11 and 4.12. The failure of the heat exchanger has an almost immediate effect on the fuel salt's temperature that enters the reactor core. As the core temperature rises, the Doppler-effect and the thermal expansion of the salt ensure that the power decreases. This consequently slows the rate by which the temperature increases.

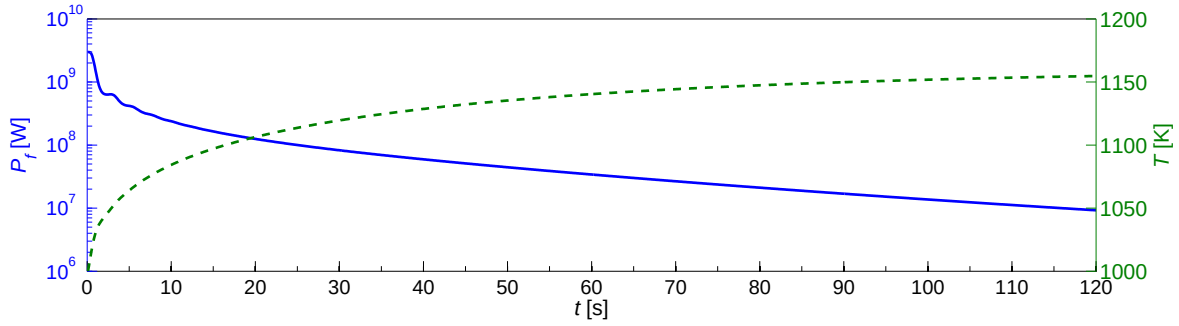

Figure 4.11 – The average temperature and total fission power as a function of time during a heat exchanger failure.

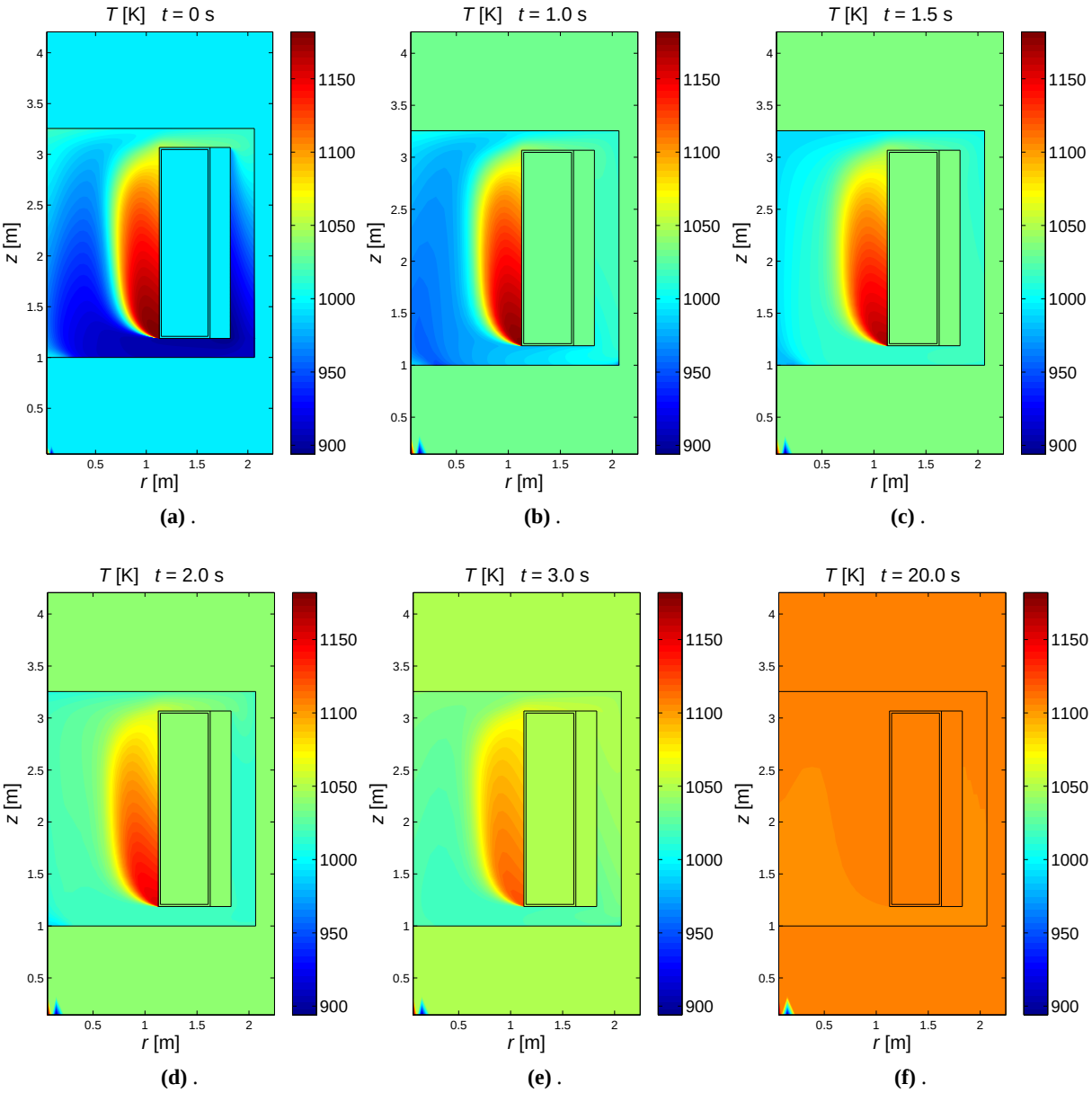

Figure 4.12 – The temperature field as a function of space during a heat exchanger failure. Note that the in the left bottom corners a red and blue pixel is depicted, this is not a result of the measurement. It is used to ensure that the colour legends for the different plots are exactly the same.

In $\Delta t = 120$s the average temperature has increased from $T = 996\,\mathrm{K}$ to $T = 1155\,\mathrm{K}$, and the total fission power has reduced from $P_f = 3.0\,\mathrm{GW}$ to $P_f = 9.2\,\mathrm{MW}$, which is 0.3% of the total starting power.

Recalling figure 2.1, about 6% of nominal power is produced as delayed fission heat, which gradually decreases as a function of time. Given that IMP does not account for a part of the fission heat to be delayed, the total fission power produced is underestimated for $t > 0\,\mathrm{s}$.

As long as IMP calculates $P_f(t) > 0.06\,P_f(t=0)$ the results will be quite accurate, but after $P_f(t) \approx 0.06\,P_f(t=0)$ which is at $t \approx 13.5\,\mathrm{s}$, the heat is mainly produced by decaying fission products. Hence, from this moment on, results produced by IMP are of limited value.

However, from IMPs results it can be concluded that the Doppler-effect and the thermal expansion of the fuel salt quickly reduce the fission rate by mere passive means. This also quickly reduces the rate of increase in temperature, which allows time for the salt to be drained in to the passively cooled sub-critical storage tanks.

4.2.2 Pump failure

Failure of the pumps has also been investigated with IMP. At $t = 0\,\mathrm{s}$ the body force which pumps the fuels salt (section 3.2.2) was instantly reduced to $F_{b_z}(t = 0) = 0$. Until $t = 0\,\mathrm{s}$ a steady state existed, as reported in the previous section 4.1. The thermal expansion coefficient was programmed to be $\beta_\rho = 1.833\,10^{-4}\,\mathrm{K}^{-1}$.

In HEAT a time step size of $\Delta t_{\mathrm{H}} = 0.005\,\mathrm{s}$ was used and 20 time steps were calculated when HEAT was called. This means that the time interval is $\Delta t_{\mathrm{I}} = 0.1\,\mathrm{s}$. For DALTON-MSR a time step size of $\Delta t_{\mathrm{D}} = 0.01\,\mathrm{s}$ was used and 10 time steps were calculated when DALTON-MSR was called. Shorter time step sizes and time intervals were found to produce the same results, the just mentioned ones were used in order to save valuable calculation time.

Results thus obtained are presented in figures 4.13, 4.14 and 4.15. Note that the scales which indicate the magnitude of the velocity vectors in figure 4.13 are different in each sub-figure.

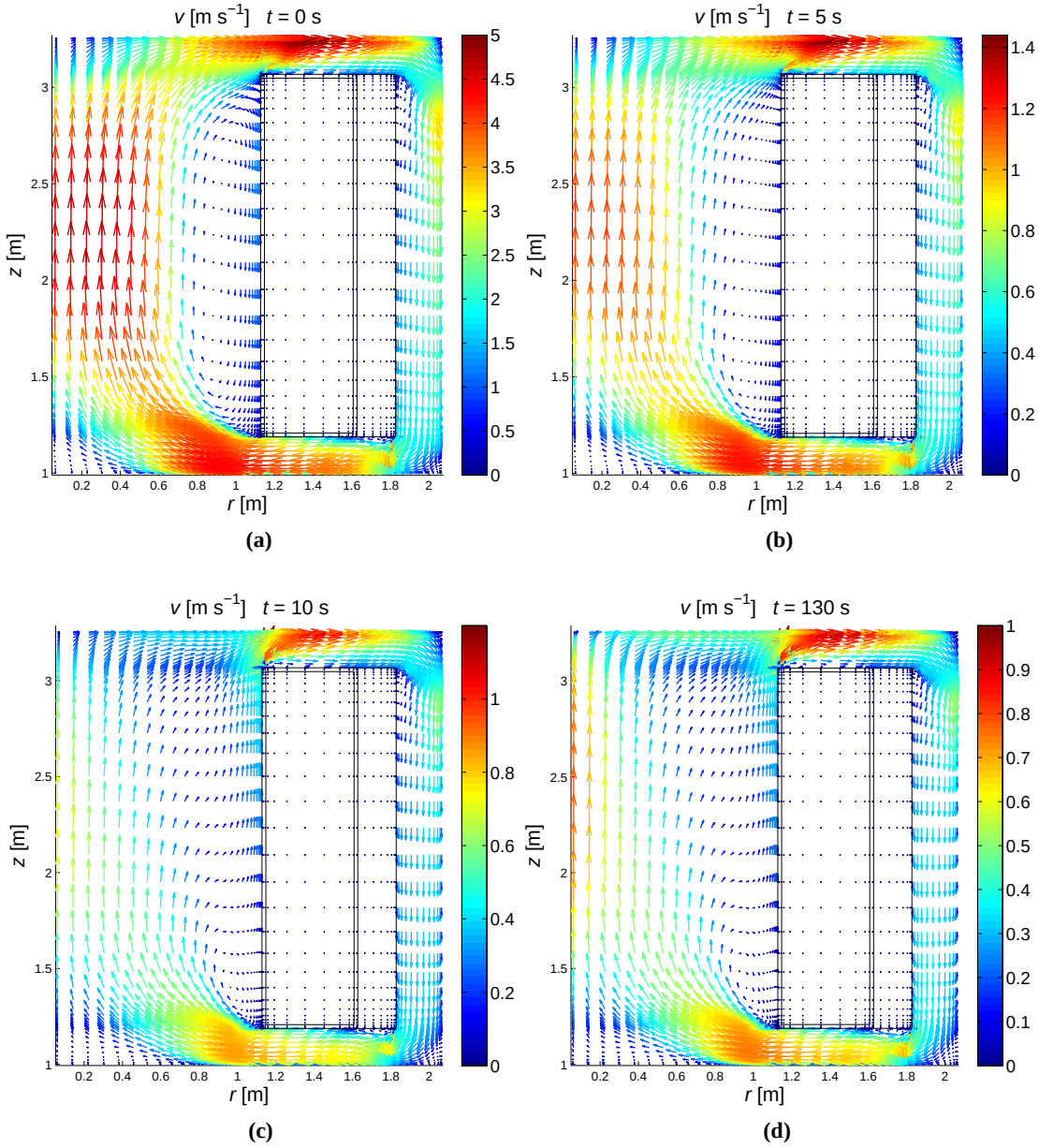

Figure 4.13 – The average velocity of the flow field at different times after a pump failure. Note that the scales of the velocity vectors are different for each sub-figure.

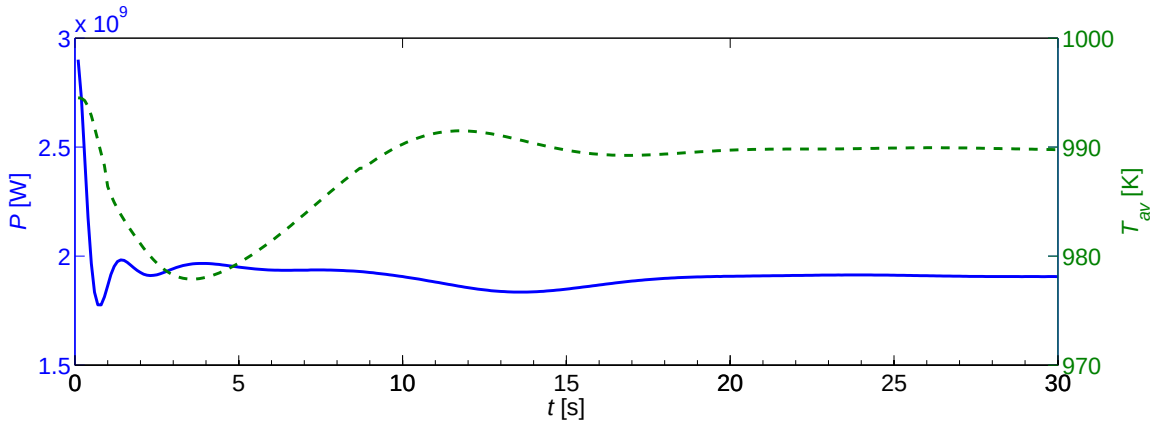

Figure 4.14 – Fission power P_f and average temperature T as function of time. P_f is given on the left hand side of the horizontal axis and plotted with a blue continuous line. T is plotted on the right hand side with a green dashed line.

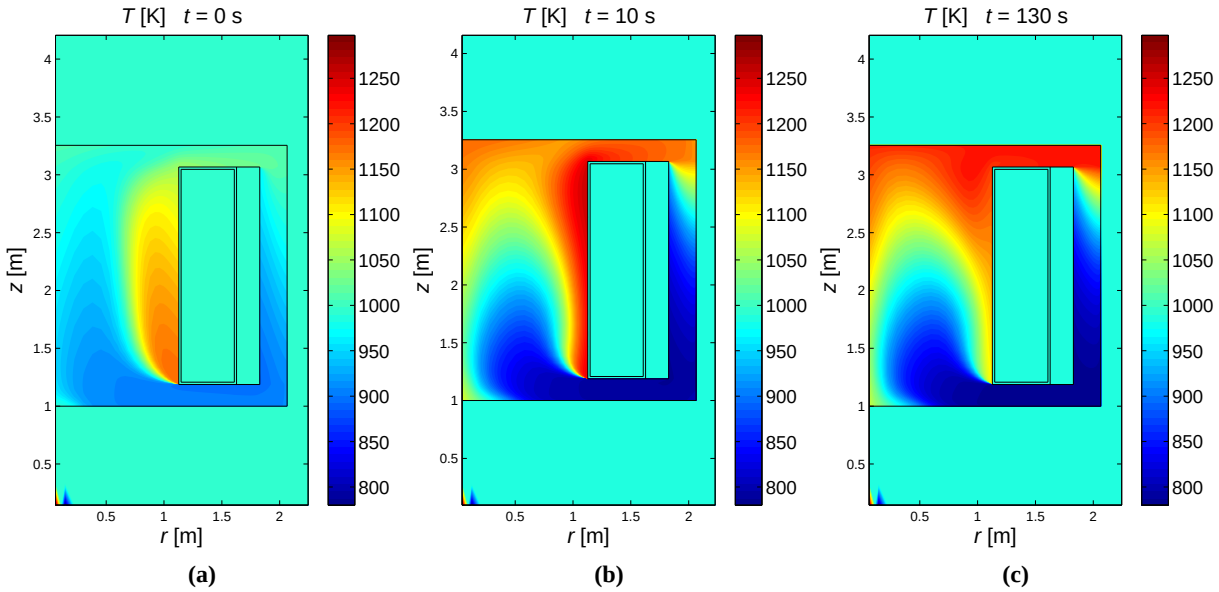

Figure 4.15 – The temperature distribution at different times after a pump failure. Again, the red and blue pixels in the bottom left corner are used for equalizing the colour legends.

During the first five seconds after the pump failure, the fuel flow speed significantly reduces (figure 4.13). In the reactor core, this leads to an increase in temperature. Due to the Doppler-effect and thermal expansion of the salt, the fission heat production quickly reduces during the thirst 3 seconds (figure 4.14).

The heat extraction rate of the heat exchanger as modelled (section 3.2.2) currently depends only on temperature and not on the flow rate. So, just after the pump failure, conditions are very similar regarding the heat exchanger, which means that it keeps extracting heat at about the same rate as it did before the failure.

The net result of the lower heat production in the core and the fairly high heat extraction in the down-comer is that the average temperature decreases during the first 3 seconds, as can be seen in figure 4.14.

As the heat exchanger still extracts heat in the down-comer, while nuclear fissions still produce heat in the core, a new steady state flow will be reached due to buoyancy effects. The volume flow reduces from $V(t=0) = 6.01\,\mathrm{m^3 s^{-1}}$ to $V(t=130) = 1.02\,\mathrm{m^3 s^{-1}}$ due to natural convection.

As the flow rate decreases, the fuel salt in the core has more time to heat up, which results in a higher

maximum temperature in the core $T_{\text{max}} = 1224\,\text{K}$ (about 150 K higher). With the lower flow rate The heat exchanger now also has more time to extract heat. As a consequence the minimum temperature decreases from $T(t = 0) = 892\,\text{K}$ to $T(t > 10) = 780\,\text{K}$ which is almost equal to the secondary salt temperature of $T_{\text{res}} = 773\,\text{K}$.

Figure 4.15 shows that, during the first 10 seconds, the recirculation zone significantly reduces in size. This somewhat reduces the relatively hot salt volume. Figure 4.15 also shows that most of the heat is extracted in the beginning, at the top part of the down-comer, where the heat exchanger is modelled. The result is that the average temperature decreases from $T_{\text{average}}(t = 0) = 995\,\text{K}$ to $T_{\text{average}}(t = 130) = 988\,\text{K}$, even though the average temperature in the core is higher - which can be concluded from the fact that the new steady state fission power produced is lower, i.e. $P_f = 1.9\,\text{GW}$.

Note that the melting point of the fuel salt is $T_{\text{melt}} = 838\,\text{K} > T_{\text{min}} = 780\,\text{K}$, which makes this simulation unrealistic in this respect, as the salt would solidify in the heat exchanger and stop the fuel flow. To avoid this the melting point of the fuel salt could be lowered by adding beryllium. The temperature of the secondary salt could also be increased so that $T_{\text{min}} > T_{\text{melt}} = 838$ at all times.

With the current MSFR's geometry it would be inadvisable to have the reactor operating in this mode, especially for long periods of time, as the structural material would much quicker corrode at these higher maximum temperatures. The pump failure transient could be much sooner stopped as simulated, by inserting control rods or by draining the fuel salt in the well known sub-critical passively cooled storage tanks.

4.2.3 Instantaneous reactivity increase

The MSFRs behaviour has been investigated for instant introductions of reactivity. In reality, such events may be caused by several actions, like a quick redraw of control rods, or by a very fast refuelling. In those cases the reactivity increase will not be instant, it may however be close to that and an instantaneous increase is the worst case scenario for such a particular event.

Whatever the reason of the introduction, for a similar increase in reactivity a similar transient behaviour can be expected. With IMP instant introductions of reactivity were modelled by changing the group constant cross-sections at t=0 s. New group constant cross-sections were prepared with the CSASI routine and XSDRN of ORNL's SCALE 6, the theory of which is reported in section 3.2.3 and the practical information is given in the beginning of section 3.3. The atomic cross-sections were exactly the same as for the cross-section libraries used for the steady state, with the only exception that a fraction of the non-fissile thorium-232 atoms were replaced with fissile uranium-233 atoms - this is realistic in a chemical way, as the valence state of thorium and uranium in the fuel salt is +4 for both atoms. Table 4.1 below gives the increase in uranium concentrations as well as the increase in reactivity that comes with it.

Increase in U-233		$\Delta\rho$
%	[kg]	[pcm]
0.1	5.06	48
0.2	10.12	102
0.3	15.18	156
0.5	25.3	265
1.0	50.6	533

Table 4.1 – Different introductions of reactivity were realised by increasing the uranium-233 concentrations. The reactivity worth was calculated with a separate eigenvalue k_{eff} calculations - this eigenvalue calculation was not ever used during the time dependent transient calculations.

Before t=0 s the well known steady state solution as reported in section 4.1 was used - with the same "old" cross-section libraries. At $t \geq 0$s the newly prepared libraries with increased U-233 concentrations were used.

The reactivity introduction of 533 pcm is discussed first, as it most clearly shows what physically happens. It is also discussed in most detail, as the physical behaviour for the other reactivity introductions is similar but less pronounced.

4.2.3.1 Instant reactivity introduction of 533 pcm

During this transient, conditions changed so rapidly that very short time intervals had to be used in the beginning. Increasingly less short time steps could be used when the flux and fission power started to change at a slower rates.

From $0 \leq t < 5$ ms time intervals were chosen to be $\Delta t = 10\,\mu$s, and only one time step was calculated during each time interval. From $5\,\text{ms} \leq t < 15\,\text{ms}$ the time interval was $\Delta t = 0.1$ ms. From $15\,\text{ms} \leq t < 115\,\text{ms}$ the time interval was $\Delta t = 1$ ms. From $115\,\text{ms} \leq t < 10.115$ s the time interval was $\Delta t = 0.01$ s; the time step size in HEAT was $\Delta t = 5$ ms, in DALTON-MSR it was $\Delta t = 0.01$ s. From $10.115\,\text{s} \leq t < 110.115$ s the time interval was $\Delta t = 0.1$ s; the time step size in HEAT was $\Delta t = 5$ ms, in DALTON-MSR it was $\Delta t = 0.01$ s.

Results for a reactivity introduction of $\Delta\rho = 533$ pcm are presented in figures 4.16 and 4.17.

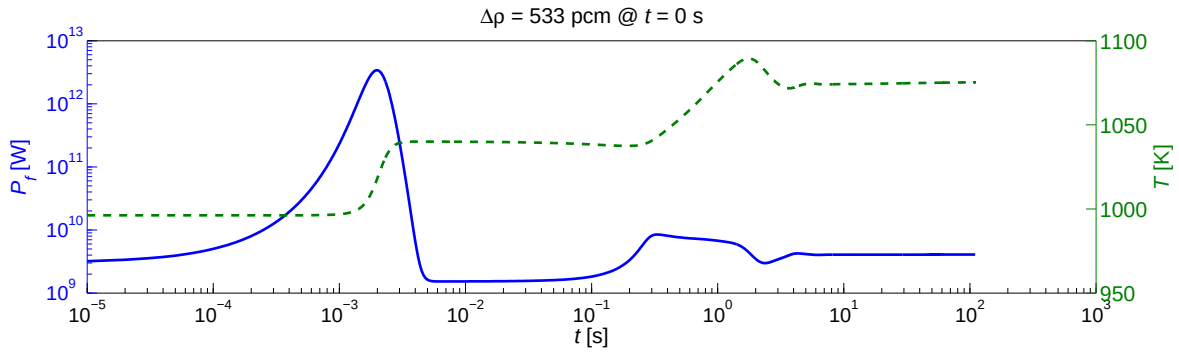

Figure 4.16 – The total fission power and average temperature as a function of time, after an instantaneous introduction of $\Delta\rho = 533$ pcm at t=0 s.

Figure 4.16 shows that during the prompt jump the total fission heat production increases from $P_f(t = 0) = 3$ GW to $P_f(t = 0.002) = 3.4\,10^3$GW. After $t \approx 0.0015$ s the prompt jump starts to measurably increase the temperature. Due to the negative reactivity coefficient, the increased temperature of the fuel salt leads to a decrease in reactivity. Figures 4.17b and 4.17c show that the average temperature is locally increased within the reactor core.

Due to the Doppler-effect and thermal expansion of the fuel salt, this increase in temperature temporarily leads to a power of $P_f(0.004 < t < 0.1) \approx 1.6$ GW, which is clearly lower than the initial steady state production rate.

Figure 4.17e shows that about $t \approx 0.1$ s the locally heat region in the core starts to exit the core region. This leads to an average decrease in temperature *within* the core, which explains why the fission power starts to rise for the second time at $t \approx 0.2$ s. Hence, the total average temperature increases for a second time.

The introduction of reactivity will after some time be compensated by an increased temperature. The new steady state temperature is $T = 1075$ K which is $\Delta T = 79$ K higher compared to the old steady state. Recalling the model used for the heat exchanger, equation 3.5

$$S_{\text{sink}} = h_{\text{HX}}\,(T - T_{\text{res}}) \tag{4.2}$$

the temperature difference $(T - T_{\text{res}})$ in the heat exchanger will now be higher for the new steady state. This means that the heat exchanger will extract more heat, which allows the fission power produced to be higher. The new steady state fission power is $P_f = 4.1$ GW.

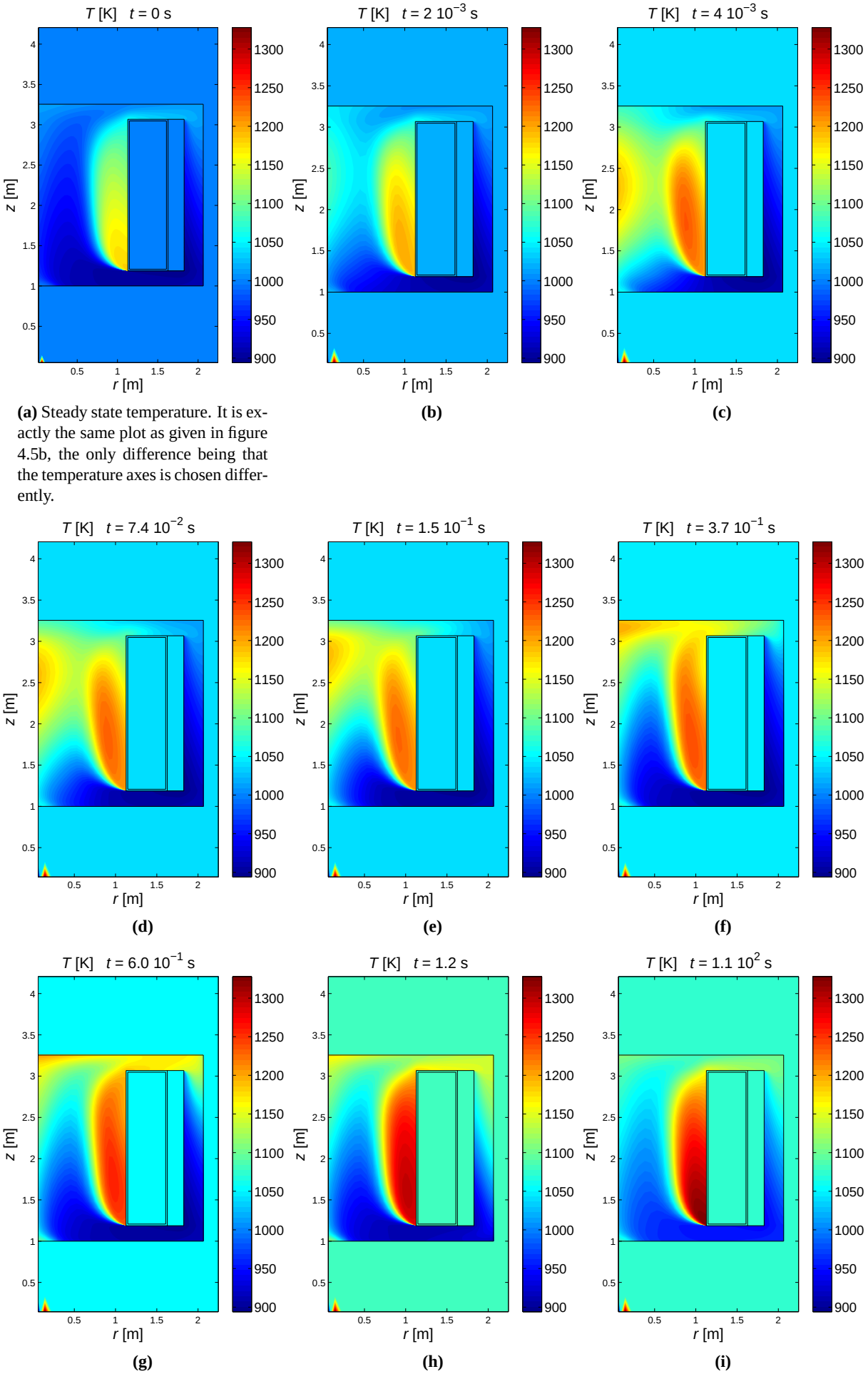

(a) Steady state temperature. It is exactly the same plot as given in figure 4.5b, the only difference being that the temperature axes is chosen differently.

(b) **(c)** **(d)** **(e)** **(f)** **(g)** **(h)** **(i)**

Figure 4.17 – The temperature as function of space, at different moments in time, after an instantaneous introduction of $\Delta\rho = 533$ pcm at t=0 s. Note that the in the left bottom corners a red and blue pixel is depicted, this is not a result of the measurement. It is used to ensure that the colour legends for the different plots are exactly the same.

4.2.3.2 Comparing the different instantaneous reactivity introductions

All the reactivity introductions modelled are given in figure 4.18 below. Be aware that some axes are defined differently for the individual sub-figures. The starting condition at t=0 s was the steady state where $P_f(t = 0) = 3.0$ GW.

The time intervals used for the reactivity introduction of $\Delta\rho = 533$ pcm have been thoroughly reported in the previous section. For the other introductions of reactivity the following time steps and time intervals were used.

From $0 \leq t < 50$ ms time intervals were chosen to be $\Delta t = 0.1$ ms, and for both DALTON-MSR and HEAT only one time step was calculated during each time interval. From 50 ms $\leq t < 150$ ms time intervals were chosen to be $\Delta t = 1$ ms. From 150 ms $\leq t < 1.15$ s time intervals were chosen to be $\Delta t = 10$ ms; the time step size in HEAT was $\Delta t = 5$ ms, in DALTON-MSR it was $\Delta t = 10$ ms. For $t > 1.15$ s time intervals were chosen to be $\Delta t = 0.1$ s; the time step size in HEAT was $\Delta t = 5$ ms, in DALTON-MSR it was $\Delta t = 10$ ms.

From the results in Figure 4.18 the following can be concluded. For the smaller reactivity introductions, the conditions change relatively slowly, as can be seen in figures 4.18a and 4.18b. For these cases the new steady state is not much different from the original one.

For reactivity introductions of $\Delta\rho = 156$ pcm and more, i.e. figures 4.18c and later, the MSFR qualitatively behaves the same as compared to the reactivity introductions of $\Delta\rho = 533$ pcm, the behaviour of which is extensively discussed in section 4.2.3.1 above.

The reactivity introduction of $\Delta\rho = 533$ pcm is, with $\beta = 0.00292$, equivalent to 1.8 \$. The results in section 4.1.7 demonstrate that a large fraction of the precursors decays outside the reactor core. This means that for the MSFR the meaning of a dollar is different as compared to a reactor wherein the precursors are unable to migrate. Due to migrating precursors, a smaller fraction of the neutrons in the MSFR core will be delayed. Hence, for $\Delta\rho = 1.8$ \$ the MSFR is more super prompt critical, for the same reactivity increase in dollars, as compared to a reactor wherein the precursors would have been unable to migrate.

From this, and the results reported, it can be concluded that the MSFR's fuel salt temperature stays well below the boiling point, even when it becomes super prompt critical at $\Delta\rho = 1.8$ \$.

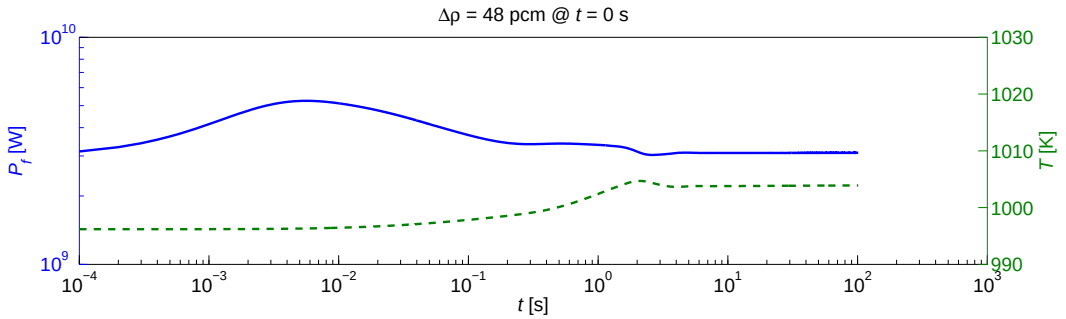

(a) For the new steady state $P_f = 3.1\,\text{GW}$ and $T = 1004\,\text{K}$.

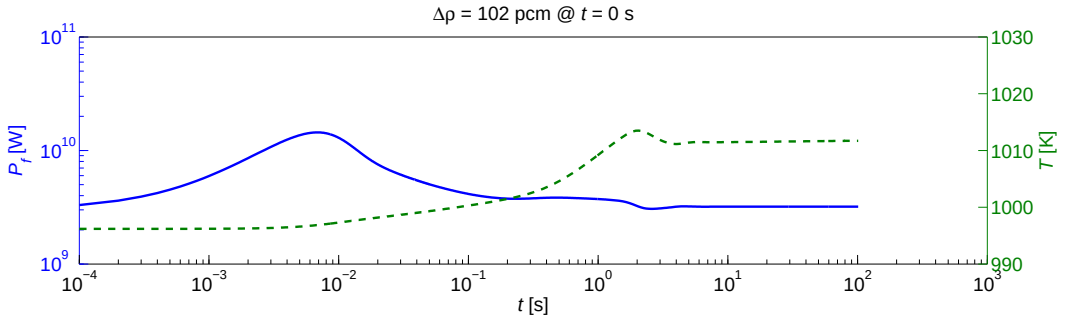

(b) For the new steady state $P_f = 3.2\,\text{GW}$ and $T = 1012\,\text{K}$.

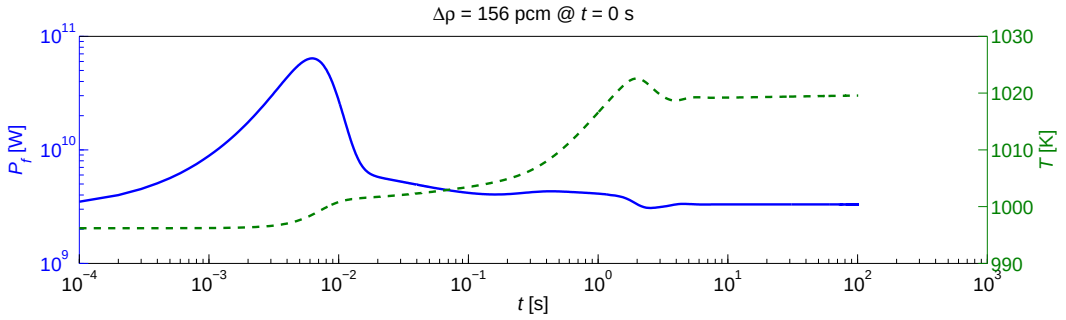

(c) For the new steady state $P_f = 3.3\,\text{GW}$ and $T = 1020\,\text{K}$.

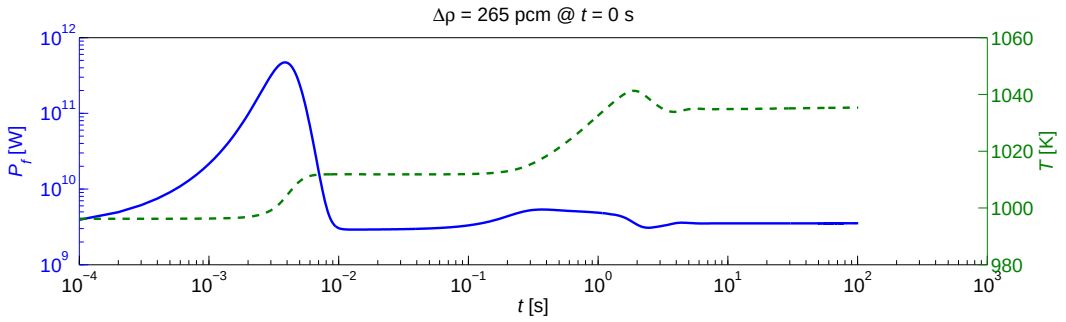

(d) For the new steady state $P_f = 3.5\,\text{GW}$ and $T = 1035\,\text{K}$.

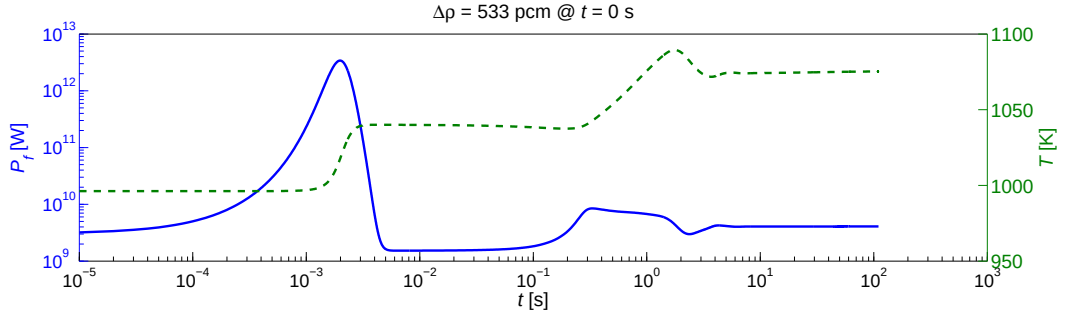

(e) For the new steady state $P_f = 4.1\,\text{GW}$ and $T = 1075\,\text{K}$.

Figure 4.18 – The total fission heat and average temperature as function of time for different introductions of reactivity.

5 Conclusion

Physical models which describe the turbulent flow and the neutronics were mutually linked, so that a physical model was formed for the molten salt fast reactor (MSFR), as defined by the EVOL project benchmark reference design of May 2011. The programs DALTON-MSR, HEAT and MIXER were upgraded and interdependently linked and the software package IMP was thus formed. This allowed the MSFR's neutron flux, precursor concentration, fission heat, temperature and fuel salt flow to be solved for as a function of space and time.

A model which describes the precursor transport in turbulent nuclear fuel flows was selected, and applied to the MSFR benchmark reference design. It was found that turbulent diffusion cannot be ignored, if an accurate solution for the precursor concentration has to be found, so that the time dependent behaviour of the MSFR can be accurately described.

Steady state solutions were found for the MSFR's neutron flux, precursor concentration, fission heat, temperature and fuel salt flow.

The fluoride and lithium in the fuel salt slightly moderate the neutrons. As a consequence the MSFR's neutron spectrum is epi-thermal, and the name "Molten Salt Fast Reactor" may confuse those who are new to the subject of molten salt reactor physics. The highest neutron flux is reached in the centre of the core where $\Phi = 9.66\,10^{15}\,\mathrm{s}^{-1}\,\mathrm{cm}^{-2}$. The highest flux in the structural material is reached at the boundaries where r = 0 m, here $\Phi = 2.4\,10^{15}\,\mathrm{s}^{-1}\,\mathrm{cm}^{-2}$. The energy groups with $E <$ 12.9 eV can all be combined into a single energy group. No up-scatter groups are needed to accurately describe the neutron flux of the MSFR.

For the MSFR the distribution of the precursor concentration is clearly shaped differently as compared to the shape of the neutron flux. The neutron flux is cosine shaped in the reactor core, whereas the slow decaying precursors are almost homogeneously distributed over the fuel salt. Almost all fast decaying precursors decay inside the reactor core.

A large zone is found within the reactor core, where the fuel salt recirculates. This has several effects on the reactors behaviour. The precursor concentration is higher in the core, compared to when the recirculation would not have occurred. The highest temperature of $T_{\mathrm{max}} = 1183\,\mathrm{K}$ is reached within the recirculation zone, and it is higher than $T_{\mathrm{max}} = 1048\,\mathrm{K}$ allowed by the benchmark design. The steady state average fuel salt temperature was found to be $T_{\mathrm{average}} = 995\mathrm{K}$.

The time dependent behaviour of the MSFR was investigated for a heat exchanger failure, a pump failure, and for instantaneous reactivity introductions.

An instantaneous reactivity introduction of $\Delta\rho = 533\,\mathrm{pcm}$ makes the MSFR prompt critical during a very short time interval. During the whole transient the average temperature increase by about 80 K. A new steady state is formed, where $P_f = 4.1\,\mathrm{GW}$ and the average fuel salt temperature is $T = 1075\,\mathrm{K}$.

After all the fuel salt pumps instantaneously fail, the average temperature rises 100 K in $t \approx 13.5\,\mathrm{s}$ to $T = 1094\,\mathrm{K}$. The negative reactivity coefficient of the fuel salt ensures that the fission power is reduced to $P_f(13.5) \approx 180\,\mathrm{MW}$, which is about equal to the delayed fission heat produced at that moment.

When all heat exchangers simultaneously fail the average temperature within the core quickly rises. Within seconds, this brings down the fission power to $P_f = 1.9\,\mathrm{GW}$. After the failure the fuel flow speed reduces, but natural convection keeps the fuel salt flowing, and allows a new steady state to be reached after a minute or two. As the fuel slows down the recirculation zone strongly reduces in size.

When systems such as the fuel pump or heat exchanger promptly fail to function, the MSFR remains to operate at temperatures well below the boiling point of the fuel salt, so that there is time for the fuel to be drained in to undercritical passively cooled storage tanks.

6 Recommendations and Future Research

During this project tests were performed only for the initial loading of the fuel which contained uranium-233 as a fissile isotope. With the current version of IMP, the MSFR's time dependent behaviour can also be investigated for the transuranic fuel composition as proposed by the benchmark. Note that when other fissile materials are used, the fission yields and decay constants of the precursor groups change. Different yields and decay constants can be readily adjusted for in DALTON-MSR's source code file "set_xs.f90".

When results of burn-up calculations become available and provide different fuel compositions, IMP can be used to investigate the MSFR's behaviour for those compositions as well.

During this project the mass flow was somewhat higher, and the inlet and outlet temperature were somewhat different, from what is proposed by the benchmark reference design of May 2011. Results obtained with IMP can be better compared to results obtained with other programs when exactly the same flow speed is used. To realise this, the body force of the fuel salt pump modelled should be reduced, and the inlet and outlet temperature should better represent the temperatures proposed. As this will effect the average temperature in the reactor core, the uranium concentration in the fuel salt will also have to be changed, if the same thermal power of 3 GW is still desired.

Currently, IMP does not model any change in the fuel salt concentration. It may be of value to implement a model for this. Especially for the xenon and protactinium concentration, as they effect the reactivity and neutron flux.

Delayed fission heat could be implemented in HEAT as being delayed - and not prompt, as is currently assumed. Delayed fission heat could be accounted for in a very similar way as for the precursors: the few group assumption for the precursors could also be used for the fission products that only produce decay heat. The transport equation 2.2 can be readily used for this purpose. The only difference is that delayed fission heat groups are a source for the fission heat and not a source of neutrons.

For creating more accurate (neutron spectrum dependent) group constant cross-sections SCALE's NEWT could be utilized and replace SCALE' XSDRN in MIXER. NEWT can immediately account for a two dimensional dependent geometry. Now only one dimensional changes in the geometry are accounted for during the cross-section generation process performed by SCALE's XSDRN - which is currently used by MIXER.

The heat extraction rate of the heat exchanger currently modelled in HEAT does not depend on the fuel salt velocity. This would however only be of interest when the fuel salt flow rate changes, which, during this project, is exclusively the case for the pump failure. In addition, the heat exchanger is not modelled to have any effects on the fuel flow. Normally many small pipes are used through which the secondary salt flows, thus cooling the fuel salt that passes on the outside of the small tubes. This strongly effects the fuel salt flow behaviour, not only within the heat exchanger, but also in its wake. Due to the many small tubes, the fuel salt would experience a resistance, which results in a pressure drop over the heat exchanger, and requires a stronger pump to be used. The model for the heat exchanger in IMP can generally be improved.

Instead of assuming axial symmetry, a fully 3-dimensional computational program for the MSFR could be realised, and instead of the $k-\epsilon$ model, large eddy simulation could be used for modelling the turbulence. This would lead to more detailed results, but it will also increase the required calculation time. The amount of work needed to realise these improvements should also not be underestimated. With some effort, the SIMPLE routine used in HEAT could be upgraded to the SIMPLER routine or better. This would save some calculation time.

After failure of the pumps, a new steady state exists during which the fuel is driven by natural convection, due to low temperatures in the down-comer and high temperatures in the reactor core. However, temperatures this high are unacceptable, as it would lead to corrosion of the structural material within a few days (maybe hours) of operation.

It may be desirable to circulate the fuel salt by natural convection only. If so, a MSFR reaches most of its potential when the reactor core's height is increased, the liquid fuel salt's resistance experienced is minimized, while the heat exchangers is located as high as possible, maybe in the horizontal part. Using a chimney

to further help natural convection should strongly be weighed against a decrease in the number of precursors that decay inside the core, as the chimney and extra piping consequently increase the volume of fuel salt that becomes located outside the reactor core, thus reducing the precursor concentration within the reactor core.

6.1 Recommendations for Programming Source Code

Extensive comments should be provided throughout the source code. This not only helps a potential next person that has to work with the code, it also helps the programmer when he revisits his own code after a month or so.

It would have helped this project a lot if previous programmers would have provided comments in the following cases.

- For *each* subroutine and function. A description of what the subroutine should do would help identifying what is programmed and - more importantly - what should have been programmed. When there are errors, it is of great value if there is no doubt about: which subroutine should do what.
- For each variable deceleration. For the same reasons as given above. It is of great value to know the purpose of a variable, especially when the variable is suspected to be misused.
- For each physical or mathematical model used, a reference should be given. This is holds for *all* scientific work.

A programmer can help himself, and potential users a lot by making coded checks. If an integer should always be greater then zero, a simple check can be programmed to test this, and when the test fails, i.e. the integer is ≤ 0, something should be written to the screen that informs the user what he did wrong, and the program should be brought to a stop. Many users will not read all the lines that are produced by a program. Stopping the program gives the immediate feedback that something is wrong.

It is also of great value to program and provide comments in English. Only few people understand Hungarian.

References

[1] M07miplib, part of the scale6 manual. Oak Ridge National Laboratory.

[2] Cross-section plotter, 2012. http://atom.kaeri.re.kr/cgi-bin/endfplot.pl.

[3] Standard k-epsilon model, 2012. http://www.cfd-online.com/Wiki/Standard_k-epsilon_model.

[4] Antonio Cammi, Valentino Di Marcello, Lelio Luzzi, Vito Memoli, and Marco Enrico Ricotti. A multi-physics modelling approach to the dynamics of molten salt reactors. *Annals of Nuclear Energy*, 38(6):1356 – 1372, 2011.

[5] A.N Chmelev, V.A Apse, and G.G Koulikov. Nuclear energy systems: Safety, transmutation of radiowastes and fuel self-sustaining. *Progress in Nuclear Energy*, 29, Supplement(0):439 – 443, 1995. Proceedings of the International Symposium on Global Environment and Nuclear Energy Systems.

[6] Sylvain David, Elisabeth Huffer, and Hervé Nifenecker. Revisiting the thorium-uranium nuclear fuel cycle. *Energy Panel of the French Physics Society*, 2007. Institut de Physique Nucléaire d'Orsay and Laboratoire de Physique Subatomique et de Cosmologie (IN2P3, Grenoble).

[7] James J. Duderstadt and Louis J. Hamilton. *Nuclear Reactor Analysis*. John Wiley and Sons, 1976.

[8] Beaudoin B.R. Frederickson R.A. Hartfield G.L. Hecker H.C. Milani S. Sarber W.K. Schick W.C. Freeman, L.B. Physics experiments and lifetime performance of the light water breeder reactor. *Nuclear Science and Engineering*, 102(4):341–364, 1989. cited By (since 1996) 17.

[9] Kazuo Furukawa, Kazuto Arakawa, L. Berrin Erbay, Yasuhiko Ito, Yoshio Kato, Hanna Kiyavitskaya, Alfred Lecocq, Koshi Mitachi, Ralph Moir, Hiroo Numata, J. Paul Pleasant, Yuzuru Sato, Yoichiro Shimazu, Vadim A. Simonenco, Din Dayal Sood, Carlos Urban, and Ritsuo Yoshioka. A road map for the realization of global-scale thorium breeding fuel cycle by single molten-fluoride flow. *Energy Conversion and Management*, 49(7):1832 – 1848, 2008. ICENES 2007, 13th International Conference on Emerging Nuclear Energy Systems, June, 2007, Istanbul, Turkiye.

[10] Tetsuo Hara and Shinsuke Kato. Numerical simulation of thermal plumes in free space using the standard k-epsilon model. *Fire Safety Journal*, 39(2):105 – 129, 2004.

[11] M. Hoogmoed. Coupled calculations for a thorium molten salt reactor. *M.Sc. Thesis*. September, 2009.

[12] Shin ichi Koyama, Tatsuya Suzuki, and Masaki Ozawa. From waste to resource, nuclear rare metals as a dream of modern alchemists. *Energy Conversion and Management*, 51(9):1799 – 1805, 2010. 14th International Conference on Emerging Nuclear Systems (ICENES 2009).

[13] Takashi Kamei and Saeed Hakami. Evaluation of implementation of thorium fuel cycle with LWR and MSR. *Progress in Nuclear Energy*, 53(7):820 – 824, 2011.

[14] Jan-Leen Kloosterman. Cross-section plotter, April 2012. http://www.janleenkloosterman.nl/ntvn_201201.php.

[15] D. Kotlyar, Y. Shaposhnik, E. Fridman, and E. Shwageraus. Coupled neutronic thermo-hydraulic analysis of full PWR core with Monte-Carlo based BGCore system. *Nuclear Engineering and Design*, 241(9):3777 – 3786, 2011. Seventh European Commission conference on Euratom research and training in reactor systems (Fission Safety 2009).

[16] Oak Ridge National Laboratory. MSRE overview, 2012. http://en.wikipedia.org/wiki/File:MSRE_Diagram.png.

[17] David LeBlanc. Molten salt reactors: A new beginning for an old idea. *Nuclear Engineering and Design*, 240(6):1644 – 1656, 2010.

[18] H.G. Macpherson. Molten-salt reactors. *Proceedings of the International Conference on the Constructive Uses of Atomic Energy, Washington, DC, November 1968, American Nuclear Society (March 1969)*.

[19] Karim Van Maele and Bart Merci. Application of two buoyancy-modified turbulence models to different types of buoyant plumes. *Fire Safety Journal*, 41(2):122 – 138, 2006.

[20] Elsa Merle-Lucotte, Daniel Heuer, Michel Allibert, Xavier Doligeza, Véronique Ghetta, and Christian Le Brun. Optimization and simplification of the concept of non-moderated Thorium Molten Salt Reactor. *International Conference on the Physics of Reactors 'Nuclear Power: A Sustainable Resource'*. Casino-Kursaal Conference Center, Interlaken, Switzerland, September 14-19, 2008.

[21] R.W. Moir. Recommendations for a restart of molten salt reactor development. *Energy Conversion and Management*, 49(7):1849 – 1858, 2008. ICENES 2007, 13th International Conference on Emerging Nuclear Energy Systems, June, 2007, Istanbul, Turkiye.

[22] K. Nagy, J.L. Kloosterman, D. Lathouwers, and T.H.J.J. van der Hagen. New breeding gain definitions and their application to the optimization of a molten salt reactor design. *Annals of Nuclear Energy*, 38(2 - 3):601 – 609, 2011.

[23] F.T.M. Nieuwstadt. *Turbulentie*. Epsilon Uitgaven, wetenschappelijke reeks nr. 24, 1998, 2008. Language: Dutch.

[24] Karl O. Ott and Robert J. Neuhold. *Introductory Nuclear Reactor Dynmics*. American Nuclear Society, 1985.

[25] Suhas V. Patankar. *Numerical Heat Transfer and Fluid Flow*. Hempshire Publishing Corporation, 1980.

[26] Andreas Pautz and Adolf Birkhofer. DORT-TD: A Transient Neutron Transport Code with Fully Implicit Time Integration. *Nuclear Science and Engineering*, 145(3):299 – 319. June 2, 2003.

[27] Martin Richard. China takes lead in race for clean nuclear power, 2011. `http://www.wired.com/wiredscience/2011/02/china-thorium-power/`.

[28] R. C. Robertson. *MSRE design and operations report part 1*. Oak Ridge National Laboratory (ORNL), 1965. Description of reactor design.

[29] M.W. Rosenthal, P.R. Kasten, and R.B. Briggs. Molten-salt reactors - history, status, and potential. *Oak Ridge National Laboratory, Oak Ridge, Tennessee 37830*, 1969.

[30] H K Versteeg and W Malalasekera. *An Introduction to Computational Fluid Dynamics the Finite Volume Method*. Pearson Prentice Hall, second edition, 2007.

[31] David C. Wilcox. *Turbulance modelling for CFD*. DCW Industries, 1993.

[32] C.R. Wilke and Pin Chang. Correlation of diffusion coefficients in dilute solutions. *AIChE Journal*, 1(2):264 – 270. June, 1955.

[33] Guan Heng Yeoh and Kwok Kit Yuen. *Computational Fluid Dynamics in Fire Engineering: Theory, Modelling and Practice*. Elsevier inc., 2009.

A Convection diffusion equation for turbulent flows

Here the Reynolds averaged convection diffusion equation for (turbulent) scalar transport will be taken as a starting point. It is given by equation 3.32 by Versteeg and Malalasekera [30] p65.

$$\frac{\partial \rho_{_F} \Theta}{\partial t} + \nabla \cdot (\rho_{_F} \Theta \, \mathbf{u}) = \nabla \cdot [\Gamma_{_\Theta} \nabla \Theta] + \left[-\frac{\partial \left(\rho_{_F} \overline{u_x' \Theta'} \right)}{\partial x} - \frac{\partial \left(\rho_{_F} \overline{u_y' \Theta'} \right)}{\partial y} - \frac{\partial \left(\rho_{_F} \overline{u_z' \Theta'} \right)}{\partial z} \right] + S_{_\Theta} \tag{A.1}$$

Where Θ is the transported scalar quantity and $\Gamma_{_\Theta}$ the thermal conductivity or molecular diffusion. Similar to Buossinesq's hypothesises it is assumed that turbulent transport of a scalar is proportional to the gradient of the mean value of the transported quantity [30] p68.

$$-\rho_{_F} \overline{u_i' \Theta'} = \Gamma_t \frac{\partial \Theta}{\partial x_i} \tag{A.2}$$

where $\Gamma_{_t} = \dfrac{\mu_{_t}}{\mathrm{Pr}_t}$ is the turbulent diffusivity, so that

$$-\rho_{_F} \overline{u_i' \Theta'} = \frac{\mu_{_t}}{\mathrm{Pr}_t} \frac{\partial \Theta}{\partial x_i} \tag{A.3}$$

Using this equation

$$\left[-\frac{\partial \left(\rho_{_F} \overline{u_x' \Theta'} \right)}{\partial x} - \frac{\partial \left(\rho_{_F} \overline{u_y' \Theta'} \right)}{\partial y} - \frac{\partial \left(\rho_{_F} \overline{u_z' \Theta'} \right)}{\partial z} \right] = \frac{\partial}{\partial x} \frac{\mu_{_t}}{\mathrm{Pr}_t} \frac{\partial \Theta}{\partial x} + \frac{\partial}{\partial y} \frac{\mu_{_t}}{\mathrm{Pr}_t} \frac{\partial \Theta}{\partial y} + \frac{\partial}{\partial z} \frac{\mu_{_t}}{\mathrm{Pr}_t} \frac{\partial \Theta}{\partial z} \tag{A.4}$$

$$= \begin{bmatrix} \frac{\partial}{\partial x} \\ \frac{\partial}{\partial y} \\ \frac{\partial}{\partial z} \end{bmatrix} \cdot \left(\frac{\mu_{_t}}{\mathrm{Pr}_t} \begin{bmatrix} \frac{\partial}{\partial x} \\ \frac{\partial}{\partial y} \\ \frac{\partial}{\partial z} \end{bmatrix} \Theta \right) \tag{A.5}$$

$$= \nabla \cdot \left[\frac{\mu_{_t}}{\mathrm{Pr}_t} \nabla \Theta \right] \tag{A.6}$$

Substituting the result in equation A.1 yields

$$\frac{\partial \rho_{_F} \Theta}{\partial t} + \nabla \cdot (\rho_{_F} \Theta \, \mathbf{u}) = \nabla \cdot \left[\left(\Gamma_{_\Theta} + \frac{\mu_{_t}}{\mathrm{Pr}_t} \right) \nabla \Theta \right] + S_{_\Theta} \tag{A.7}$$

which is the form of the scalar transport equation used in this thesis report.

B EVOL project benchmark reference design of May 2011

MOLTEN SALT FAST REACTOR

Reference configuration

The reference MSFR is a 3000 MWth reactor with a fast neutron spectrum and based on the Thorium fuel cycle. It may be started either with ^{233}U, enriched U or TRU elements as initial fissile load.

1 Reactor geometry

1.1 System description

The fuel salt flows upward in the active core until it reaches an extraction area which leads to salt-bubble separators through salt collectors. The salt then flows downward in the fuel salt heat exchangers and the pumps before finally re-entering the bottom of the core through injectors. The injection / extraction of the salt is performed through pipes of ~30 cm of diameter. This very simplified vision of the injection / extraction has to be improved during the EVOL project.

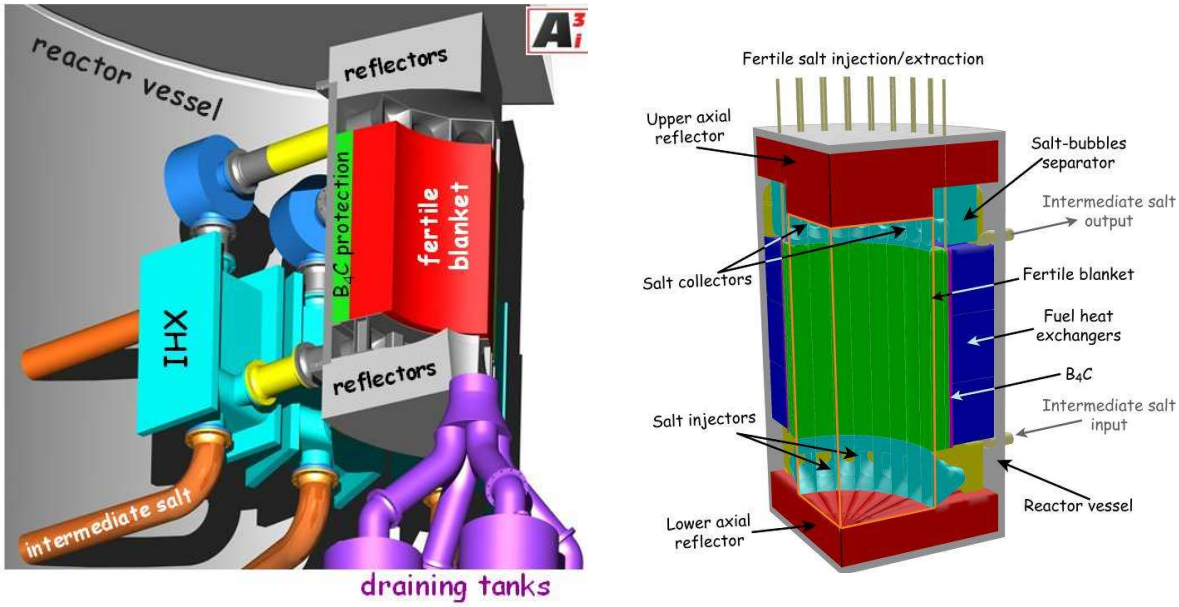

Fig. 1 (Left): *Global view of a quarter of the reactor vessel including the fertile blanket (red), the B_4C protection (green), the structure in Ni-based alloy (gray), the heat exchangers (pale blue) and the draining tanks (purple) -* ***(Right):*** *Schematic view of a quarter of the MSFR, the fuel salt (not represented here) being located within the orange lines*

The external circuit (salt collector, salt-bubble separator, heat exchanger, pump, salt injector and pipes) is broken up in 16 identical modules distributed around the core, outside the fertile blanket and within the reactor vessel. The external circuit is divided in two parts: the pipes (including the salt-bubble separator, the pump and the injector) and

the heat exchanger. The distribution of the salt between these two parts is chosen so as to minimize the pressure drops in the circuit. The fuel salt runs through the total cycle in 3,9 seconds. The salt circulation being considered uniform, the residence time of the salt in each zone of the circuit and the core is proportional to the volume of this zone.

The total fuel salt volume is distributed half ($9m^3$) in the core and half ($9m^3$) in the external circuit.

The external core structures and the heat exchangers are protected by thick reflectors (1m height for the axial reflectors) made of nickel-based alloys which have been designed to absorb more than 99% of the escaping neutron flux.

1.2 Core geometry

As shown in Fig. 2, the core is a single cylinder (the diameter being equal to the height) where the nuclear reactions occur within the flowing fuel salt. The core is composed of three volumes: the active core the upper plenum and the lower plenum. The fuel salt considered in the simulations is a binary salt, LiF - (Heavy Nuclei)F_4, whose (HN)F_4 proportion is set at 22.5 mole % (eutectic point), corresponding to a melting temperature of 565°C. The choice of this fuel salt composition relies on many systematic studies (influence of the chemical reprocessing on the neutronic behaviour, burning capabilities, deterministic safety evaluation and deployment capabilities). This salt composition leads to a fast neutron spectrum in the core.

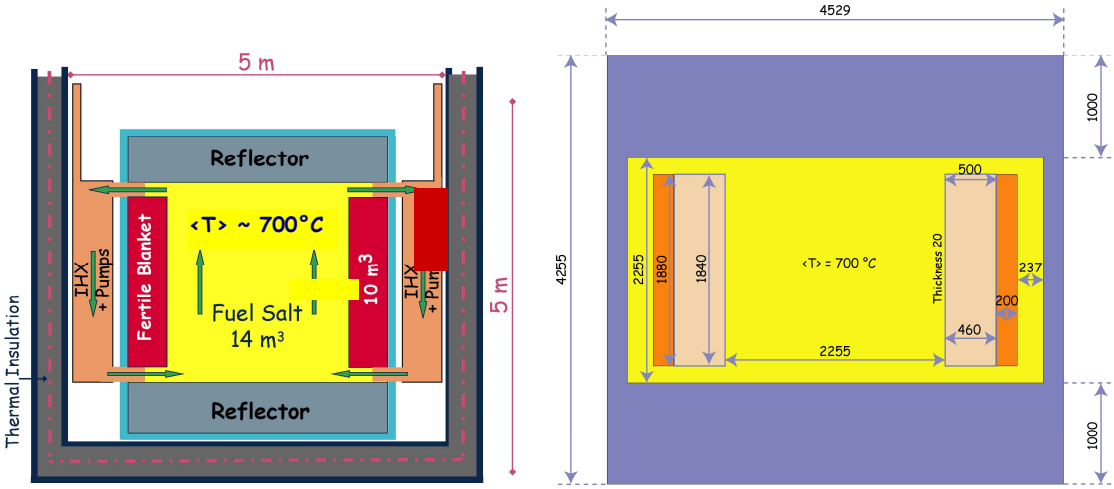

Fig. 2 (Left): *Simplified to scale vertical scheme of the MSFR system including the core, blanket and fuel heat exchangers (IHX) –* ***(Right):*** *Model of the core as used for the neutronic simulations (dimensions given in mm) with the fuel salt (yellow), the fertile salt (pink), the B_4C protection (orange) and the reflectors and 20mm thick walls in Ni-based allow (blue).*

The operating temperatures chosen for our neutronic simulations range between 625°C (input) and 775°C (output), the lower limit due to the salt's melting point, the

upper limit estimated from the structural materials chosen for our simulations and detailed in section 5.

1.3 Blanket geometry

As shown in Fig.1 and 2, the radial reflector is a fertile blanket (~50 cm thick) filled with 7.7m^3 of a fertile salt LiF-ThF_4 with molar 22.5% of ^{232}Th. This fertile blanket improves the global breeding ratio of the reactor thanks to a ^{233}U extraction in an around six months period, i.e. 100% of the ^{233}U produced in the blanket is extracted in 192 days (40 liters per day as shown in the lower part of Fig 3). This fertile blanket is surrounded by a 20cm thick neutronic protection of B_4C which absorbs the remaining neutrons and protects the heat exchangers. The thickness of this B_4C protection has been determined so that the neutron flux arriving from the core through it is negligible compared to the flux of delayed neutrons emitted in the heat exchangers.

The radial blanket geometry is an angular section toron of 1.88 m high and 50 cm thick. The 2 cm thick walls are made of Ni-based alloy (see composition in Table 4). A single volume of fertile salt is considered, homogenous and cooled to a mean temperature of 650°C. A temperature variation of the fertile salt of around 30 °C between the bottom and the top of the fertile blanket may be introduced to check its low impact on the reactor evolution.

2 Fuel salt initial composition

The core contains a fluoride fuel salt, composed of 77.5 molar % of LiF enriched in ^{7}Li (99.999 at%) and 22.5 molar % of heavy nuclei (HN) amongst which the fissile element, ^{233}U or Pu. This HN fraction is kept constant during reactor evolution, the produced FPs replacing an equivalent proportion of the lithium.

2.1 ^{233}U-started MSFR

As detailed in table 2, the initial fuel salt is composed in this case of LiF-ThF_4-$^{233}UF_3$, the initial fraction of ^{233}U being adjusted to have an exactly critical reactor.

2.2 TRU-started MSFR

Table 1: *Proportions of transuranic nuclei in UOX fuel after one use in PWR without multi-recycling (burnup of 60 GWd/ton) and after five years of storage*

Isotope	Proportion in the mix
Np 237	6.3 mole%
Pu 238	2.7 mole%
Pu 239	45.9 mole%
Pu 240	21.5 mole%
Pu 241	10.7 mole%
Pu 242	6.7 mole%
Am 241	3.4 mole%
Am 243	1.9 mole%
Cm 244	0.8 mole%

Cm 245	0.1 mole%

The initial fuel salt is composed of LiF-ThF_4-$(TRU)F_3$. More precisely, the reference MSFR is started with a TRU mix of 87.5% of Pu (^{238}Pu 2.7%, ^{239}Pu 45.9% , ^{240}Pu 21.5%, ^{241}Pu 10.7%, and ^{242}Pu 6.7%), 6.3% of Np, 5.3% of Am and 0.9% of Cm, as listed in table 1 and corresponding to the transuranic elements contained in an UOX (60 GWd/ton) fuel after one use in a standard LWR and five years of storage. The amounts of TRU elements initially loaded in the TRU-started MSFR are given in table 2.

Table 2: *Summary of the characteristics of the MSFR*

<table>
<tr><td>Thermal power (MWth)</td><td colspan="5">3000</td></tr>
<tr><td>Electric power (MWe)</td><td colspan="5">1500</td></tr>
<tr><td>Fuel Molten salt initial composition (mol%)</td><td colspan="5">LiF-ThF_4-$^{233}UF_4$ or LiF-ThF_4-$(Pu\text{-}MA)F_3$ with 77.5 % LiF</td></tr>
<tr><td>Fertile Blanket Molten salt initial composition (mol%)</td><td colspan="5">LiF-ThF_4 (77.5%-22.5%)</td></tr>
<tr><td>Melting point (°C)</td><td colspan="5">565</td></tr>
<tr><td>Input/output operating temperature (°C)</td><td colspan="5">625-775</td></tr>
<tr><td rowspan="6">Initial inventory (kg)</td><td colspan="2">^{233}U-started MSFR</td><td colspan="3">TRU-started MSFR</td></tr>
<tr><td>Th</td><td>^{233}U</td><td>Th</td><td colspan="2">Actinide</td></tr>
<tr><td rowspan="4">38 300</td><td rowspan="4">5 060</td><td rowspan="4">30 600</td><td>Pu</td><td>11 200</td></tr>
<tr><td>Np</td><td>800</td></tr>
<tr><td>Am</td><td>680</td></tr>
<tr><td>Cm</td><td>115</td></tr>
<tr><td>Density (g/cm^3)</td><td colspan="5">4.1052</td></tr>
<tr><td>Dilatation coefficient (/°C)</td><td colspan="5">$7.526\ 10^{-4}$</td></tr>
<tr><td>Core dimensions (m)</td><td colspan="5">Radius: 1.1275
Height: 2.255</td></tr>
<tr><td>Fuel Salt Volume (m^3)</td><td colspan="5">18
9 out of the core
9 in the core</td></tr>
<tr><td>Blanket Salt Volume (m^3)</td><td colspan="5">7.7</td></tr>
<tr><td>Total fuel salt cycle in the system</td><td colspan="5">3.9 s</td></tr>
</table>

Commentaire [d1] : More precise values

Table 3: *Initial critical fissile inventory for the calculation without evolution*

^{233}U-started MSFR		TRU-started MSFR		
Th	^{233}U	Th	Actinide	
38 281 kg 19.985 %mol	4 838 kg 2.515 %mol	30 619 kg 16.068 %mol	Pu	11 079 kg 5.628 %mol
			Np	789 kg 0.405 %mol
			Am	677 kg 0.341 %mol
			Cm	116 kg 0.058 %mol

Commentaire [d2] : New table with fissile quantity values for the starting up

In fact, the evolution calculation shows that more fissile material is needed to stay critical short time after the starting up.

3 Fuel salt reprocessing

As displayed in Fig. 3, the salt management combines a salt control unit, an online gaseous extraction system and an offline lanthanide extraction component by pyrochemistry.

The gaseous extraction system, where helium bubbles are injected in the core, removes all non-soluble fission products (noble metals and gaseous fission products). This on-line bubbling extraction has a removal period $T_{1/2}$=30 seconds in the simulations. The elements extracted by this system are the following: Z = 1, 2, 7, 8, 10, 18, 36, 41, 42, 43, 44, 45, 46, 47, 51, 52, 54 and 86.

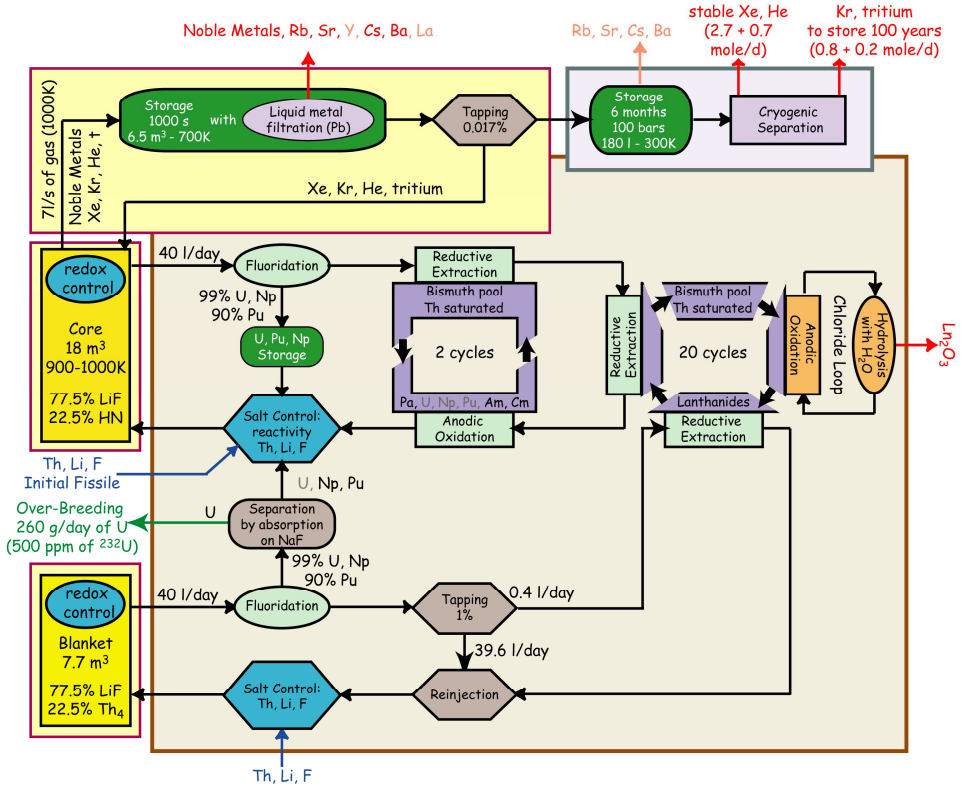

Fig. 3: *Overall scheme of the fuel salt management including the online gaseous extraction (top) and the offline reprocessing unit (bottom) – The yellow boxes surrounded by a red line represent the parts enclosed within the reactor vessel*

A fraction of salt is periodically withdrawn and reprocessed offline in order to extract the lanthanides before it is sent back into the core. The actinides are sent back into the core as soon as possible in order to be burnt. With the online control and adjustment part, the salt composition and properties are checked.

The rate at which this offline salt reprocessing is done depends on the desired breeding performance. In the reference simulations, we have fixed the reprocessing rate at 40 litres per day whatever the fuel salt volume, i.e. the whole core is reprocessed in 450 days. In the simulation of the reactor evolution, this is taken into account through a 100% offline extraction of the following fission products in 450 days: Z = 30, 31, 32, 33, 34, 35, 37, 38, 39, 40, 48, 49, 50, 53, 55, 56, 57, 58, 59, 60, 61, 62, 63, 64, 65, 66, 67, 68, 69, 70

Thanks to this simplified view of the reprocessing, even if not totally realistic, a stationary state may be reached during the reactor evolution. In the following, the extraction efficiencies may be refined in cooperation with WP3.

As displayed in fig 3, the fission products of the fertile blanket are slowly removed, with a rate of 0,4 liter of salt cleaned per day i.e. the whole fertile salt volume ($7.7m^3$) cleaned in 19250 days (52.7 years).

4 Physicochemical properties of the molten salts used in the MSFR

During reactor operation, fission products and new heavy nuclei are produced in the salt up to some mole % only, they do not impact the salt physicochemical properties needed for our studies. In the absence of precise data for the salt chosen in our simulations, we have used the well known characteristics of the LiF (77.5 mole%)-ThF_4 salt, presented in table 3. The last column of Table 1 summarizes the values used in these studies, at a mean temperature of 700°C (halfway between the low and the high operating temperatures).

Commentaire [d3] : instead of 695 °C

Table 4: *Physicochemical properties used for the fuel salt*

	Formula	Value at 700°C
Density ρ (g/cm^3)	$4.632 - 7.526 \cdot 10^{-4}\ T_{(°C)}$	4.1052
Dynamic viscosity μ (Pa.s)	$0.39943 \cdot 10^{-3} \exp(2812.9/T_{(K)})$	$7.191\ 10^{-3}$
Thermal Conductivity λ (W/m/K)	$0.16016 + 5 \cdot 10^{-4}\ T_{(°C)}$	0.510
Calorific capacity c_p (J/kg/K)	-	1045

Commentaire [d4] : instead of 695 °C

Commentaire [d5] : instead of 4.124

Commentaire [d6] : instead of 7.76 10^{-3}

Commentaire [d7] : instead of 0.498

The fertile salt, located in the radial blanket surrounding the core and serving as radial reflector, is composed of 77.5 LiF-22.5 ThF_4 and has similar properties.

The secondary salt is not determined but we have assumed its characteristics to be identical to those of the fuel salt (see table 3). In fact, the constraints on this secondary salt being less stringent than for the primary salt, its capacities in terms of heat transfers will probably be better. Our simulations thus correspond to the worst case.

5 Structural materials

The structural materials of the reactor, even if they are located around the core and not directly in it, have to bear the neutron flux together with high temperatures. We have considered for our simulations a Ni-based alloy containing W and Cr as detailed in tab 4.

Table 5: *Composition (at%) of the Ni-based alloy considered for the simulation of the structural materials of the core*

Ni	W	Cr	Mo	Fe	Ti	C	Mn	Si	Al	B	P	S
79.432	9.976	8.014	0.736	0.632	0.295	0.294	0.257	0.252	0.052	0.033	0.023	0.004

The composition of the material used for the heat exchangers being not yet fixed, we have assumed its thermal conduction to be equal to 24 W/m/K, and typical value for a Ni-based alloy. The density of the Ni-based alloy is equal to 10 (data given by Thierry Auger – WP4). This material will not be submitted to a high neutron flux; hence the choice of its composition is not too constrained.

Commentaire [d8] : The density of the alloy added here

We have considered the composition of natural boron : 19.8% of ^{10}B and 80.2% of ^{11}B. The B_4C density is equal to 2.52016 (data used in SIMMER, given by KIT).

Commentaire [d9] : The density and the abundance of natural boron added here

6 Other data

Table 6: *Abundances of seven delayed neutron precursors for two uranium isotopes*

Group	1	2	3	4	5	6	7
Precursor	^{87}Br	^{137}I	^{88}Br	^{93}Rb	^{139}I	^{91}Br	^{96}Rb
Half-Life	55.9 s	24.5 s	16.4 s	5.85 s	2.3 s	0.54 s	0.199 s
Abundances							
^{233}U (fast)	0.0788	0.1666	0.1153	0.1985	0.3522	0.0633	0.0253
^{233}U (thermal)	0.0787	0.1723	0.1355	0.1884	0.3435	0.0605	0.0211
^{235}U (fast)	0.0339	0.1458	0.0847	0.1665	0.4069	0.1278	0.0344
^{235}U (thermal)	0.0321	0.1616	0.0752	0.1815	0.3969	0.1257	0.0270
Mean Value	0.0742	0.1679	0.1209	0.1915	0.3533	0.0684	0.0240

Mean values of abundances for the neutron precursors are considered here for fissions that are due to ^{233}U (90%) and ^{235}U (10%) with a spectrum located between a thermal and a fast one (50% of thermal spectrum and 50% of fast spectrum).

Commentaire [d10] : The explanation on the calculation of the mean values was added

7 Calculations to perform for both the 233U-started and the TRU-started MSFR

- Either the amounts (in kg) of Th and ^{233}U / TRU needed initially to have k_{eff}=1 with the incertitudes or the k_{eff} value while using our data for the initial amounts of Th and fissile matters (table 3)
- Evolution of the materials composition (fuel salt, fertile salt, structural materials in contact with the fuel salt) from beginning of life (BOL) to equilibrium
- The effective proportion of delayed neutrons in the salt (BOL and equilibrium)
- Generation time
- Neutron spectrum (neutron flux as a function of the neutron energy) in the core
- The breeding ratio and/or the breeding gain at equilibrium, proposed definition[1]:

  Breeding ratio: BR = decay rate of ^{233}Pa / (capture + fission of ^{233}U)
  Breeding gain: BG = total production of ^{233}U - initial inventory of ^{233}U

Commentaire [d11] : Definition of breeding gain and breeding ratio added

- The fuel burn-up at equilibrium
- The feedback coefficients: total / Doppler / density (BOL and equilibrium)

[1] These definitions have to be improved by other partners and we will have to choose one optimized definition in WP2 before performing the same calculation on this parameter with our different numerical tools.

- Power / heat sources distribution, both in the fuel salt and in the fertile salt - function and/or discretization
- Irradiation damages to the structural materials (walls of the fertile blanket / axial reflectors) as a function of the depth: dpa + Helium production + W transmutation
- Temperature distribution in the core
- Salt velocity distribution in the core

NB: The compositions (salt, structural materials) at steady state are not mentioned in this paper since all the partners have numerical tools for the simulation of reactor evolution. Do not hesitate to ask for if necessary.